Resist and Residue Removal Using Gas-Expanded Liquids

A Dissertation

Presented to

The Academic Faculty

By

Matthew Thomas Spuller

In Partial Fulfillment

Of the Requirements for the Degree

Doctor of Philosophy in Chemical Engineering

Georgia Institute of Technology

October 30, 2003

Resist and Residue Removal Using Gas-Expanded Liquids

Approved by:

Dr. Charles A. Eckert

Dr. Clifford L. Henderson

Dr. Charles L. Liotta

Dr. J. Carson Meredith

Dr. Dennis W. Hess, Advisor

Date Approved: 10/30/2003

ACKNOWLEDGEMENTS

Financial and technical support of this project was provided by DuPont-EKC Technology (Hayward, CA). The author is grateful for their long term commitment and significant contributions. Dr. Mel Carter, Dr. Michael Fury, Dr. David Maloney and Robert Sherrill of DuPont-EKC were particularly influential in the collaboration and the success of the project. Additional financial support was provided through the Applied Materials Graduate Student Fellowship awarded by Applied Materials, Inc. (Santa Clara, CA).

This thesis research was completed under the advisement of Professor Dennis Hess. Professor Hess's standards for creativity and excellence in research are reflected in this work. In addition to direct scientific contributions to this thesis, Professor Hess's approachability, support of professional development, and good-natured persona made for an excellent graduate research experience, and one gratefully appreciated by the author.

The author is tremendously thankful for many other contributions. Dr. Tazrien Kamal offered training and support to begin this research. The expertise of Dr. Ankur Agrawal and Professor Cliff Henderson regarding interferometry, of Dr. Jeff Morris regarding wetting and transport modeling, and of Professor Charles Eckert and Professor Charles Liotta regarding the theory and application of gas-expanded liquids was especially helpful. Group members Dr. Galit Levitin, Chris Timmons, and Satya Myneni were particularly helpful in this research, as were fellow graduate students David

Desrocher and Roy Furbank. Undergraduate students Beth Floyd and Ross Perchuk were also of assistance in the laboratory.

The thesis advisory committee was critical to the success of this project through annual committee meetings and periodic individual meetings. These committee members include Professor Eckert, Professor Henderson, Professor Liotta, and Professor Carson Meredith.

Finally, the author thanks his family. His parents have given him the greatest gift, defined his character, and instilled an inquisitive nature well-fitted for research. Particular thanks go to his uncle, John Spears, for providing key encouragement and advice regarding the pursuit of an advanced degree. The author also thanks his wife, Laura, for being the omnipresent positive influence and for making life as a graduate student incredibly tolerable.

TABLE OF CONTENTS

Acknowledgements	iii
List of Tables	vii
List of Figures	ix
List of Symbols	xiv
Summary	xvi
Chapter 1. Introduction	1
Chapter 2. Background	4
2.1 Semiconductor Processing	4
2.2 Problem Significance	5
2.3 Future Process Requirements	8
Chapter 3. Gas-Expanded Liquids	10
3.1 Introduction	10
3.2 Physical Property Modification	12
3.3 CO_2 Expansion of Organic Solvents	14
3.4 CO_2 Expansion of Organic Bases	18
3.5 High Pressure ATR-FTIR	20
3.6 Environmental, Safety, and Health Issues	23
3.7 Conclusion	24
Chapter 4. Wetting	26
4.1 Introduction	26
4.2 Wetting Impedance: Gas Cavity Formation	27

4.3 Complete Wetting through Gas Transport 33

4.4 Diffusion-Dominated Transport 37

4.5 Discussion 38

4.6 Feature Collapse 41

4.7 Dielectric Compatibility 43

4.8 Conclusion 44

Chapter 5. Transport Properties 47

5.1 Introduction 47

5.2 Transport within Nanoscale Features 48

5.3 Dissolution Rate Enhancement 49

5.4 Optimizing Properties with Gas-Expanded Liquids 51

5.5 Discussion 55

5.6 Conclusion 56

Chapter 6. *In Situ* Monitoring of Film Refractive Index and Thickness 58

6.1 Introduction 58

6.2 Experimental Setup 59

6.3 Reflectance Theory 62

6.4 Refractive Indices of Gases and Liquids 64

6.5 Refractive Index and Thickness of Thin Films 66

6.6 Discussion 71

6.7 Conclusion 72

Chapter 7. Photoresist Removal with CO_2-Expanded Liquids 73

7.1 Introduction 73

7.2 Experimental Equipment Setup 74

7.3 Experimental Procedure 77

7.4 Organic Residue Removal from Silicon 78

7.5 Results and Discussion 79

7.6 Scale-Up of GXL Processes 86

7.7 Conclusion 87

Chapter 8. Conclusions 89

Chapter 9. Future Work 93

9.1 Mechanistic Studies of Polymer Removal in CO_2 93

9.2 Investigation of Wetting and Feature Collapse 96

Appendices. 99

A. MATLAB Program for Estimating Wettability 99

B. Removal of Native Copper Oxides with Acetic Acid 103

C. Spatial Resolution on Patterned Surfaces (SR-XPS) 108

References 115

Vita 120

LIST OF TABLES

Table 2.1.	Wiring pitch and aspect ratio are the geometries of interest for cleaning (SIA, 2001).	6
Table 3.1.	The viscosity (μ), surface tension (γ), and density (ρ) of ethanol and liquid carbon dioxide (DIPPR, 2002).	12
Table 3.2.	Economic factors for estimating the ratio of the cost of consumables to the cost of equipment.	24
Table 4.1.	Variables to be considered in the design of a liquid process.	26
Table 4.2.	Feature geometries of DRAM trench capacitors (DTC) and global interconnects (GI) at particular years of production.	40
Table 6.1.	Measured and reported (DIPPR, 2002) refractive indices (at 589 nm).	65
Table 6.2.	Refractive index of CO_2-expanded ethanol, experimental and predicted results.	66
Table 6.3.	Comparison of PHOST film thickness and RI determined by ellipsometry and by the current approach.	67
Table 6.4.	Comparison of JSR resist thickness and RI determined by ellipsometry and by the current approach.	67
Table 6.5.	Comparison of PHOST film thickness and RI determined by ellipsometry, by interferometry, and following exposure to dilute ethanol vapor.	69
Table 7.1	XPS results of treating patterned samples with CO_2-expanded NMP.	85
Table 7.2	XPS results of treating JSR resist with CO_2-expanded NMP.	86

Table 9.1. Comparisons of select properties of ethane and carbon dioxide. 94

Table B.1. The atomic composition of copper films treated with acetic acid and exposed to air. The fraction copper decreases with time as the amount of native oxide and adventitious carbon on the surface increases. 106

LIST OF FIGURES

Figure 3.1.	Comparison of various classes of fluids.	11
Figure 3.2.	Pressure-composition data for GXLs of CO_2 and ethanol at 18°C, 25°C, and 30°C (Chang et al., 1998).	15
Figure 3.3.	Pressure-composition data for GXLs of CO_2 and NMP at 15°C and 25°C (Zubchenko, 1985).	15
Figure 3.4.	Two high pressure syringe pumps are used to formulate and deliver GXLs. A schematic diagram of the pumps and mixing chamber is shown on the right.	16
Figure 3.6.	Molecular structures of, from left to right, NMP, butyrolactone, 2-(2-aminoethoxy)ethanol, and morpholine.	19
Figure 3.7.	Diagrams of the modified high pressure FTIR reactor.	22
Figure 4.1.	A nonplanar solid surface (S) with trapped gas cavities (G) formed with a liquid (L) at contact angle, θ.	28
Figure 4.2.	For a feature with height h_1, liquid will fully wet the feature while that with height h_3 will form a gas cavity. Height h_2 defines the critical aspect ratio, $\cot\theta$.	29
Figure 4.3.	An illustration of the geometry defined to describe feature wetting.	30
Figure 4.4.	The feature pressure increases exponentially as the feature size is reduced. The plot illustrates this trend for surface tensions of (a) 72, (b) 24, and (c) 1 mN/m.	32
Figure 4.5.	The momentum and concentration boundary layer for flow past a flat substrate.	34
Figure 4.6.	The wetting time is independent of the liquid velocity up to 20 m/s for a feature with 150-nm diameter and 1.2 μm depth.	36

Figure 4.7. Wetting times of IC features specified in the ITRS, where (a)-(c) are DRAM trench capacitors and (d)-(f) are global interconnects to be produced in 2002, 2005, and 2008, respectively. 39

Figure 4.8. Feature collapse of PHOST as a function of aspect ratio with aqueous processing. 42

Figure 4.9. Plot of feature collapse as a function of feature geometry and process fluids. The height on the ordinate is the maximum height of PHOST-based photoresist lines that can be processed without collapse. This comparison is based on a contact angle of 50° and a PHOST critical stress of 5.5 MPa. 43

Figure 5.1. Ratio of the time to transport species within a nanoscale feature using a GXL to that using a traditional liquid. A GXL with as much as 46% CO_2 will not increase the time necessary for removal compared to a liquid. 52

Figure 5.2. Ratio of the dissolution rate in a GXL to the dissolution rate in a traditional liquid at a particular rotation rate. Dissolution rate enhancement occurs for all GXLs with a solvent fraction greater than ~15%. 53

Figure 5.3. Ratio of the dissolution rate in a GXL to the dissolution rate in a traditional liquid when dispensing an equivalent amount of solvent. Significant dissolution rate enhancement occurs. 54

Figure 5.4. Ratio of moles of solvent consumed, *n*, in a GXL to that in a traditional liquid for equivalent dissolution rates. The amount of solvent that must be consumed is significantly less in a GXL than in a traditional liquid. 55

Figure 6.1. Schematic diagram of the dissolution rate monitor. 59

Figure 6.2. A gas-liquid contactor is used to modify the composition of ethanol vapor exposed to a thin film sample for film thickness measurements with MWI. 61

Figure 6.3. A schematic diagram of the path of normally incident transmitted and reflected light. 61

Figure 6.4. Refractive index of CO_2 vs pressure. 66

Figure 6.5. The reflectance model fit to reflectance data of a PHOST film. 67

Figure 6.6. Refractive index and thickness change of PHOST films exposed to ethanol vapor. 68

Figure 6.7. Relative reflectance from a PHOST film before and after exposure to dilute ethanol vapor. 69

Figure 6.7. Refractive index and thickness change of a commercial JSR resist in a 0.13N TMAH aqueous solution. 70

Figure 6.8. Compression of a commercial JSR photoresist in high pressure CO_2. 70

Figure 7.1. The high-pressure 8-inch wafer treatment system schematic. 74

Figure 7.2. A schematic diagram of the center-fed flow reactor in which samples are rotated on an 8-inch platen. 74

Figure 7.3. Picture of the complete high pressure system used to investigate GXL treatment of films. 76

Figure 7.4. A schematic diagram of the dissolution rate monitor for dissolution under elevated pressures. 77

Figure 7.5. Single wavelength interference spectrum for PHOST exposed to CO_2-expanded ethanol at 5 MPa. The liquid contacts the sample at t = 22 sec, at which time the intensity drops significantly due to interference with the meniscus. Swelling occurs prior to liquid exposure, characterized by the oscillation of the intensity. No film is detectable after liquid submersion, likely due to rapid dissolution. 80

Figure 7.6. Swelling of PHOST upon exposure to ethanol vapor. 81

Figure 7.7. Surface concentration following treatment of PHOST films with GXLs of different composition. Ethanol yields a surface with 20% silicon. The same results are obtained with GXLs containing as little as 25% ethanol. GXLs with less ethanol do not remove the PHOST, and no silicon is detected. 81

Figure 7.8. C1s binding energy following treatment with GXLs of PHOST films. Ethanol yields a surface with C1s of 284 eV. The same results are obtained with GXLs containing as little as 25% ethanol. GXLs with less ethanol do not completely remove organic material, resulting in a binding energy shift. 82

Figure 7.9. The SEM image of PHOST following treatment with CO_2-expanded ethanol at 5.5 MPa and 21ºC indicates large amounts of residual polymer on the silicon substrate. 83

Figure 7.10. Surface concentration following treatment of PHOST films with CO_2-expanded NMP of different composition. 84

Figure 7.11. Visual inspection following treatment of PHOST films with CO_2-expanded NMP of different composition. From left to right, these samples were treated with GXLs of 15mol%, 20mol%, and 25mol% NMP. 84

Figure 9.1. Schematic of the FTIR high pressure cell in which a film of interest is deposited on a silicon waveguide. The IR spectrum of the film can be obtained *in situ* as the film is exposed to a GXL. 95

Figure 9.2. The feature geometrical parameters are defined by the height (*h*), wall thickness (*t*), line length (*l*), gap width (*g*), and line spacing (*w*). 98

Figure B.1. Absolute (left) and normalized (right) C1s spectra of copper films treated with acetic acid and subsequently exposed to air. 104

Figure B.2. Absolute (left) and normalized (right) O1s spectra of copper films treated with acetic acid and subsequently exposed to air. 104

Figure B.3. Absolute (left) and normalized (right) Cu-Auger spectra of copper films treated with acetic acid and subsequently exposed to air. 105

Figure B.4. Absolute (left) and normalized (right) Cu2p spectra of copper films treated with acetic acid and subsequently exposed to air. 105

Figure C.1. Basic geometry of line/trench sample. 108

Figure C.2. Illustration of a.) x-ray shading, and b.) electron shading. Gray lines indicate shadowed regions. 109

Figure C.3. Nonideal pattern with sloped sidewalls. 110

Figure C.4. Plasma etched aluminum lines, (nominally 3 micron lines, 10 micron spaces). 111

Figure C.5. Plot showing the effects of take off angle on trench area exposed. Aluminum lines are oriented perpendicular to analyzer. 112

Figure C.6. Blue spectrum: aluminum lines are oriented perpendicular to analyzer. Red spectrum: aluminum lines are oriented parallel to analyzer. With trenches exposed (Red), the atomic concentration of Si is 3.6% while when unexposed it is 0.5%. 113

LIST OF SYMBOLS

C	concentration, C_B in the bulk liquid, C_O in the liquid at the interface
D	diffusivity
DR	dissolution rate
h	height of liquid dispensed on a rotating substrate, or feature height, or imaginary Fresnel reflection coefficient
h_P	height of boundary layer
k_H	Henry's constant
k	extinction coefficient
L	substrate diameter, or length
l	distance from top of feature, l_e at physical equilibrium
M	total amount of gas dissolved in the liquid
M_i	molecular weight of i
n	moles of solvent consumed
n_i	refractive index of i
P	pressure
ΔP_{int}	interfacial pressure drop
P_f	pressure of gas trapped in feature
P_O	initial pressure of gas in feature
Q	volumetric flow rate
R	ideal gas constant
R_i	molar reflectance of i
r	radius, or radius of curvature, or real Fresnel reflection coefficient
S	total dissolved

T temperature

t time, t_p for Poiseuille flow wetting o, t_d for diffusional transport wetting

u velocity

V molal volume of solute

w feature width

x mole fraction solvent in a GXL

Greek

γ gas-liquid surface tension

δ laminar boundary layer thickness, or optical path length

Δl coherence length

$\Delta\lambda$ spectrometer resolution

ζ combination variable

θ contact angle

λ wavelength

μ dynamic viscosity

ν kinematic viscosity

ρ density, or reflectance amplitude

ϕ solvent interaction parameter

ω rotation rate

SUMMARY

Each new generation of integrated circuits and other nano-structured devices is produced at ever decreasing length scales. The extension of conventional liquid-phase processes for the manufacturing of these devices is uncertain.

This work investigates the ability of liquids to wet nanoscale features. A model for wetting time is derived that may be used to identify those geometries for which wetting is critical. Conditions under which wetting time is significant may result in low yield and poor uniformity, and may require alternate-phase processing. Furthermore, the dependence of wetting time on the properties of the fluid are quantified so that fluids may be designed to have optimal properties and thus optimal performance for wetting in liquid-phase processes. The resulting model can be used as a tool to predict future processing requirements, and when necessary, to design novel processes implementing alternative phase fluids (e.g. vapor, gas-expanded liquids (GXLs), and supercritical fluids).

This study also quantitatively predicts specific effects associated with modified transport properties for dissolution and transport in nanoscale features. The use of GXLs is a particularly promising alternative to conventional liquid-phase processes. GXLs have superior mass transport properties relative to liquids, but can maintain the solvent strength necessary for IC process steps such as post-etch residue removal and photoresist stripping. In addition, the environmental benefits associated with carbon dioxide (CO_2)-based processes can be substantial.

Conceptual demonstration of the use of CO_2-expanded liquids for photoresist and residue removal has been performed. GXLs containing up to 75% CO_2 are equally as effective as the pure solvents for removal of PHOST-based films. These experiments indicate that GXLs have potential applications in photoresist stripping and post-etch residue removal, in which cost savings due to reduced solvent use can be substantial.

The removal of films with GXLs has been evaluated primarily with x-ray photoelectron spectroscopy (XPS). Additionally, an *in situ* optical technique has been developed for film and GXL diagnostics. This mutliwavelenght interferometry (MWI) technique is applied to dissolution of photoresist in aqueous base solutions, swelling of photoresist in solvent vapor, and swelling of photoresist in CO_2 at elevated pressures. MWI has also been used to evaluate the response of PHOST-based thin films to GXLs and to monitor density changes of liquids upon gas expansion.

CHAPTER 1

INTRODUCTION

Some of the greatest innovations of the past half century have involved the integrated circuit (IC) industry and perhaps some of the greatest to come in the foreseeable future will result either directly from semiconductor technology or through mergers with biology and other disciplines. Clearly, chemical engineering plays an important role in the continued development of ICs and related devices. At the core of many of the challenges and opportunities in microelectronics are the basics of chemical engineering, including thermodynamics, fluid mechanics, chemical kinetics and reactor design. Indeed, current limitations in existing ICs such as the microprocessor lie not in device or circuit design, but in our ability to manufacture these reliably and affordably on a large scale.

There are several key areas that represent tremendous challenges for the future of the IC industry, and hence are significant opportunities for research. At no other time in the history of the industry have more new materials been required at the same time. Copper is replacing aluminum as the conductor of choice. New organic materials and porous materials are replacing silicon dioxide as insulators. Substrates other than silicon are being proposed for select applications. However, even these new materials will only meet the demands of the industry over the next half decade – subsequently, additional new materials will need to be developed and implemented. Each new material requires new chemical processes, and each new process will likely require new reactor designs.

A continuing challenge for future ICs is the reduction of feature size in these devices, which is beneficial for two main reasons. First, the time necessary for an electronic signal to propagate is proportional in part to the distance the electron must travel. Secondly, smaller geometries allow more devices to be created per unit area, a tremendous economic advantage. Current state-of-the-art ICs are being manufactured at a characteristic feature size approaching 100 nm, on the order of 1000-times smaller than the diameter of a human hair. New chemical processes and new reactor designs are required to allow further reduction in feature size.

An additional challenge is to not only improve the performance of ICs but to make the cost per function of an IC more affordable. One approach has been to increase the diameter of a silicon wafer, which increases the number of ICs produced in parallel. In the year 2000, the industry increased the standard wafer diameter from 200mm to 300mm. With this change came many technological challenges, including issues with scale-up of reactors for handling these larger dimensions.

To address these challenges, the extension of conventional liquid-phase processes for the manufacture of ICs is uncertain. For example, research on the limitations of HF-based cleaning of deep-submicron features (Baklanov, 1998) indicates that the contact resistance increases significantly as the size of the contact is reduced below 0.45 microns. The authors conclude that "undoubtedly, the application of conventional wet chemistry is facing a turning point in the deep-submicron era".

The use of gas-expanded liquids (GXLs) may be a promising alternative to conventional liquid-phase processes. GXLs have superior transport properties relative to liquids, but can maintain the solvent strength necessary for IC processing steps such as

post-etch residue removal and photoresist stripping. In addition, the environmental benefits associated with CO_2-based processes can be substantial. Although supercritical CO_2 may also be useful, the superior solvent strength and reduced operating pressures are among the advantages of GXLs. The ability to tune physical properties, and thus process performance, by gas-expansion may allow progress in process design to be realized for meeting many of the key challenges of IC processing.

CHAPTER 2

BACKGROUND

2.1 Semiconductor Processing

Since the invention of the integrated circuit (IC) in 1958, the semiconductor industry has boomed to become over a $150 billion market. From the most primitive ICs having only a few components to those of today having more than a billion, advancements in the fabrication of the IC has led to faster and cheaper computing, while devices have become smaller than ever.

The manufacturing of ICs today typically occurs by means of more than 400 processing steps (SIA, 2001). These steps include unit operations such as ion implantation, deposition, lithography, and etching. Precise control of each of these operations is critical for high-yield production of defect-free products. Contamination is a major source of these defects, currently accounting for 50% or more of yield losses in IC manufacturing. Accordingly, among the most numerous processing steps are cleaning operations, often numbering more than 80. Cleaning in general aims at selectively removing unwanted substances to yield a surface having desirable properties. These unwanted substances may include organic films and residues such as photoresist, inorganic materials such as metal oxides or metal salts, or particulates such as those originating from plasma reactors. Semiconductor cleaning specifically encompasses surface preparation and modification, residue removal, photoresist stripping, particle removal, rinsing, and drying.

Since the first development of manufacturing processes for solid-state devices and ICs, cleaning has been performed primarily using liquid phase processes. Two main regimes of cleaning chemistry are designated as front-end-of-line (FEOL) or back-end-of-line (BEOL). Transistors and other devices are fabricated through selective doping of the silicon substrate in FEOL. The standard clean for decades for FEOL has been the RCA clean (Kern and Puotinen, 1970) or modifications thereof. The RCA clean is a multistep process comprised of an NH_4OH/ H_2O_2/DIW (deionized water) bath (Standard Clean 1, or SC-1), a dilute HF dip, an HCl/H_2O_2/DIW bath (Standard Clean 2, or SC-2), and multiple DIW rinse steps. Other FEOL formulations that have been used include ozonated water and the Piranha clean (sulfuric acid/ H_2O_2/DIW)(Kern, 1993).

BEOL refers to all processing beyond the first deposition of metal and includes fabrication of the multiple levels of wiring and insulators used to interconnect the devices. Interconnects are generally fabricated by blanket deposition of a material followed by selective etching. Etching by means of plasmas can be highly anisotropic, is more easily controlled, and produces less waste than with wet techniques. Therefore, plasma-etching processes are used most frequently in critical steps of fabrication. Plasma processes are not without their shortcomings, however. Substrate damage and contamination may be significant.

2.2 Problem Significance

More new materials are being introduced today than at any other time in the history of IC fabrication (Braun, 2001), particularly in BEOL in which new low dielectric constant materials are replacing SiO_2 as the insulator and copper is replacing aluminum

as the conductor. The dual damascene technique is the primary means for building interconnects using copper (DeJule, 2000). Although aluminum metallization involves plasma etching of the metal, dual damascene has been developed due to the nonvolatility of copper etch products. Dual damascene involves selective etching of the dielectric film. Subsequently, copper is electrochemically deposited as a blanket layer and planarized with chemical mechanical polishing (CMP).

A specific challenge is the cleaning of vias. Vias are small holes patterned in an interlayer dielectric to connect two metal layers. These features may prove most difficult to process due to the high-aspect ratio and reduced feature size (sub-100 nm) demanded in future generations of devices, as defined in the International Technology Roadmap for Semiconductors (SIA, 2001) (Table 2.1). The structures that remain after etching vias are patterned layers that may contain numerous post-etch residues. Some of the mechanisms by which these residues will form include:

- The formation of nonvolatile products in secondary reactions between gas phase neutrals and the film to be etched
- Sputtering of the etch mask resulting in redeposition on via sidewalls and bottom
- Back-sputtering of the underlying films once exposed during overetch

Table 2.1. Wiring pitch and aspect ratio are the geometries of interest for cleaning (SIA, 2001).

	1999	2002	2005	2008
Local wiring pitch (nm)	500	365	265	185
Local wiring aspect ratio	1.4	1.5	1.7	1.9

Residues at the bottom, sidewalls, and top of these features can cause poor contact upon subsequent depositions, may alter the properties of low-k dielectric films, and may lower the conductance of metal lines. Inadequate cleans show 1000 times greater dielectric leakage current and a wider capacitance range (Dornisch, Li, and Brongo, 2000). Therefore, these structures must be free of essentially all residues.

The residue that remains after an etching process is dependent upon the dielectric material, the etching gas, and all other exposed materials. The following etch residues have been reported (Dornisch, Li, and Brongo, 2000):

Materials etched:	Etch residues:
SiO_2 based dielectrics with or without dopants such as C, F, N	CF_x-Cu, CH_xF_y, CuF_x, CuO_x
Carbon based low-k dielectric polymers	CuO_x, CH_x

The primary chemical formulations for BEOL cleaning involve hydroxylamine-based chemistries (Lee, 1989). However, these formulations are corrosive to copper and tungsten. Noncorrosive materials such as fluoride-based chemistries have been suggested as alternatives (Kanegsberg, 2001), yet these often result in etching of exposed silicon dioxide. The hydroxylamine- and fluoride-based formulations often contain a mixture of organic solvents and water, in addition to various surfactants to aid wetting. Current commercial formulations have proven to be ineffective in fully removing these etch residues (Louis, 2001). Unless improved solutions are developed, high-yield manufacturing will not be possible for next generation devices.

2.3 Future Process Requirements

Since residue removal plays such an important role in the fabrication of ICs, improvements in this area can have tremendous impact on increasing yield while lowering the cost of the overall process. Research on alternative cleaning processes generally aims at improving one or more of the following:

1. Uniformity
2. Reduction of process time and increased throughput
3. Reduction of toxic chemical and DIW consumption
4. Compatibility with new materials
5. Reduction of residual contaminant concentration

Process time is a very important factor when developing cleaning methods. Batch cleaning in which dozens of wafers are processed simultaneously differs significantly from single wafer processing. A cleaning process that in a batch system could take 30 minutes must occur in minutes in a single wafer tool to ensure adequate throughput. Combining steps or using alternative cleaning processes which do not require distinct rinsing or drying will also reduce processing time, chemical consumption, and process complexity, but yield must not be sacrificed. For example, commercially available formulations for photoresist stripping and etch residue removal must typically be followed by a DIW rinse and a drying step. Using a formulation that does not require separate rinsing and drying steps can lead to significant cost reduction.

The semiconductor industry also constantly strives to reduce the volume of toxic chemicals and water used to process ICs. The safety and health risks associated with the use of toxic chemicals can lead to considerable environmental and personnel concerns

and costs to a company. The massive quantities of DIW consumed at some wafer fabrication facilities (fabs) can put a significant strain on community water supplies (Parker, Chiarello and Gomez, 1998). For these reasons, alternate processes that reduce the use of toxic chemicals and DIW can be of tremendous benefit.

Compatibility and effectiveness of cleaning processes with new materials is crucial. As previously mentioned, more new materials are being introduced today than at any other time in the history of IC fabrication. New cleaning processes must be formulated for compatibility with these new materials (Braun, 2000).

Finally, minimum feature sizes are decreasing to the point where physical properties such as surface tension, viscosity, and diffusivity can limit the effectiveness of currently available cleaning formulations; this results in sub-optimal yield. Understanding these physical property effects on cleaning performance is needed if yield is to be maximized.

CHAPTER 3

GAS-EXPANDED LIQUIDS

3.1 Introduction

Liquid-phase processing is used routinely in the fabrication of integrated circuits (IC), microelectromechanical systems (MEMS), and nano-structured devices (Campbell, 1996). Specifically, liquid-phase process steps include rinsing, cleaning, surface conditioning, photoresist stripping, and post-etch residue removal. The liquids used range from organic to aqueous and acidic to basic, but they often share the common property of being environmentally hazardous with regard to flammability, human health, and pollution. In addition, limitations may exist in the use of liquids to process nanoscale features. For instance, viscosity, surface tension, and diffusivity of liquids may inhibit mass transport and surface wetting.

Carbon dioxide has been suggested as an alternative to traditional liquids for surface cleaning and photoresist development (SIA, 2001). Carbon dioxide is relatively benign in terms of flammability, toxicity, and environmental impact. In addition, CO_2 physical properties include a significantly lower viscosity and surface tension, and a greater diffusivity than liquid counterparts, which suggest the possibility of improving mass transport and wettability. However, carbon dioxide is often a poor solvent in the liquid phase and is even less effective in the supercritical phase. Some solubility of materials such as silicones and fluorocarbons is possible, but other materials, especially those with polar moieties, are essentially insoluble.

Due to their unique range of properties, gas-expanded liquids (GXLs) may overcome the limitations of traditional solvents, pure CO_2, and supercritical mixtures of these components. The physical properties of GXLs range between those of the pure components, suggesting that excellent mass transport and excellent solvent strength are possible. For example, the solvent strength of GXLs is much greater than that of gases or supercritical fluids, while the surface tension and viscosity of GXLs is much lower than that of liquids. This is depicted in Figure 3.1.

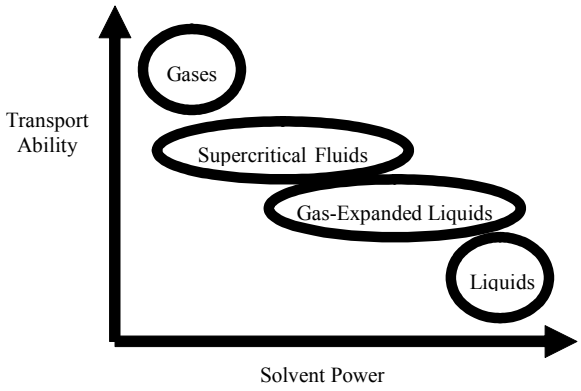

Figure 3.1. Comparison of various classes of fluids.

Consider a closed system in which carbon dioxide is in equilibrium with a solvent such as ethanol. At low pressures (~ 1 atm), the amount of carbon dioxide that is in the liquid phase is minimal. However, at elevated pressures, carbon dioxide may have significant solubility, and the total volume of the liquid phase will increase (Chang et al., 1998). This new liquid is termed a GXL. When the pressure approaches the vapor pressure of CO_2, the fluid volume is entirely liquid. Therefore, the composition of the liquid can be varied from that of essentially pure solvent to that of essentially pure liquid carbon dioxide if the components are miscible.

GXLs have been utilized for crystallization (Bertucco, 1999) and other separation applications (Lee, Olesik, Fields, 1995)(Chang, Randolph, 1991)(Eckert, Bush, Brown, Liotta, 2000). However, to the authors' knowledge, no studies have been reported where applications of GXLs in microelectronics processing have been investigated. This class of liquids may be particularly useful for photoresist and residue removal.

3.2 Physical Property Modification

As the composition of a GXL is modified, the physical properties (viscosity, diffusivity, density, etc.) are similarly modified over the range of the pure component properties. Hence the properties of the liquid phase (e.g., for solubilization of residues, removal of photoresists, penetration of shallow trenches) are tunable (West, 2001).

The physical parameters of a GXL as a function of composition can be approximated from pure component data. For example, the dependence of properties upon the composition of CO_2-expanded ethanol will be considered. The physical properties of these components in Table 3.1 gives an indication of the range over which the properties of a GXL may be tuned.

Table 3.1. The viscosity (μ), surface tension (γ), and density (ρ) of ethanol and liquid carbon dioxide (DIPPR, 2002).

	EtOH	L-CO_2	units
$\mu \downarrow$	1.0	.06-.09	mPa-s
$\gamma \downarrow$	22	1.5	mN/m
$\rho \sim$	790	1100	kg/m^3

The dependence of physical property modification upon composition is of interest, particularly for estimating the impact of gas expansion upon process factors such as wetting and transport (Chapter 4 and 5). For the ratio of the density of a GXL to that of a pure liquid, experimental data is available (Chang, 1998) and at 298 K:

$$\frac{\rho_{GXL}}{\rho_L} = -0.092x + 1.092 \qquad [3.1]$$

where ρ is density and x is the mole fraction of ethanol in the liquid phase.

The viscosity of a binary liquid mixture is interpolated from the pure component viscosity as (Poling et al., 2001)

$$\ln \mu_{mix} = x_1 \ln \mu_1 + x_2 \ln \mu_2 + x_1 x_2 G_{12} \qquad [3.2]$$

where G_{12} is an empirical interaction parameter. If the interaction is assumed to be minimal and this parameter is neglected, Equation 3.2 reduces to

$$\mu_{mix} = \mu_1^{x_1} \mu_2^{x_2} \qquad [3.3]$$

Therefore, for a GXL, the viscosity ratio is

$$\frac{\mu_{GXL}}{\mu_L} = \mu_{CO_2}^{1-x} \mu_L^{x-1} = (0.064)^{1-x} (1.06)^{x-1} = (16.56)^{x-1} \qquad [3.4]$$

The viscosity (DIPPR, 2002) (in mPa-s) at 298 K for ethanol is ~1.06, and that of liquid CO_2 is 0.064.

Correlations exist to approximate values of diffusivity. One such correlation is the Wilke-Chang equation for diffusivity given by (Middleman, *Transfer*, 1998)

$$D = 7.4 \times 10^{-8} \frac{(\phi M_B)^{1/2} T}{\mu_B V_A^{0.6}} \qquad [3.5]$$

where M is the molecular weight of the solvent, V is the molal volume of the solute, and ϕ is a solvent association factor. For non-hydrogen-bonded solvents such as CO_2, $\phi = 1$.

For ethanol, $\phi = 1.5$. It is assumed for simplicity that ϕ_{GXL} is the weighted average of the pure component ϕ's and, by definition, M_{GXL} is the weighted average of the individual molar masses. Therefore the ratio of the diffusivity for this correlation is

$$\frac{D_{GXL}}{D_L} = \left[\left(\frac{\phi_{CO_2}}{\phi_L}(1-x) + x \right) \left(\frac{M_{CO_2}}{M_L}(1-x) + x \right) \right]^{0.5} \frac{\mu_L}{\mu_{GXL}} \qquad [3.6]$$

The concentration ratio may be calculated if solubility data for a solute of interest exists. However, if this information is unavailable, it is assumed that the solubility in CO_2 is much less than in the solvent (ethanol in this case) and if the solubility of the GXL is assumed to follow a linear function of the pure component solubility, the ratio is simply x.

These functions for physical properties vs. GXL composition are useful for estimating processes dependent on these properties, such as wetting and transport.

3.3 CO_2 Expansion of Organic Solvents

Many organic solvents are completely miscible with CO_2, resulting in a single liquid phase. Two such solvents commonly used in microelectronics processing are ethanol and n-methyl pyrrolidone (NMP). Equilibrium data for these materials is plotted in Figures 3.2 and 3.3. NMP and ethanol mixtures with CO_2 are representative of ideal liquid mixtures and are well characterized by Raoult's Law. Water, however, is not miscible with CO_2 and therefore cannot be significantly expanded.

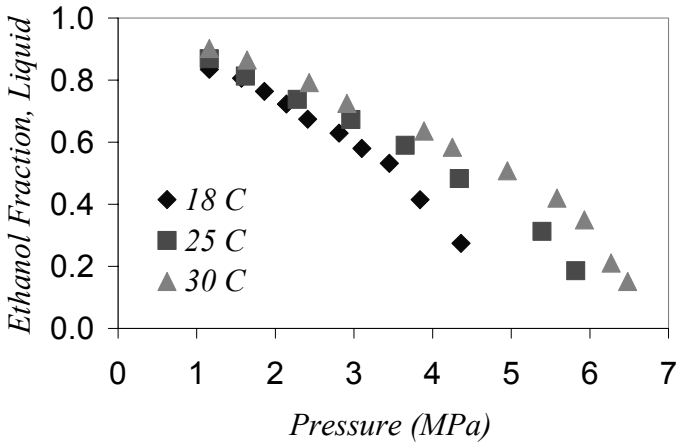

Figure 3.2. Pressure-composition data for GXLs of CO_2 and ethanol at 18°C, 25°C, and 30°C (Chang et al., 1998).

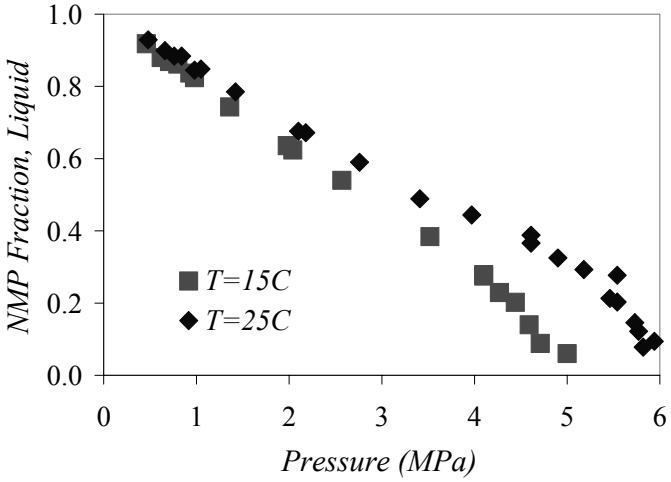

Figure 3.3. Pressure-composition data for GXLs of CO_2 and NMP at 15°C and 25°C (Zubchenko, 1985).

GXLs are formulated in the laboratory using the equipment illustrated in Figure 3.4. Two high pressure syringe pumps (ISCO, Inc.) are used. Pump A is operated in constant pressure mode for maintaining the pressure setpoint (and thus composition) while Pump B is operated in constant flow mode and used for controlling the delivery of liquid. Care is taken to ensure adequate mixing of CO_2 and the solvent at the temperature

and pressure of interest so that the composition of the liquid is controllable and able to be estimated from literature data.

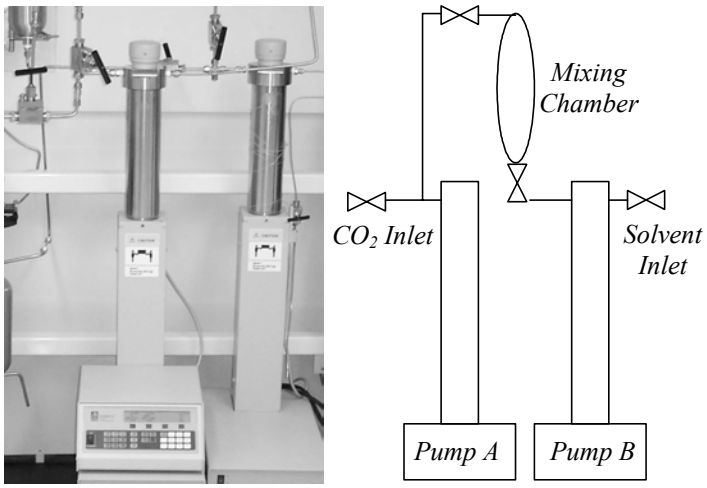

Figure 3.4. Two high pressure syringe pumps are used to formulate and deliver GXLs. A schematic diagram of the pumps and mixing chamber is shown on the right.

Pump B is first loaded with the solvent of interest. When the system is depressurized and all valves are closed, the liquid inlet valve on Pump B is opened and the inlet tube is placed in a beaker filled with the solvent. During filling of the pump, the tube inlet is fully submersed in the liquid. The refill rate of Pump B is set at approximately 40 mL/min. Filling of the pump is stopped after it is loaded with the desired amount of solvent. The liquid inlet valve is then closed and the pump contents are delivered to the liquid mixing chamber.

To pressurize the system with CO_2, the CO_2 cylinder is opened to Pump A. Pump A is filled to a sufficient volume such that the GXL can equilibrate and the experiment can be run at a rate of ~100 mL/min. After the pump is full the valve to the mixing chamber is opened. The CO_2 cylinder valve is opened just enough to approach the

pressure setpoint. Pump A is operated in constant pressure mode at the setpoint. If Pump A empties, the CO_2 cylinder is again briefly opened.

To enhance the mixing of solvent with CO_2, the mixing chamber is periodically agitated. Also Pump B is set to automatically refill to 55 mL when emptied while delivering at a rate of 30 mL/min. This will cause the pump to continually deliver and draw liquid into and out of the mixing chamber. This status is maintained for several hours to ensure sufficient mixing.

To maintain control of the vapor-liquid phase equilibrium concentrations, each region of the equipment through which fluid is transported must be maintained at the specific temperature setpoint of the particular experiment. Any deviations from this setpoint will shift concentrations in the fluid. Therefore, the pumps, mixing chamber, lines, and sample chamber are each equipped with an independent heater and thermocouple. The temperature is controlled with a single multi-zone controller. Most experiments, however, have been performed at room temperature.

Two techniques have been used to check qualitatively the agreement of GXL composition formulated in the lab with reported literature data. First, a known amount of GXL is delivered to an expansion vessel, allowing CO_2 to flash. The remaining volume of solvent is collected. Following the aforementioned procedure for formulating GXLs, reasonable agreement with literature data is obtained. For example, NMP was mixed with CO_2 at 5.0 MPa and 22.5°C, which according to reference data should yield a GXL of 70mol% CO_2 with a molar volume of 60 mL/mol. This should yield a volume of solvent after flash equal to 50% of the GXL volume. Following the procedure for obtaining a well mixed GXL, 25 mL were collected from 50mL of GXL. However, for

an inferior mixing procedure (insufficient time and mixing), 40 mL were collected from 50 mL of GXL.

Second, using an optical technique detailed in Chapter 6, the refractive index of the GXL is monitored. The refractive index of a mixture can be calculated from pure component properties using the Lorentz-Lorenz mixing rule. This is given by:

$$\frac{n_{mix}^2 - 1}{n_{mix}^2 + 2} = \sum \frac{\rho_i R_i}{MW_i} \qquad [3.7]$$

where R_i is the molar reflectance, MW_i is the molecular weight, and ρ_i is the density, all of component i, and n_{mix} is the refractive index of the GXL. CO_2-expanded ethanol at 5000 kPa and 22.8°C, for example, had a refractive index of 1.234. This is comparable to the predicted refractive index using Equation 3.7 of 1.240. Unfortunately, complementary techniques for comparatively measuring the refractive index of these high pressure liquids are not available.

3.4 CO_2 Expansion of Organic Bases

Although photoresist residue can often be removed using traditional solvent formulations, more extreme processes such as plasma etching, ion implantation, and thermal annealing yield photoresist residue that can only be removed with more aggressive chemistries. Commercial formulations for these applications primarily contain amines as the reactive component. Therefore, CO_2 expansion of these types of formulations has been investigated.

DuPont-EKC Technologies (Hayward, CA) is one supplier of commercial formulations used for photoresist removal. Two specific products were targeted for

investigation of gas expansion, EKC 505 and EKC 830, both of which are nonaqueous formulations containing amines.

EKC 505 primarily contains NMP, morpholine, and butyrolactone. These molecules and others referred to in this section are pictured in Figure 3.6. This formulation yields a precipitate upon mixing with CO_2, as can be seen simply by bubbling CO_2 through this formulation contained in a beaker. CO_2 reacts with the amine to form an insoluble product. This reaction has been described in the literature (Versteeg and Swaaij, 1988) to proceed as

$$CO_2 + R_1R_2NH \leftrightarrow R_1R_2NCOOH \qquad [3.8]$$

$$R_1R_2NCOOH + R_1R_2NH \leftrightarrow R_1R_2NCOO^-R_1R_2NH_2^+ \qquad [3.9]$$

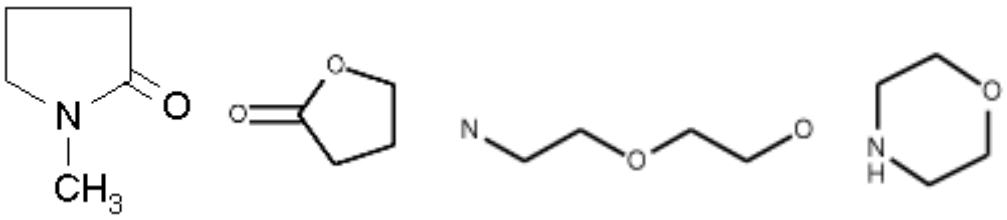

Figure 3.6. Molecular structures of, from left to right, NMP, butyrolactone, 2-(2-aminoethoxy)ethanol, and morpholine.

EKC 830 is a mixture of NMP and 2-(2-aminoethoxy)ethanol. Bubbling CO_2 through this formulation in a beaker does not produce solid, although the liquid becomes highly viscous. If a reaction occurs, the product remains soluble. The significant temperature rise observed suggests that this reaction does occur. Using a Jurgeson gauge, the formation of a solid is observed at elevated pressures.

CO_2 is clearly not an inert component in these mixtures. Indeed, CO_2 is a Lewis acid, and thus interactions with bases will occur. This suggests there may be opportunities to design novel formulations for use with CO_2. Tertiary amines, for instance, have been reported to not react with CO_2 in nonaqueous solvents.

To explore the interaction of CO_2 with tertiary amines, triethylamine was mixed with CO_2 both in a beaker and at elevated pressure. Beaker experiments suggested no reaction; that is, heating and precipitation as observed in experiments with primary and secondary amines did not occur. Even at elevated pressures up to 5.5 MPa, no sign of reaction is observed. However, this decrease in reactivity of the amines with CO_2 quite possibly coincides with a decrease in reactivity of a tertiary amine with photoresist residues. Indeed, no commercial formulations are known to contain tertiary amines.

3.5 High Pressure ATR-FTIR

Understanding the compositional changes of a remover formulation upon CO_2 expansion can be greatly aided with FTIR. For such analyses, a high pressure cell has been modified and optimized so that GXL compositions may be investigated. The general design has been previously described (Kamal, 2000), but does not adequately hold pressures up to 1000 psi. O-ring design tools are provided by many suppliers of o-rings. An online o-ring seal design tool by Apple Rubber Products was used to modify and improve the design of the FTIR high pressure cell. In particular, the mobility of the o-ring within the groove must be minimized in order to avoid excess fatigue. Therefore, the o-ring outer diameter (OD) must be at least equivalent to the groove OD or up to 1%

larger. The groove OD of the cell is 1.783", but the original o-rings used have an OD of 1.674".

The most likely source of failure, however, relates to two bolts that support the crystal in the cell. The area of the crystal exposed to elevated pressure is 2.0 square inches. For a pressure of 1000 psi, 2000 lbs of force are applied to the crystal, and consequently directed on two bolts, #4-40. These bolts have a tensile area of 0.00604 square inches; thus, the pressure they each support is over 160,000 psi. Since the tensile strength of steel is about 60,000 psi, this is likely a source of failure. Indeed, the support beam was observed to have bowed under the force directed upon it.

The new design consists of a new bottom plate for supporting the crystal (Figure 3.7). The plate is supported along the periphery by 8 #4-40 bolts. The dimensions of the plate are machined such that the gap between the crystal and reactor top is precisely maintained to avoid extrusion of the o-ring. However, this new design will only be effective if the tolerance of the dimensions determining the clearance gap is much less than the gap clearance itself. Even with precision machining of the cell and plate, the crystal has a tolerance on the order of the gap. Therefore the plate support must be used only with a crystal of a particular thickness. To be able to interchange crystals, multiple plate supports machined appropriately for the gap must be fabricated. This new design was found to effectively hold pressurized CO_2 up to 6 MPa. This pressure capability allows analysis of GXLs.

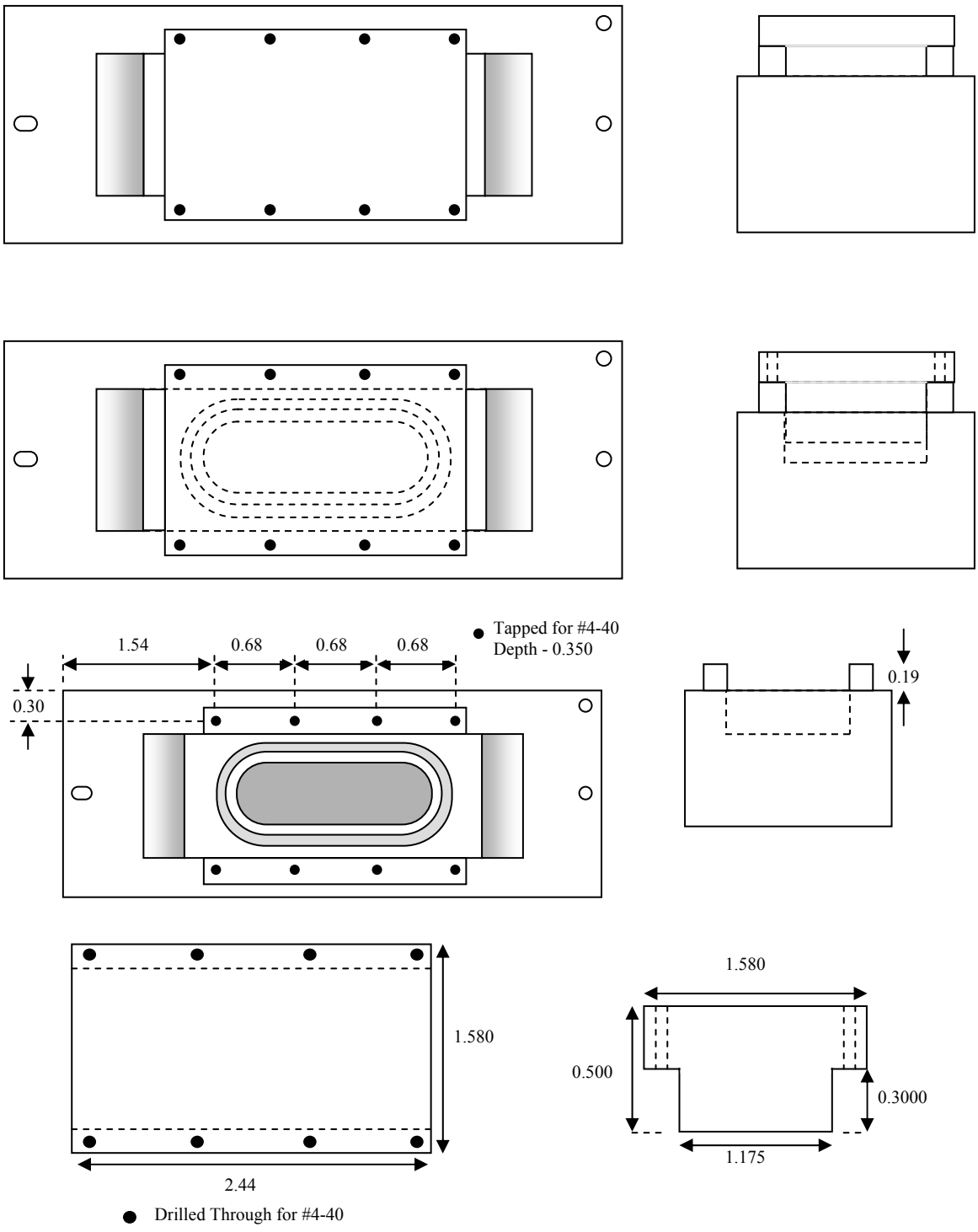

Figure 3.7. Diagrams of the modified high pressure FTIR reactor.

3.6 Environmental, Safety, and Health Issues

In order to more fully exploit the opportunities to minimize environmental impact, the post-processed solvent within a GXL (after a photoresist removal process) can be collected by reducing the pressure to separate CO_2 from the solvent and thus obtain an estimate of the amount of CO_2 recoverable. Presumably the large differences in vapor pressures will yield opportunities for recycling CO_2.

Also, calculations can be performed to estimate the advantages possible with respect to flash point and flammability limits of GXLs relative to pure solvents. These property values can be approximated from pure component data (Crowl and Louvar, 1999). Because the GXL is formed in a closed system, under elevated pressure, flammability is only an issue if a leak develops in the system. The lower flammability limit for ethanol, for example, is 3.7%. However, the composition of CO_2 in the vapor head of a GXL is always greater than 98% (Chang, 1998) in the pressure and temperature range of interest (4-6 MPa and 290-315 K), yielding an inflammable mixture if a leak develops from the gas phase. A leak from the liquid phase of a GXL will lead to a flash separation of CO_2 vapor from the flammable liquid, resulting in no change in flammability from the pure solvent.

A full cost analysis is necessary to determine if GXLs can be used commercially. While not all costs are known, some estimates can be readily performed. Cost factors for pressure vessels are available (Peters, 1991); a reactor operating at up to 800 psig costs 3.8 times that of a reactor operating at up to 50 psig. However, a reactor operating at up to 3000 psig, as what might be of interest in supercritical fluids, costs 8.8 times that of the 50 psig vessel.

The increased capital and operating costs expected with high pressure equipment can be offset if the volume of consumables can be reduced. Recent data from TSMC, a manufacturer of ICs, indicates chemicals used for processes such as cleaning account for 18% of the total material costs in IC manufacturing (Tracy, 2003). These chemical costs are second only to wafer costs at 47.4%.

SEMATECH, a consortium of IC manufacturers, offers a fab simulation and economic modeling tool from which the cost of consumables is estimated to be 5 times that of equipment costs (Table 3.2). If these figures are representative of actual costs, this suggests that even a small decrease in the volume of chemicals consumed will compensate for increased operating and equipment costs for high pressure operation.

Table 3.2. Economic factors for estimating the ratio of the cost of consumables to the cost of equipment.

Consumables per wafer	$25
Wetbench with 125 wafers/hr throughput	$2,000,000
Equipment Depreciation	5 years
Equipment Installation	15%
Equipment Maintenance	7.5%
Equipment Downtime	5%
Cost of Consumables/Cost of Tool	5

3.7 Conclusion

Gas-expanded liquids possess improved transport properties relative to liquids, but are superior solvents in comparison to supercritical fluids. Therefore, GXLs may prove useful as alternatives to conventional liquids for cleaning processes, and preliminary cost estimates suggest feasibility. Models for physical property estimation have been applied for predicting properties of GXLs as functions of CO_2 concentration. Equipment capable of forming and delivering GXLs has been designed, assembled, and

optimized. With this equipment, GXLs of varying composition can be studied. Gas-expansion of organic solvents has been observed to correspond well with literature pressure-composition data, but CO_2-expansion of solvents containing primary and secondary amines yields precipitation of reaction products. Tertiary amines may alternatively prove useful as components in CO_2-based fluids, and future work may investigate the applicability of tertiary amines in cleaning formulations. A high pressure ATR-FTIR cell has been redesigned and fabricated for studying the compositions of these GXLs. The increased operating and capital costs of high pressure equipment may be more than offset by the reduced cost of consumables in GXLs since these consumables currently contribute significantly to the total process cost of ownership.

CHAPTER 4

WETTING

4.1 Introduction

To evaluate the extendibility of liquid processes to the fabrication of future device generations (i.e., smaller geometries) and for the design of new processes, the physical parameters (Table 1) of the processing fluids, reactor design, and device structures must be correlated to the process figures of merit. Specifically, for surface cleaning or preparation, film removal (i.e. photoresist stripping, chemical etching), and film deposition (i.e. spin casting, electroplating), these figures of merit include throughput (or processing time), chemical consumption, uniformity, etch/deposition rates, and especially cost.

Table 4.1. Variables to be considered in the design of a liquid process.

Category	Variable
Liquid Properties	Viscosity, surface tension, density
Geometrical Parameters	Feature size, aspect ratio, pitch
Processing Conditions	Pressure, temperature, flow rate, flow profile
Other Liquid Related Properties	Contact angle, diffusivity, solubility

Any liquid-phase process must begin by complete wetting of the surface. Efforts to model liquid-phase processes and the various steps of the process mechanism (Mazouchi, Homsy, 2001)(Takahashi, Gross, 1999)(Lin, Busnaina, Suni, 2000)(Hebda, et al, 1999)(Olim, 1997) generally neglect this initial wetting step by assuming that complete surface wetting occurs instantaneously. However, this assumption may be invalid if wetting is obstructed in features such as high aspect ratio vias and trenches, and

on surfaces that exhibit a high contact angle with process liquids, i.e. organic polymer dielectrics in contact with aqueous solutions.

One study (Olim, 1997) investigates the wetting mechanism but concludes that wetting time is an insignificant contributor to total processing time; for example, a 0.5 μm wide feature with a height of 4 μm was estimated to completely wet in less than 1 s (Olim, 1997). This study was performed for specific liquid properties in which the displacement of gas by a wetting liquid is modeled in the limit of steady-state transport dominated by diffusion only in the feature. The time-dependence of wetting and the resistance to mass transfer outside of the feature are neglected. This chapter accounts for these issues for various fluid properties by detailing the wetting mechanism and by modeling the transport processes involved. From this model, an expression is derived to calculate the wetting time for features of cylindrical geometry. The wetting time is related directly to parameters that may be tuned in a cleaning process (e.g. surface tension or contact angle) and specifically to how the wetting time varies with feature width and height. This analysis identifies those conditions under which the wetting time may be a significant contributor to total process time.

4.2 Wetting Impedance: Gas Cavity Formation

In the typical situation of a liquid wetting a surface initially in contact with a gas, the liquid must fully displace this gas. Fundamental fluid mechanics describes this dynamic wetting process (de Gennes, 1985). A contact line is defined as the interface between the vapor, liquid and solid; pinning of this contact line may occur on rough surfaces and is exacerbated when the roughness is extended to deep parallel grooves. A

description of this case can be formulated by identifying a metastable "composite" surface (Dettre, Johnson, 1964). Here, the entrapment of gas cavities (G) between the liquid (L) and solid (S) can occur, as shown in Figure 4.1 for an arbitrary feature shape. The dynamics of this wetting process are complex, but formation of such a cavity is a possible scenario, particularly with high aspect ratio structures.

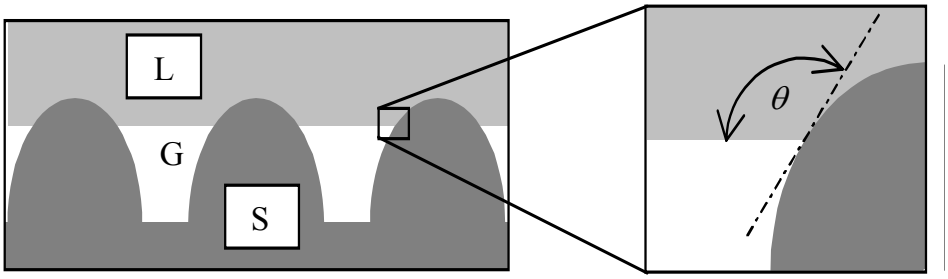

Figure 4.1. A nonplanar solid surface (S) with trapped gas cavities (G) formed with a liquid (L) at contact angle, θ.

The liquid contacts the walls of the solid features with angle θ, which depends upon the relative interfacial tensions of the solid, liquid, and gas. Only if the solid has a greater affinity for the liquid than for the gas (the contact angle is less than 90°) will the feature wet.

The formation of a gas cavity will occur only in features of sufficient depth. Therefore, a simple geometrical analysis can be performed to estimate the critical aspect ratio (h/w) above which a gas cavity will form. For shallow features, an advancing liquid with a contact line approximated by a straight line will contact the feature bottom prior to contacting the opposite side of the feature and the feature will immediately wet. However, if the liquid contacts the opposite side of the feature before contacting the

bottom, gas will be trapped in the feature (Figure 4.2). The critical aspect ratio above which a gas cavity will form is equivalent to $\cot\theta$.

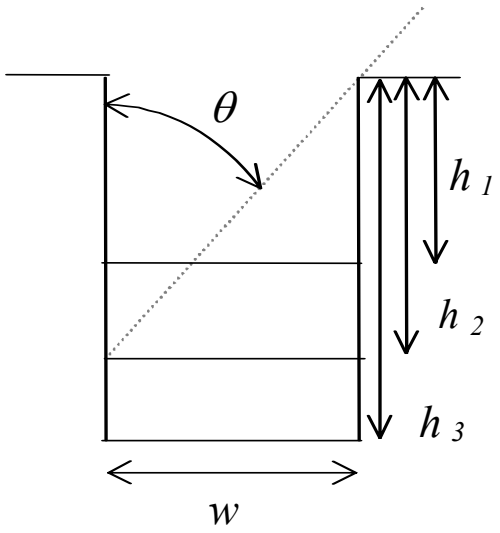

Figure 4.2. For a feature with height h_1, liquid will fully wet the feature while that with height h_3 will form a gas cavity. Height h_2 defines the critical aspect ratio, $\cot\theta$.

The result of the liquid contact in the feature is a curved interface, across which a pressure difference exists as described by the Young-Laplace Equation (Middleman, Fluids, 1998)

$$\Delta P_{\text{int}} = \gamma\left(\frac{1}{r_1}+\frac{1}{r_2}\right) \qquad [4.1]$$

where r_1 and r_2 are radii of curvature of the interface, and γ is the gas-liquid interfacial tension. For a cylindrical feature, $r_1=r_2$, and after a trigonometric substitution relating the curvature to the contact angle, θ, and feature width, w, this expression becomes

$$\Delta P_{\text{int}} = 4\frac{\gamma\cos\theta}{w}. \qquad [4.2]$$

Any gas initially contained in a cylindrical feature may be trapped and compressed as the fluid flows into the feature as a result of the developed pressure gradient (Figure 4.3). A similar analysis can be performed on a trench structure. In this case, the radius of curvature is infinite in one dimension, and Equation 4.1 reduces to

$$\Delta P_{\text{int}} = 2\frac{\gamma \cos\theta}{w}. \qquad [4.3]$$

However, the probability of cavity formation likely decreases as the length of the trench increases because a larger area must be enclosed by the liquid for gas to be trapped. The detailed dynamics of this wetting process are beyond the scope of this study.

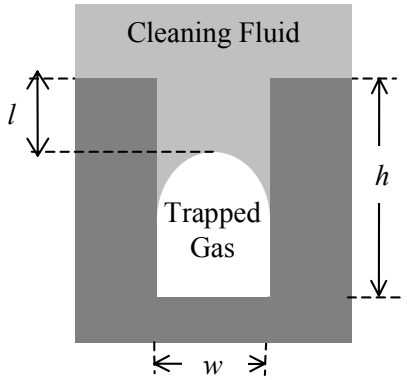

Figure 4.3. An illustration of the geometry defined to describe feature wetting.

The interface will approach a quasi-equilibrium position as the gas cavity is compressed and the pressure gradient approaches zero. The rate at which the liquid flows into the feature is given by the Hagen-Poiseuille Equation for laminar flow in a cylinder (Bird, Stewart, Lightfoot, 1960):

$$u_{avg} = \frac{dl}{dt} = \frac{\Delta p w^2}{32 l \mu} \qquad [4.4]$$

where u is the average velocity and μ is the viscosity of the liquid. In Equation 4.4, the pressure gradient, Δp, is the difference between the equilibrium feature pressure and the instantaneous feature pressure, $hP_O/(h-l)$. These expressions describing the compression of gas in a capillary have analogously been derived for flow in porous media (Churaev, 2000).

The time, t_p, required for liquid incorporation into the feature can be estimated by integrating Equation 4.4. If it is assumed that the liquid traps the volume of gas initially in the feature and that the gas behaves ideally, solving for the time necessary to move a length, l, yields:

$$t_p = \frac{32\mu}{w^2}\left(\frac{l^2}{2P_f} - \frac{hP_O l}{P_f^2} + \frac{h^2 P_O\left(P_O - P_f\right)}{P_f^3}\ln\left(\frac{h\left(P_O - P_f\right) + P_f l}{h\left(P_O - P_f\right)}\right)\right) \qquad [4.5]$$

The physical equilibrium position of the interface is found from the ratio

$$\frac{h - l_e}{h} = \frac{P_O}{P_f} \qquad [4.6]$$

where l_e is the equilibrium distance from the top of the feature, h is the height of the feature, P_O is the initial pressure of the gas (generally 1 atm) and P_f is the equilibrium pressure in the feature. This feature pressure is the sum of the curved interface pressure drop (ΔP_{int}), the pressure from the weight of the fluid, and the externally applied pressure (generally 1 atm). The curved interface pressure drop is especially significant for reduced feature sizes, as demonstrated by Equation 4.2 and illustrated in Figure 4.4.

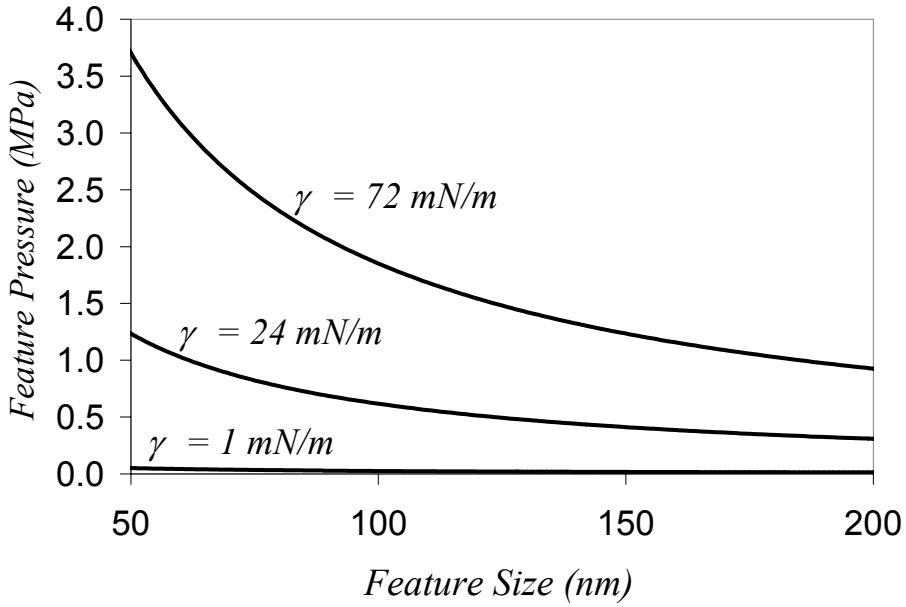

Figure 4.4. The feature pressure increases exponentially as the feature size is reduced. The plot illustrates this trend for surface tensions of (a) 72, (b) 24, and (c) 1 mN/m.

There are two important manifestations of the feature pressure. First, the pressure can be correlated to the solubility of the gas in the liquid through Henry's Law or other thermodynamic equilibrium data. Second, this pressure may lead to mechanical failures in the structure, particularly for new materials such as polymers or porous materials that generally have poorer mechanical strength than dielectrics such as SiO_2. Although work on pattern collapse attributes feature deformation to the drying step, it is possible that this may also occur during wetting in which even greater capillary pressures may develop. For weak structures such as freestanding lines, collapse has been reported to occur during drying (Namatsu, et al, 1995). Using Equation 4.3, the pressure leading to collapse of these features can be at most 0.1 MPa. (Although the pressure drop calculated from Equation 4.6 is much larger, the absolute pressure in the feature cannot be less than zero.) For mechanically stronger structures such as vias and contact holes, pressures necessary

to cause collapse are likely on the order of the material's modulus, which for new dielectric materials such as porous MSQ have been reported to be ~1 GPa (Mogilnikov, Baklanov, 2002). This topic is discussed in detail in Section 4.6.

4.3 Complete Wetting through Gas Transport

If the gas trapped in the feature is insoluble in the liquid, the feature does not fully wet. However, since gases are generally slightly soluble in liquids, the gas will diffuse into the liquid, ultimately allowing the feature to completely wet. The flux of gas into the liquid as a function of time is proportional to the concentration gradient at the liquid-gas interface. Thus, the concentration profile of gas in the liquid can be calculated by performing a mass balance on a differential element of the liquid as given by

$$\frac{\partial C}{\partial t} = D\nabla^2 C - u\nabla C \qquad [4.7]$$

where D is the diffusivity of gas in the liquid and u is the liquid velocity. This partial differential equation does not have an analytical solution. Solution of Equation 4.7 is simplified tremendously if either of two assumptions can be made. First, if the system is at steady state, an analytical solution is possible when a correlation for a mass transfer coefficient is invoked. Second, by assuming that diffusion is the dominant transport mechanism, the convection term may be neglected, and a simplified solution is possible through combination of the temporal and spatial variables. These simplifying assumptions can be validated only after solution of the complete equation.

A general model for the velocity profile can be obtained by considering flow past a flat plate with a coordinate system depicted in Figure 4.5, with a no-slip boundary condition ($u=0$) specified at the surface. Although the substrate of interest is nonplanar,

the flat plate model will be a valid approximation since the flow is approximately equal to zero within the features as well (Nakao, et al, 1990). Because the flow profile is nearly unidirectional, diffusion dominates in the y-direction (in the limit of tightly packed features – otherwise radial diffusion occurs), and convection dominates in the x-direction. Therefore, Equation 4.7 becomes

$$\frac{\partial C}{\partial t} = D\frac{\partial^2 C}{\partial y^2} - u_x \frac{\partial C}{\partial x}. \qquad [4.8]$$

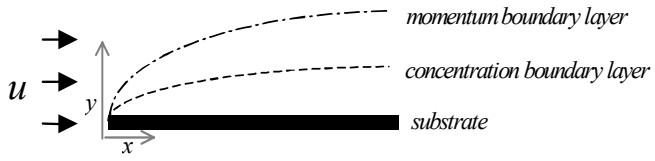

Figure 4.5. The momentum and concentration boundary layer for flow past a flat substrate.

Transport of gas into the liquid occurs primarily through diffusion from the gas cavity interface to the top of the feature, and then by both convection and diffusion into the bulk liquid. Initially, the resistance to transport in the feature will be neglected to simplify the model and *y=0* is defined as the position at the feature top.

The finite difference method has been used to solve Equation 4.8 in MATLAB, (this code is included in Appendix A) using central differences to define the spatial derivatives on the interior nodes and forward and backward differences on the boundaries and for the time derivative. The geometry is defined in the x-direction by the length of a wafer (300-mm) and in the y-direction by a distance into the liquid, *d*. The velocity profile is estimated by (Cussler, 1999)

$$\frac{u_x}{u_O} = \frac{3}{2}\frac{y}{\delta} - \frac{1}{2}\left(\frac{y}{\delta}\right)^3 \qquad [4.9]$$

within the laminar boundary layer, δ given by (Cussler, 1999)

$$\delta = \sqrt{\frac{280\mu x}{13 u_O \rho}}\,. \qquad [4.10]$$

This velocity profile will be applicable until the transition to turbulence (Middleman, Fluids, 1998)[16] occurs at $u_0 x/\nu = 5\times10^5$. For aqueous solutions (kinematic viscosity, ν, is 10^{-6} m^2/s) and a 300 mm substrate, the velocity profile is valid when $u_0 < 1.6$ m/s. Above this velocity, a model for turbulent boundary layer flow must be used.

Henry's Law can be used to correlate concentrations with pressures through the relation $P = k_H C$, where k_H is the Henry's Law constant. It as assumed here that the time for transport is much larger than the time for Poiseuille flow and that the pressure within the feature, P_f, is constant. (In all calculations performed in this study, the time for Poiseuille flow was at least 1000 times less than the time for transport, supporting the assumption). The concentration at the surface is initially proportional to the gas pressure in the feature, and this concentration will remain constant until the gas has been entirely transported from the surface.

From the concentration profile, the surface flux can be calculated as a function of position and time. Integrating this flux with respect to time yields the total amount of gas transported into the liquid. The time at which this total equals the amount of gas initially in the feature (estimated using the ideal gas law) is the time at which the feature is completely wet.

The above approach was used to calculate feature wetting times for a range of liquid velocities; one particular result is shown in Figure 4.6. It is clear that velocities as

large as 25 m/s do not influence the total wetting time in this example. This important result indicates that under some conditions, the transport is diffusion limited. As a result the velocity term in Equation 4.7 can be neglected, and a simple expression for wetting time may be found for diffusion-limited conditions.

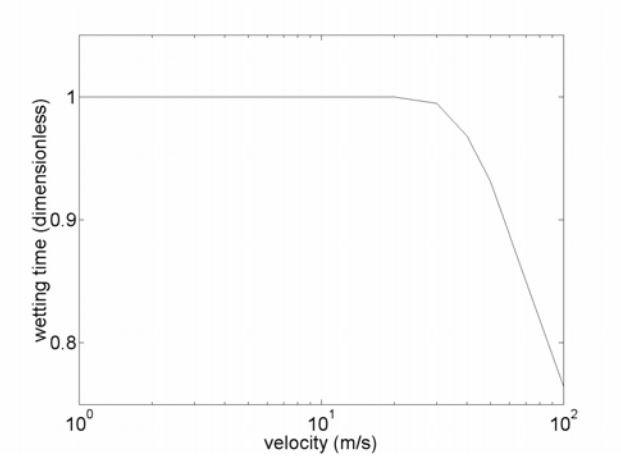

Figure 4.6. The wetting time is independent of the liquid velocity up to 20 m/s for a feature with 150-nm diameter and 1.2 μm depth.

The particular velocity below which the system is diffusion limited is a function of the feature geometry and the fluid properties. This critical velocity, u_c, below which transport is diffusion dominated, is found numerically to be given by

$$u_c \leq 1.63 \frac{L}{t_d} \left(\frac{\nu}{D} \right)^{1/3} . \qquad [4.11]$$

where t_d is derived below. In addition, it should be noted that the concentration profile is strongly time-dependent at these time scales. This indicates that a steady-state approximation to Equation 4.8 would yield an inaccurate solution to this problem.

4.4 Diffusion-Dominated Transport

When the convection terms can be assumed negligible, Equation 4.8 becomes

$$\frac{dC}{dt} = D\frac{d^2C}{dy^2} \qquad [4.12]$$

where the transport both in and out of the feature is now accounted for by defining *y=0* as the position of the liquid-gas interface. By combining variables *t* and *y* into the quantity ζ, where (Middleman, Mass, 1998)

$$\zeta = \frac{y}{\sqrt{4Dt}} \qquad [4.13]$$

an ordinary differential equation of the following form results:

$$\frac{d^2C}{d\zeta^2} = -2\zeta\frac{dC}{d\zeta} \qquad [4.14]$$

With the previously defined boundary conditions, the solution to Equation 4.14 is

$$C_O - C(\zeta) = (C_O - C_B)erf(\zeta). \qquad [4.15]$$

where C_O and C_B are the concentrations of gas at the cavity interface and in the bulk liquid, respectively.

From Equation 4.15, the total amount of gas transported into the liquid, *M*, can alternately be found by integrating the concentration profile from *y=0* to infinity at the wetting time, t_d, yielding

$$M = \int_0^\infty (C - C_B)dy = (C_O - C_B)\int_0^\infty (1 - erf\zeta)dy \qquad [4.16]$$

In this integral, the *y* dimension can be converted to ζ:

$$d\zeta = \frac{dy}{\sqrt{4Dt}} \qquad [4.17]$$

so that M can be expressed as

$$M = (C_O - C_B)\sqrt{4Dt}\int_0^\infty (1 - erf\zeta)d\zeta \,. \qquad [4.18]$$

The integral in Equation 4.18 is simply $(\pi)^{-1/2}$. Therefore,

$$M = (C_O - C_B)\sqrt{4Dt/\pi} \qquad [4.19]$$

Equating this expression to the total amount of gas initially in the feature (hP_O/RT), and utilizing Henry's Law yields the wetting time, t_d:

$$t_d = \left(\frac{\pi}{D}\right)\left(\frac{k_H P_O hw}{8RT\gamma\cos\theta}\right)^2 \qquad [4.20]$$

where, again, D is the diffusivity of the gas in the liquid, h is the height of the feature, P_O is the initial pressure of the gas in the feature, k_H is henry's constant for the gas in the liquid, w is the width of the feature, R is the ideal gas constant, T is the temperature, γ is the surface tension of the liquid, and θ is the contact angle of the liquid on the solid.

4.5 Discussion

Equation 4.20 defines a simple relationship between wetting time and the variables that define the system for diffusion limited processes. This correlation can be used as a process design tool to investigate limitations in the use of liquids or fluids in the processing of devices with nano-scale feature sizes. In particular, the effects of contact angle, surface tension, and feature size on wetting time (and thus processes such as surface cleaning) can be explored.

The International Technology Roadmap for Semiconductors (SIA, 2001) predicts the dimensions of integrated circuit features in future years. Wetting times for these

features as calculated by Equation 4.20 are plotted in Figure 4.7, where the specific parameters used in this calculation are $T = 300$ K, $P_0 = 1$ bar, $k_H = 1.5\text{x}10^5$ Pa-m^3/mol, $D = 1\text{x}10^{-9}$ m^2/s, and $\gamma = 20$ mN/m, and the geometries of these features are listed in Table 4.2. Note that when the contact angle approaches 90° (the interfacial tension difference approaches zero) the wetting time increases exponentially. Under these conditions, wetting must be taken into account in process design and development.

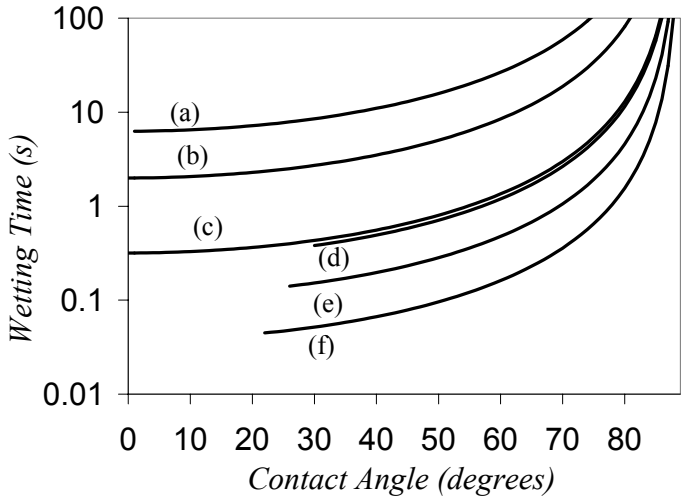

Figure 4.7. Wetting times of IC features specified in the ITRS, where (a)-(c) are DRAM trench capacitors and (d)-(f) are global interconnects to be produced in 2002, 2005, and 2008, respectively.

Table 4.2. Feature geometries of DRAM trench capacitors (DTC) and global interconnects (GI) at particular years of production.

Feature	Width (nm)	Height (nm)
GI 2002	382	649
GI 2005	280	560
GI 2008	195	468
DTC 2002	156	7500
DTC 2005	96	6900
DTC 2008	54	4900

The feature width-height product may be used as a primary factor to determine the importance of wetting as a function of feature size. The width corresponds to the rate at which gas is transported, while the height corresponds to the amount of gas that must be transported. Hence, the product of the width and height corresponds to the total time for transport.

Interfacial tension is an important fluid property, particularly for solutions that are engineered by the addition of surfactants. However, this property generally does not influence surface reactions or transport properties. Interfacial tension only affects wetting and dewetting. This model indicates that a simple reduction in surface tension is insufficient to improve wetting: instead, surfactant concentration should be selected to yield the maximum $\gamma\cos\theta$ product for minimal wetting time. Recall, however, that

$$\cos\theta = \frac{\gamma_{SG} - \gamma_{SL}}{\gamma} \qquad [4.21]$$

so the product is simply the difference of the solid-liquid and solid-gas interfacial tensions, independent of the gas-liquid interfacial tension. Therefore, although γ is

commonly measured when formulating process liquids, it is only the surfactant effect on the solid-liquid interfacial tension that influences wetting time.

4.6 Feature Collapse

An important result of the analysis of wetting/drying in liquid-phase processing is the quantification of the pressure that may be generated inside nanoscale features due to the interfacial pressure drop. This pressure, if sufficiently high, is capable of collapsing the feature. When neighboring features are under different pressures, collapse will occur if the resulting net force is above a critical value.

Namatsu, (1995), *et al*, have modeled this effect and have defined a criterion for which collapse will occur:

$$\sigma = \frac{6\gamma \cos\theta_C}{w}\left(\frac{H}{L_W}\right)^2 \qquad [4.22]$$

in which σ is the resulting tensile stress, and L_W is the linewidth. Each material, however, has a unique critical tensile stress, above which pattern deformation occurs.

Feature collapse becomes more of an issue as features sizes are reduced. Both Namatsu (1995) and Cao (2000), *et al.*, have reported experimental results indicating conditions under which feature collapse occurs. Cao's results as fit to the above model for PHOST-based photoresist features are plotted in Figure 4.8.

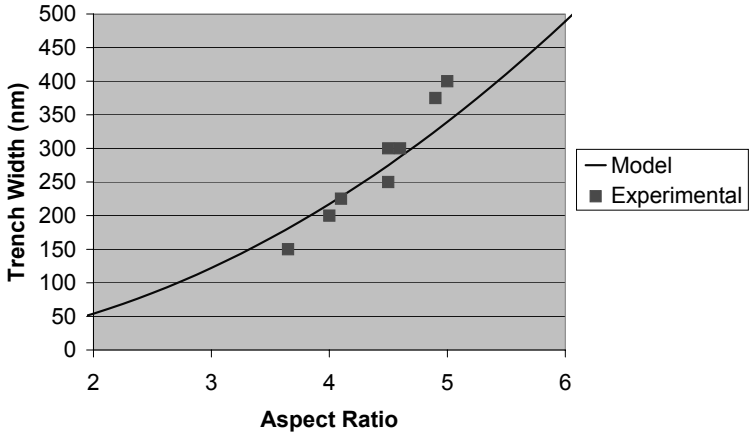

Figure 4.8. Feature collapse of PHOST as a function of aspect ratio with aqueous processing.

Clearly from these results if the allowable feature size for which lines are fabricated is to be reduced, fluids with reduced interfacial tensions must be used. One solution that has been proposed by numerous authors (Goldfarb, 2000)(Namatsu, 2000)(Namatsu, 1999)(Namatsu, 2001) is the use of supercritical fluid rinsing. Studies such as these have demonstrated that by rinsing with supercritical CO_2 feature collapse can be avoided. While supercritical fluids characteristically have no surface tension, the relatively high pressures that are required to operate under these conditions can be a great disadvantage. Additionally, the poor solvent ability of $scCO_2$ for many materials will limit its use. GXLs may be a superior alternative. Figure 4.9 illustrates the effects of using alternate fluids for processing of high-aspect ratio features without pattern collapse. This plot accounts for only the effect of surface tension and does not consider contact angle. GXLs can broaden the range of feature sizes that may be fabricated while the disadvantages associated with supercritical fluids are avoided.

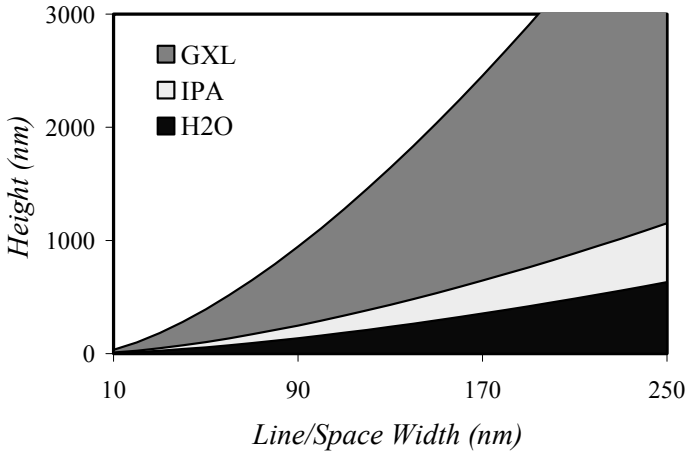

Figure 4.9. Plot of feature collapse as a function of feature geometry and process fluids. The height on the ordinate is the maximum height of PHOST-based photoresist lines that can be processed without collapse. This comparison is based on a contact angle of 50° and a PHOST critical stress of 5.5 MPa.

However, the product of $\gamma \cos\theta$ is equivalent to the difference of the solid-liquid and solid-vapor interfacial tension. This quantity is more difficult to estimate than surface tension alone. The impact upon feature collapse can be further understood if high pressure contact angle studies are performed, analogous to those in the petroleum industry (McCaffery, 1972) using high pressure optical cells.

4.7 Dielectric Compatibility

The previous analysis of wetting suggests that to design a process for which wetting is not significantly inhibited, the difference between the solid-liquid and solid-vapor interfacial tension should be maximized. However, an additional requirement of processing dielectrics is to maintain the geometry and physical properties of the dielectric. SiO_2 is mechanically and chemically stable, but novel dielectric materials of

very different nature may be more sensitive to chemical treatment. Therefore, an additional requirement for a chemical process is that it must leave the properties and geometry of the dielectric unchanged.

Unfortunately, these two requirements are closely related. A liquid will wet a solid if the molecular attractive forces are stronger than those of the gas and solid. Similarly, a liquid may solvate a solid if molecular attractive forces are great. Therefore, wetting liquids tend to solvate a solid. Solvation is a primary cause of dielectric damage. A liquid that does not attack the solid will likely have weak attractive forces or repulsive forces, but this will lead to incomplete wetting. For instance, one study of this issure correlated contact angle with solubility of a polymer (Qin, 1996). With few exceptions, solvents that completely wet a polymer will either dissolve or swell the polymer as well. Solvents that do not attack a polymer exhibit a large contact angle (>50°).

This information is useful for designing novel cleaning processes. There must be a balance between compatibility of a solvent with the solid and wettability. Solvents that have absolutely no impact on the properties of a polymer will likely not wet.

4.8 Conclusion

A model has been developed to investigate how processing variables directly correlate to the wetting time contribution of liquid-phase processes such as cleaning. The direct relationship between wetting time and surface tension, contact angle, fluid density, viscosity, temperature, pressure, flow rate, flow profile, diffusivity, and solubility allows optimal process design with respect to wetting. This numerical model is used to identify specific conditions under which wetting time may be significant, and therefore must be

considered in the design of a process. In particular, wetting time may be important for features with a large height-width product, for processes in which the contact angle approaches 90°, and for processes in which total processing time must be small for adequate throughput.

An analytical model has also been derived for conditions in which wetting is diffusion controlled. From this model, a simple expression for wetting time is derived (Equation 4.20) and the effects of feature geometry and contact angle are developed. This analysis predicts how wetting will scale in future device generations. Wetting times are reduced as the diameter and height of features are reduced, suggesting that it will not be increasingly difficult to wet nano-scale features found in integrated circuits with traditional liquids. However, when the gas-solid interfacial tension is greater than or on the order of the liquid-solid interfacial tension (i.e. the contact angle approaches 90°), the wetting time is significant. This may be particularly applicable when using aqueous liquids with hydrophobic films or polymer residues.

Although weakly wetting liquids can impact total process time and uniformity, strongly wetting liquids will also impact yield. More sensitive film patterns such as high aspect ratio photoresist lines can collapse due to capillary forces. Wetting liquids also may affect the physical properties of a material, particularly the geometry and dielectric constant of a patterned polymer film. Design equations such as those derived in this chapter can provide useful insight for the design of improved, optimized chemical processes for future generations of integrated circuits and other state-of-the-art microdevices.

Gas expansion is one potential method for tuning surface tension and wettability of liquids. The reduced surface tension of these liquids can be particularly useful when wetting, feature collapse, or compatibility is challenged with conventional liquids.

CHAPTER 5

TRANSPORT PROPERTIES

5.1 Introduction

Limitations may exist in the use of liquids to process nanoscale features as needed in the fabrication of ICs. For instance, viscosity, surface tension, and diffusivity of liquids may inhibit mass transport and surface wetting of these features. Therefore, carbon dioxide has been suggested as an alternative to traditional liquids for surface cleaning and photoresist development (SIA, 2001). The physical properties of liquid carbon dioxide include a significantly lower viscosity and surface tension, and a greater diffusivity than conventional liquid counterparts, which suggest the possibility of improving mass transport and wettability. In addition, it is relatively benign in terms of flammability, toxicity, and environmental impact. However, carbon dioxide is often a poor solvent in the liquid phase and is even less effective in the supercritical phase. Some solubility of materials such as silicones and fluorocarbons is possible, but other materials, especially those with polar moieties, are essentially insoluble.

Due to their unique range of properties, gas-expanded liquids (GXLs) may overcome the limitations of traditional solvents, pure CO_2, and supercritical mixtures of these components. The physical properties of GXLs range between those of the pure components, suggesting that both excellent mass transport and excellent solvent strength are possible. For example, the solvent strength of GXLs is much greater than that of gases or supercritical fluids, while the surface tension and viscosity of GXLs is much lower than that of liquids. As a result, GXLs may be tuned for both optimal performance

and minimal environmental impact. In order to evaluate GXLs and other alternatives to traditional liquid-phase processes, the impact of physical property modification on processes such as dissolution and transport within nanoscale features must be understood. A simple, useful tool for this purpose is mass transport theory.

5.2 Transport within Nanoscale Features

Because little to no convection occurs within nanoscale features (Olim, 1997) (Takahashi and Gross, 1999), transport is limited by diffusion. The rate of diffusional transport is a function of both the diffusivity and solubility of the solute in the liquid.

Transport from the bottom of a high-aspect ratio feature is characterized by (Cussler, 1997)

$$\frac{dC}{dt} = D\frac{d^2C}{dz^2} \qquad [5.1]$$

where z is the distance from the feature bottom, C is the concentration of the solute, and D is the diffusivity of the solute in the solvent. Using the boundary conditions that $C(z = 0, t) = C_S$, $C(z, t = 0) = 0$, and $C(z \to \infty, t) = 0$, solution of Equation 5.1 yields

$$C(t,z) = C_S\left(erfc\left(\frac{z}{\sqrt{4Dt}}\right)\right) \qquad [5.2]$$

The total amount of dissolved species, S, as a function of time is found by integrating Equation 5.2 from $z = 0$ to ∞, yielding

$$S = C_S\sqrt{\frac{4Dt}{\pi}} \qquad [5.3]$$

Therefore, the time necessary for transport to occur in one liquid (1) relative to that in another liquid (2) with different properties is

$$\frac{t_1}{t_2} = \frac{C_2^2}{C_1^2}\frac{D_2}{D_1} \qquad [5.4]$$

Equation 5.4 is a simple relationship between transport within nanoscale features and the properties of the liquid. In this case, solubility, C, and diffusivity, D, are the properties of interest. These are measurable quantities and can be determined either through experiments, available data, or correlations.

5.3 Dissolution Rate Enhancement

Dissolution is, in general, a complex multistep mechanism. However, if one particular step occurs at a significantly lower rate than other steps, the overall dissolution rate will be equivalent to the rate of the limiting step. One such rate-limiting step is the transport of a solute into a bulk liquid. This is a common rate-limiting step generally applicable to sparingly soluble solutes. In fact, this has been shown to be one of the rate-limiting steps in the dissolution of novolak-based photoresist (Hunek and Cussler, 2002).

At steady state, the dissolution rate can be approximated using correlations for the mass transfer coefficient. The mass-transfer-limited dissolution rate, DR, from a spinning disk is given by (Cussler, 1997)

$$DR = 0.62 C_S D^{2/3} \varpi^{1/2} \rho^{1/6} \mu^{-1/6} \qquad [5.5]$$

where C_S is the solubility of the solute in the liquid, ω is the rotation rate, ρ is the density of the liquid, and μ is the liquid viscosity. A spinning disk is of particular interest because the transport rate is uniform across the radius of the disk.

Equation 5.5 allows the mass-transfer-limited dissolution rate that results from the use of two different fluids to be compared.

$$\frac{DR_1}{DR_2} = \frac{C_1}{C_2}\left(\frac{D_1}{D_2}\right)^{2/3}\left(\frac{\omega_1}{\omega_2}\right)^{1/2}\left(\frac{\rho_1}{\rho_2}\right)^{1/6}\left(\frac{\mu_2}{\mu_1}\right)^{1/6} \qquad [5.6]$$

In this equation C, D, μ and ρ are all measurable quantities and can be determined either through experiments, available data, or correlations.

One may be interested in comparing dissolution rates at a particular rotation rate. In this case, the ratio of ω in Equation 5.6 is unity. However, because the rotation rate is coupled to the volumetric flow rate of liquid dispensed on a rotating disk, this comparison would not account for differences in the flow rates that would need to be delivered to the disk at a particular rotation rate. An alternative basis for comparison of dissolution rates is flow rate.

The volumetric flow rate dispensed at the center of the disk is given by (Middleman, *Fluids*, 1998)

$$Q = \frac{2}{3}\pi\frac{\rho}{\mu}r^2\varpi^2h^3 \qquad [5.7]$$

where r is the radius and h is the height of the liquid at r. In principle, the height should be a factor greater than the boundary layer thickness (otherwise, the flow profile will be perturbed and uniform dissolution will not occur). This boundary layer thickness, h_P, is given by (Levich, 1962)

$$h_P = \frac{3.6\mu^{1/2}}{\varpi^{1/2}\rho^{1/2}} \qquad [5.8]$$

Combination of Equation 5.7 with Equation 5.8 yields the ratio of rotation rates as

$$\left(\frac{\varpi_1}{\varpi_2}\right)^{1/2} = \frac{Q_1}{Q_2}\left(\frac{\mu_2}{\mu_1}\right)^{1/2}\left(\frac{\rho_1}{\rho_2}\right)^{1/2} \qquad [5.9]$$

and substitution into Equation 5.6 yields

$$\frac{DR_1}{DR_2} = \frac{C_1}{C_2}\frac{Q_1}{Q_2}\left(\frac{D_1}{D_2}\right)^{2/3}\left(\frac{\rho_1}{\rho_2}\right)^{2/3}\left(\frac{\mu_1}{\mu_2}\right)^{-2/3} \qquad [5.10]$$

Using Equation 5.10, the dissolution rates in two liquids can be compared with account of the volumetric flow rate dispensed.

5.4 Optimizing Properties with Gas-Expanded Liquids

In Chapter 3, gas-expanded liquids were defined and methods for estimating their physical properties were described. The composition of the liquid can be varied from that of essentially pure solvent to that of essentially pure liquid carbon dioxide. Similarly, the physical properties (viscosity, diffusivity, density, etc.) can be modified over the range of the pure component properties and hence the properties of the liquid phase (e.g., for solubilization of residues, removal of photoresist, penetration of shallow trenches) are tunable (West, 2001). To the authors' knowledge, no studies have been reported where applications of GXLs in microelectronics processing have been investigated.

While the physical properties of GXLs may lead to improvements in mass transport, the solvent strength of the pure liquid is sacrificed. However, preliminary experiments with GXLs have indicated that the solvent properties of the pure liquid are largely maintained upon expansion (Chapter 8). When improvements in transport properties favor a greater transport rate than the corresponding effect of a decrease in solubility, the use of GXLs are expected to be superior to traditional liquids. The equations derived above for dissolution (Equations 5.6 and 5.10) and for transport within

nanoscale features (Equation 5.4) are used to predict opportunities for GXLs in the following discussion.

The solubility and diffusivity of a GXL are estimated using correlations described in Section 3.2. Using these estimates, the transport time in Equation 5.4 is plotted versus solvent mole fraction in Figure 5.1. For a GXL in which the solvent mole fraction is 77%, the time is decreased by 8%. This analysis also indicates that a GXL containing as much as 43% CO_2 may be used without extending the transport time. Using the simple transport theory described here, it is predicted that small improvements in transport within nanoscale features are possible in using GXLs containing up to ~40% CO_2. It is in this composition range that the increase in diffusivity dominates the decrease in solubility of a GXL relative to a traditional liquid.

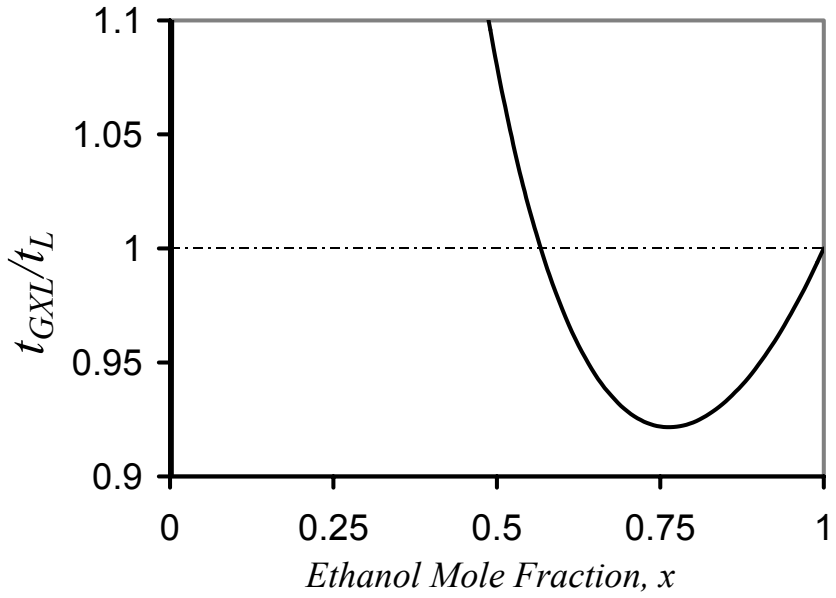

Figure 5.1. Ratio of the time to transport species within a nanoscale feature using a GXL to that using a traditional liquid. A GXL with as much as 46% CO_2 will not increase the time necessary for removal compared to a liquid.

Substitution of the correlations described in the Section 3.2 into Equation 5.6 yields an expression for the relative dissolution rates as a function of solvent fraction at a particular rotation rate. This result is plotted in Figure 5.2, which indicates that the dissolution rate is enhanced for all GXLs with a solvent fraction greater than ~15% due to improved transport into the GXL. Furthermore, the dissolution rate can be enhanced by over 1.5 times that of the pure solvent. The dissolution rate is enhanced due to an increase in diffusivity and decrease in viscosity of the GXL relative to the traditional liquid, which has a greater impact on the net dissolution rate than the decrease in solubility.

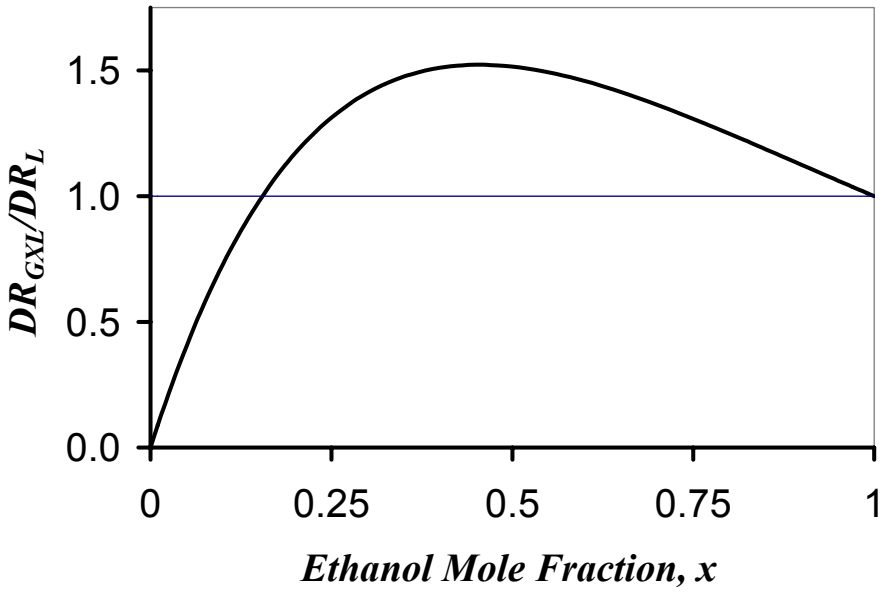

Figure 5.2. Ratio of the dissolution rate in a GXL to the dissolution rate in a traditional liquid at a particular rotation rate. Dissolution rate enhancement occurs for all GXLs with a solvent fraction greater than ~15%.

The volumetric flowrate of a GXL containing an equivalent amount of solvent to that of a pure liquid is given by

$$Q_{GXL} = Q_L \frac{\rho_L M_{GXL}}{x\rho_{GXL} M_L} \qquad [5.11]$$

where M is the molecular weight and x is the solvent fraction in the GXL. Substituting Equation 5.11 into Equation 5.10 yields

$$\frac{DR_{GXL}}{DR_L} = \frac{1}{x}\frac{C_{GXL}}{C_L}\left(\frac{D_{GXL}}{D_L}\right)^{2/3}\left(\frac{\rho_{GXL}}{\rho_L}\right)^{-1/3}\left(\frac{\mu_{GXL}}{\mu_L}\right)^{-2/3}\left(\frac{M_{GXL}}{M_L}\right) \qquad [5.12]$$

Substitution of the appropriate physical property ratios into Equation 5.12 yields an expression for the relative dissolution rates as a function of solvent fraction. This function is plotted in Figure 5.3. Comparing the dissolution rate in a GXL to that of a liquid in this way suggests that dissolution is enhanced as a result of gas expansion. Again, the dissolution rate is enhanced due to an increase in diffusivity and decrease in viscosity of the GXL relative to the traditional liquid, which has a greater impact on the net dissolution rate than does the decrease in solubility.

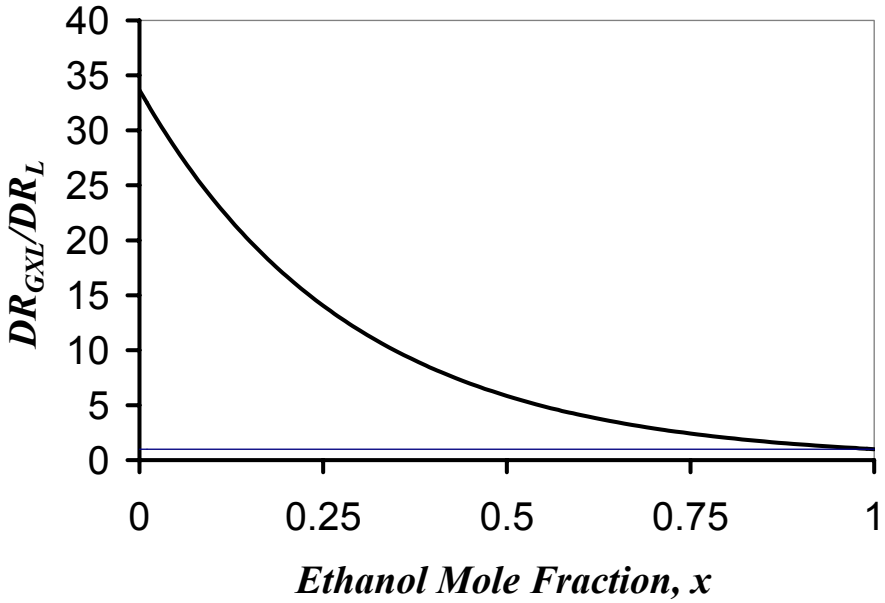

Figure 5.3. Ratio of the dissolution rate in a GXL to the dissolution rate in a traditional liquid when dispensing an equivalent amount of solvent. Significant dissolution rate enhancement occurs.

Similarly, comparing a GXL to a traditional liquid on the basis of equivalent dissolution rates estimates the amount of solvent that must be consumed.

$$\frac{n_{GXL}}{n_L} = x\left(\frac{C_{GXL}}{C_L}\right)^{-1}\left(\frac{D_{GXL}}{D_L}\right)^{-2/3}\left(\frac{\rho_{GXL}}{\rho_L}\right)^{1/3}\left(\frac{\mu_{GXL}}{\mu_L}\right)^{2/3}\left(\frac{M_{GXL}}{M_L}\right)^{-1} \qquad [5.13]$$

where n is the moles of solvent. This ratio is plotted in Figure 5.4 and suggests that the use of GXLs can lead to a significant reduction of solvent consumption.

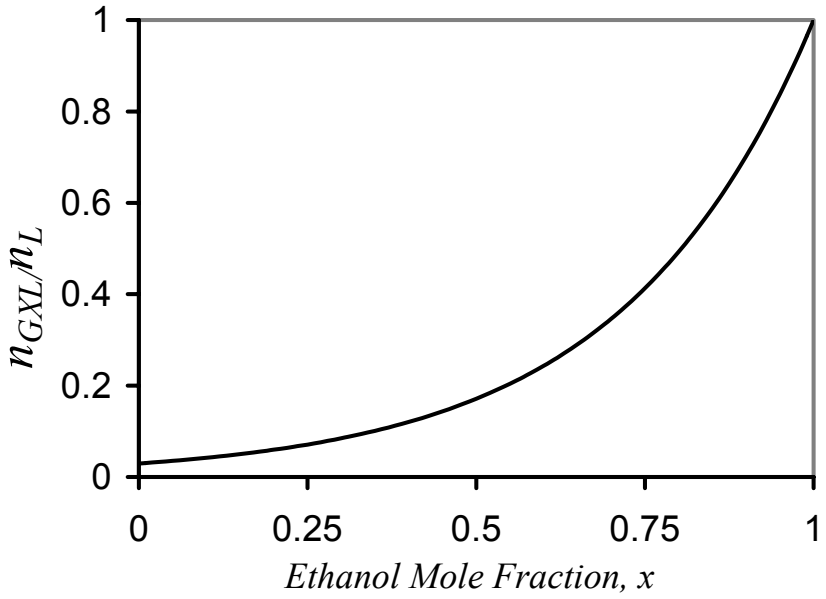

Figure 5.4. Ratio of moles of solvent consumed, n, in a GXL to that in a traditional liquid for equivalent dissolution rates. The amount of solvent that must be consumed is significantly less in a GXL than in a traditional liquid.

5.5 Discussion

The use of mass transport theory provides an estimate of how the modification of liquid properties can yield increased transport rates. Although this work has focused upon GXLs, the theory described can be extended to other systems such as supercritical

fluids. However, these estimates are only valid for processes that are limited by mass transport. Post-etch resist and residue removal may be limited by other mechanisms such as polymer chain disentanglement, surface reactions, and wetting. Some of these mechanistic steps are independent of liquid properties. For instance, surface reactions will generally depend on the concentration of reactants, and will not depend on transport properties such as viscosity. The effects of physical property modification on mechanistic steps such as polymer disentanglement may be important, but are difficult to predict quantitatively. The impact of the use of GXLs relative to that of liquids for film/residue removal controlled by one or more of the above mechanisms is not addressed in this chapter.

It should also be noted that the estimates of physical properties of GXLs were derived above for ideal mixtures. Nonideal mixtures can lead to significantly different physical properties than those estimated in this study. For example, solubility enhancement has been observed in some liquid mixtures (Prausnitz et al., 1999) and would impact estimates of dissolution and transport within nanoscale features. More accurate physical property values, such as those determined experimentally, can also be used in the previously described models for comparing different liquids such as GXLs.

5.6 Conclusion

In this chapter, transport within nanoscale features and the dissolution rate from a rotating substrate are quantified as functions of physical properties of a liquid using mass transport theory. These transport models are used to estimate the possible advantages of

gas-expanded liquids (GXLs), which combine improved physical properties over traditional liquids with the environmental advantages associated with CO_2-based fluids.

This analysis suggests that transport within nanoscale features is aided due to the increased diffusivity in GXLs. Therefore, GXLs may be a useful alternative to traditional liquids in microelectronic processes that are limited by transport within nanoscale features.

The improved transport properties of GXLs relative to traditional liquids also lead to increased dissolution rates when compared on the basis of both rotation rate and solvent consumption. In addition, less solvent must be consumed when using a GXL relative to a traditional liquid for equivalent flow rates. Therefore, tremendous environmental improvements may be realized without sacrificing performance in photoresist and residue removal processes.

CHAPTER 6

IN SITU MONITORING OF FILM REFRACTIVE INDEX AND THICKNESS

6.1 Introduction

Real-time optical monitors of film thickness are used in a wide range of applications. For example, film thickness changes are monitored routinely in such processes as photoresist development and endpoint detection during dielectric etching. Multiwavelength interferometry (MWI) is a cost-effective, optical technique used to determine film thickness based on known, constant values of the film refractive index (Henderson, 1998; Pham, 2002). However, many processes that lead to a thickness change also lead to a corresponding change in the optical properties. In these processes, inaccurate film thickness measurements are obtained if the dynamic optical properties are not considered. Such concerns can be overcome by the use of real-time spectroscopic ellipsometry (Sirard, 2000; Burns, 2003), but in closed systems, window birefringence has been reported to lead to significant measurement errors. Furthermore, ellipsometry systems are typically more costly than MWI.

Conventional MWI techniques calculate film thickness from the effective frequency of the interference spectrum. Extending the interference analysis to include the amplitude of the interference spectrum allows the film refractive index to be calculated, since the amplitude is independent of film thickness (Tompkins, 1999). Use of the interference amplitude has analogously been suggested for monitoring thin film growth directly on an optical fiber (Johnson, 2001). This chapter details the application of this technique.

6.2 Experimental Setup

The equipment components needed to assemble a reflectance monitor have been described previously (Agrawal and Henderson, 2003). The optical components are available from Ocean Optics (Dunedin, FL); these consist of a tungsten filament light source (LS-1), a fiber optic probe (R200) and spectrometer (USB2000). The optical fibers connecting the light source and spectrometer are coaxial in the probe, which is positioned with optical aligners (Newport). Ocean Optics software has been used to acquire interference spectra. The greatest intensity of this light source occurs from 500 to 750 nm; therefore, this wavelength range is used in the following analyses.

Figure 6.1 is a schematic diagram of the interferometer system. A ¾-inch stainless steel union cross (Swagelok) is used as the main chamber. Two ports of the cross are used as the inlet and outlet for a process liquid, gas or fluid. One port supports a thermocouple while the fourth is equipped with a sapphire window (Esco Products). A stainless steel sample holder has been machined to hold a thin film sample within the cross, parallel to the sapphire window.

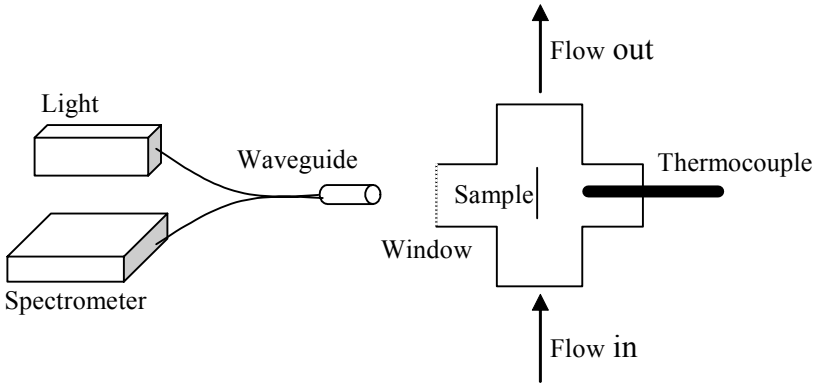

Figure 6.1. Schematic diagram of the dissolution rate monitor.

The system described in Chapter 3 is used to deliver process fluids at elevated pressures into the analysis cross. To enable precise control of the vapor composition to which a film sample is exposed, a custom vapor delivery system was designed and assembled. This system is pictured in Figure 6.2. Nitrogen serves as a purge gas, a solvent carrier gas, and a diluent. Flow rates are controlled by mass flow controllers, thus allowing the composition of the vapor phase delivered to the cross to be changed. The carrier stream flows through a liquid-gas contacting column, which is packed with glass Raschig rings to enhance mixing. The flow rate range and column design are designed to ensure that the carrier stream leaving the column is saturated with the vapor of interest. Using design equations for gas-liquid contactors (Perry, 1998), the height of a column necessary to approach 95% saturation of the carrier gas with solvent was determined. Given the fraction of ethanol in nitrogen at standard conditions is 0.07 (from Raoult's Law), the number of transfer units is 0.09. The height of a transfer unit is approximately 8 ft. Therefore, a contactor height of 8 inches is necessary to reach 95% saturation.

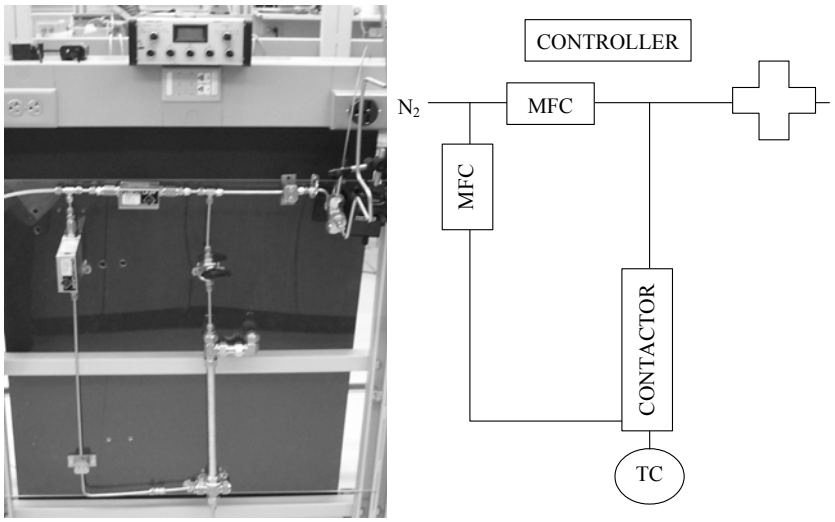

Figure 6.2. A gas-liquid contactor is used to modify the composition of ethanol vapor exposed to a thin film sample for film thickness measurements with MWI.

A schematic of the light path is shown in Figure 6.3. The source is aligned normal to the thin film sample, and the resulting reflectance is affected by each medium through which it passes. These include the ambient air (0), the sapphire window (1), the process fluid (2), the thin film (3), and the substrate (4). Reflection and transmission occur at each individual interface and the sum of each reflection is detected by the spectrometer.

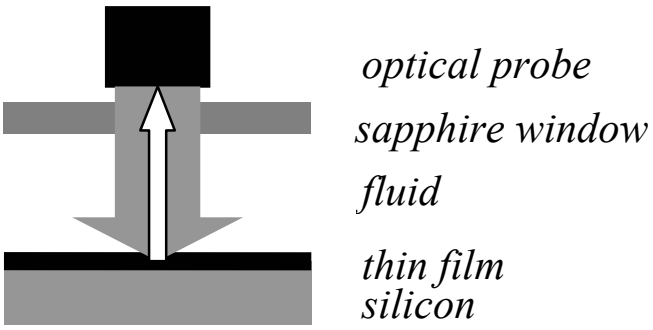

Figure 6.3. A schematic diagram of the path of normally incident transmitted and reflected light.

6.3 Reflectance Theory

The resulting reflectance from a multilayered structure such as that in Figure 6.3 has been mathematically defined (Heavens, 1991) in matrix form. The intensity is a function of the optical properties and thickness of each medium. These parameters are known for air, the sapphire window and the silicon substrate. Therefore, the optical properties of the fluid and of the film, as well as the film thickness can be calculated by fitting the measured reflectance to the function containing the unknown parameters of interest.

With this system, a few simplifications can be invoked. The light source used is incoherent; interference will therefore occur only when the thickness of the medium is less than the coherence length of the light (Rancourt, 1996). The coherence length, Δl, is given by

$$\Delta l = \frac{\lambda^2}{\Delta\lambda} \qquad [6.1]$$

where $\Delta\lambda$ is the resolution of the spectrometer. The resolution of the spectrometer is 1.3 nm, and at a wavelength 589 nm, the coherence length is 0.27 mm. Therefore, only interference from the thin film is detected; sinusoidal interference terms within the model can be neglected.

A fitting parameter is added to each translation of the light through the window and through the fluid, respectively Λ_W and Λ_F. It is well known that penumbral loss of intensity occurs as incoherent light propagates through a medium. Loss also occurs due to scattering from nonplanarities at interfaces. The fitting parameters are physically related to these phenomena.

A three parameter Cauchy model is used to describe the dependence of optical properties on wavelength for materials with known optical parameters. From calculations of the optical properties of unknown films and fluids, a two parameter Cauchy model was found to be adequate for these analyses, since only marginal improvement of fitting the refractive index dispersion was achieved in adding a third Cauchy term. All materials but silicon are nonabsorbing in the wavelength range of interest.

The resulting characteristic equations for this system are:

$$\text{For } i = 1, 2, 3; \quad r_i = \frac{n_{i-1} - n_i}{n_{i-1} + n_i} \tag{6.2}$$

$$r_4 = \frac{n_3^2 - n_4^2 - k_4^2}{(n_3 + n_4)^2 + k_4^2} \tag{6.3}$$

$$h_4 = \frac{2n_3 k_4}{(n_3 + n_4)^2 + k_4^2} \tag{6.4}$$

$$\delta_3 = \frac{2\pi}{\lambda} d_3 n_3 \tag{6.5}$$

$$\rho_3^2 = \frac{r_3^2 + r_4^2 + h_4^2 + 2r_3 r_4 \cos(2\delta_3) + 2r_3 h_4 \sin(2\delta_3)}{1 + r_3^2 (r_4^2 + h_4^2) + 2r_3 r_4 \cos(2\delta_3) + 2r_3 h_4 \sin(2\delta_3)} \tag{6.6}$$

$$\rho_2^2 = \frac{r_2^2 + \Lambda_F \rho_3^2}{1 + \Lambda_F r_2^2 \rho_3^2} \tag{6.7}$$

$$\rho_1^2 = \frac{r_1^2 + \Lambda_W \rho_2^2}{1 + \Lambda_W r_1^2 \rho_2^2} \tag{6.8}$$

where n_i is the refractive index of medium i, k_4 is the extinction coefficient of the silicon substrate, r_i and h_4 are the real and imaginary Fresnel reflection coefficients, respectively, for interface i, δ_3 is the optical path length in the film, λ is the wavelength, and ρ_i is the amplitude of the net reflectance from interface i.

The intensity of the reflectance detected by the interferometer referenced to a background spectrum is $\rho_I^2/\rho_I^2(b)$, in which the background spectrum is described by

$$\rho_1^2(b) = \frac{r_1^2 + \Lambda_W r_2^2}{1 + \Lambda_W r_1^2 r_2^2}. \qquad [6.9]$$

For our experiments, the unknown parameters of interest can be calculated using software such as MS Excel solver to fit reflectance data to these models.

6.4 Refractive Indices of Gases and Liquids

For film monitoring in fluids other than air, the optical properties of the fluid must be known. Using the model described above for films, the optical properties of fluids can be independently measured. In this case, only reflectance from the air-window and window-fluid interfaces is needed. For these measurements, the sample holder is removed and the chamber filled with the fluid of interest. Of particular interest is the ability to measure high pressure fluids such as supercritical fluids, liquid carbon dioxide (L-CO_2) and mixtures of gases with liquids, such as GXLs.

The average reflectance of several spectra obtained when the chamber is filled with de-ionized water (DIW) was used to calculate the loss term of the window, Λ_W, but it was found to be equal to 1, and thus negligible. From measurements of $\rho_I^2/\rho_I^2(b)$ vs. λ, the refractive index of the fluid as a function of λ can be determined. Results of the use of this technique to measure refractive indices of common solvents are shown in Table 6.1. Reported values for these liquids are also tabulated.

Table 6.1. Measured and reported (DIPPR, 2002) refractive indices (at 589 nm).

Solvent	Measured RI	95% Conf. Int.	Reported RI
Methanol	1.335	± 0.004	1.327
Ethanol	1.361	± 0.007	1.359
NMP	1.445	± 0.004	1.469
L-CO_2	1.174	± 0.042	1.180

This technique can also be used to measure optical properties of high pressure fluids. Table 6.1 contains the refractive index measurement of liquid CO_2, and Figure 6.4 plots the refractive index of CO_2 as a function of pressure. Also, the refractive index of a mixture can be calculated from pure component properties using the Lorentz-Lorenz mixing rule. This is given by:

$$\frac{n_{mix}^2 - 1}{n_{mix}^2 + 2} = \sum \frac{\rho_i R_i}{MW_i} \qquad [6.10]$$

where R_i is the molar reflectance, MW_i is the molecular weight, and ρ_i is the density, all of component i, and n_{mix} is the refractive index of the GXL. An example of this measurement is shown in Table 6.2. Unfortunately, complementary techniques for comparatively measuring the refractive index of these high pressure liquids are not available.

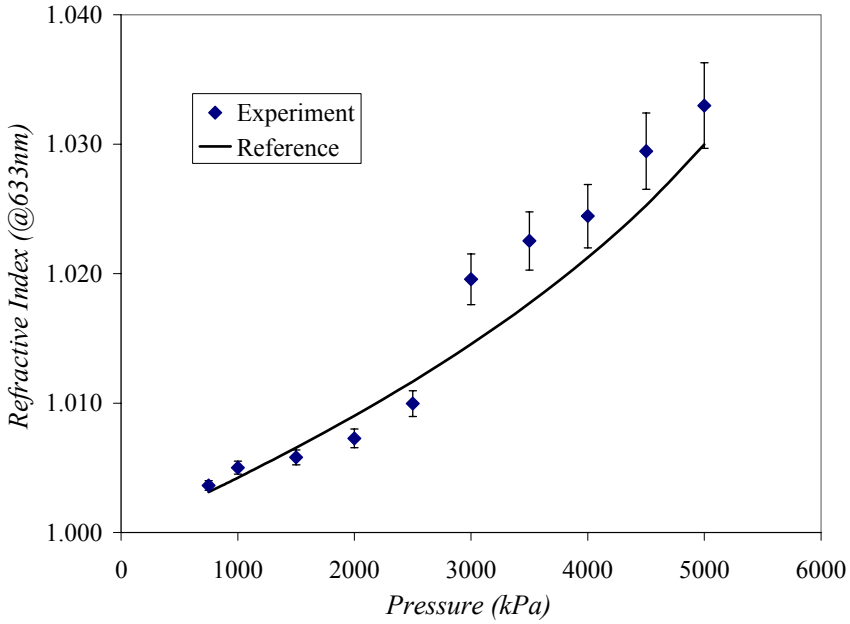

Figure 6.4. Refractive index of CO_2 vs pressure.

Table 6.2. Refractive index of CO_2-expanded ethanol, experimental and predicted results.

Pressure	Temperature	Density	CO_2 fraction	RI @ 589nm	Predicted RI
5000 kPa	22.8 °C	839.1 kg/m^3	0.76 mol	1.234	1.240

6.5 Refractive Index and Thickness of Thin Films

The measurement of film thickness and optical properties using this approach has been compared to results obtained using spectroscopic ellipsometry (V-VASE®, J.A. Woollam Co., Inc.). For this measurement, a polyhydroxystyrene (PHOST) film was spincast from a solution of 20wt% PHOST (MW=10,700, PDI=1.58) in PGMEA and subsequently baked on a hotplate at 120ºC for 5 minutes. Additional experiments were also performed with a commercially prepared JSR photoresist film (PFRIX4204) that had

been baked at 120ºC for 1 minute. The PHOST film is useful for fundamental studies in that the composition of the film is well known. The JSR resist, however, is more characteristic of those used in commercial processes. Resulting measurements of these films are shown in Table 6.3 and 6.4. Raw interferometry data and the model fit to this data is represented in Figure 6.5. The two techniques yield comparable results.

Table 6.3. Comparison of PHOST film thickness and RI determined by ellipsometry and by the current approach.

Measurement	Thickness (μm)	Conf. Int 95%	RI @589nm	Conf. Int 95%
Ellipsometer	2.415	0.020	1.639	0.021
Interferometer	2.410	0.180	1.619	0.131

Table 6.4. Comparison of JSR resist thickness and RI determined by ellipsometry and by the current approach.

Measurement	Thickness (μm)	Conf. Int 95%	RI @589nm	Conf. Int 95%
Ellipsometer	1.413	0.005	1.644	0.008
Interferometer	1.395	0.048	1.669	0.071

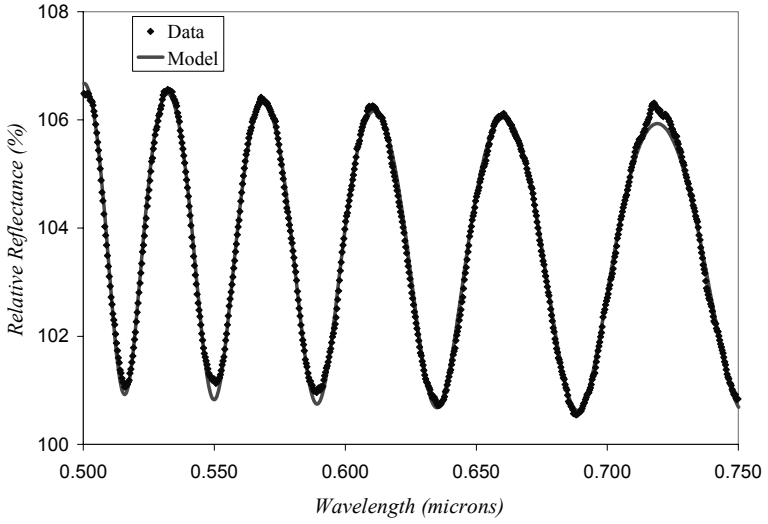

Figure 6.5. The reflectance model fit to reflectance data of a PHOST film.

This MWI approach is well suited to analyze thickness and refractive index changes of a polymer film *in situ*. First, a film is placed directly in a chamber having been previously filled with ethanol, exposing the film to concentrated ethanol vapor. The resulting measured values for thickness and refractive index as a function of exposure time are plotted in Figure 6.6. For comparison, the film thickness, calculated with a constant refractive index of the film, is also displayed. Obviously, the assumption of constant refractive index results in a large underestimate of the extent of polymer swelling in this case.

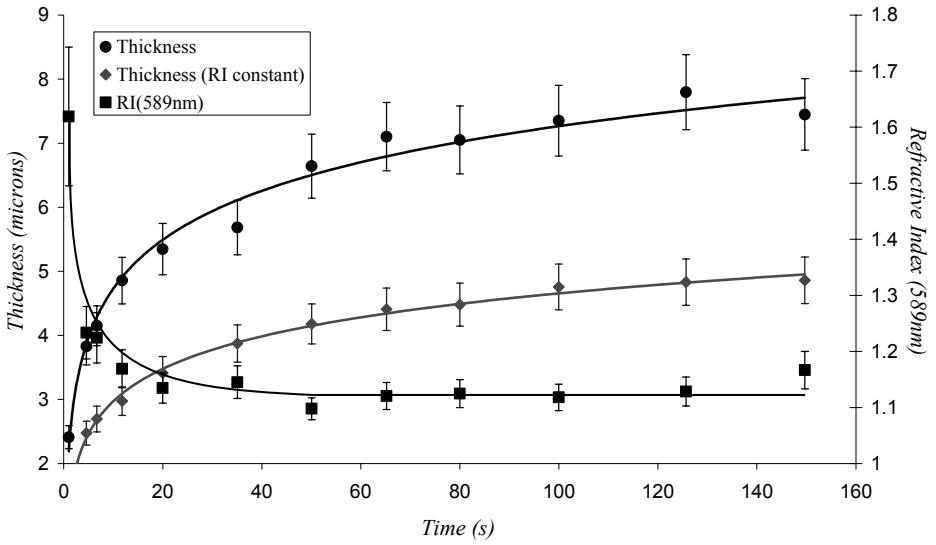

Figure 6.6. Refractive index and thickness change of PHOST films exposed to ethanol vapor.

PHOST was also exposed to dilute ethanol vapor. This was performed in the vapor cell previously described; the results are plotted in Figure 6.7. The thickness and refractive index of the film before and after exposure is shown in Table 6.5, as is the ellipsometry measurement of the original film.

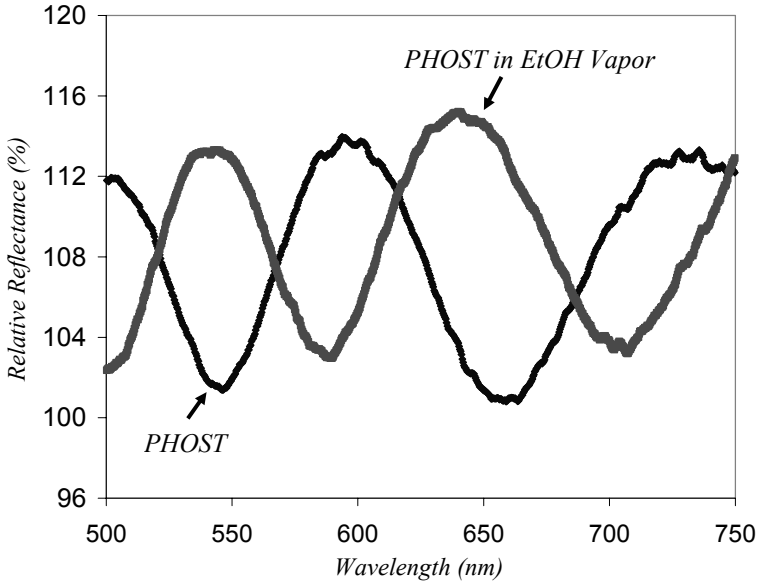

Figure 6.7. Relative reflectance from a PHOST film before and after exposure to dilute ethanol vapor.

Table 6.5. Comparison of PHOST film thickness and RI determined by ellipsometry, by interferometry, and following exposure to dilute ethanol vapor.

Measurement	Treatment	RI @589nm	Thickness (μm)
Ellipsometer	None	1.673 ± .005	1.053 ± .001
Interferometer	None	1.697	1.053
Interferometer	Dilute EtOH Vapor	1.478	1.091

MWI was also applied to the dissolution of a photoresist film in a liquid. Figure 6.7 shows the results of the JSR resist dissolution in 0.13 N tetramethylammonium hydroxide (TMAH) in water. In this case, little variation of the film refractive index occurs; thus, the resulting thickness does not vary significantly by assuming that the JSR refractive index remains constant upon TMAH solution exposure.

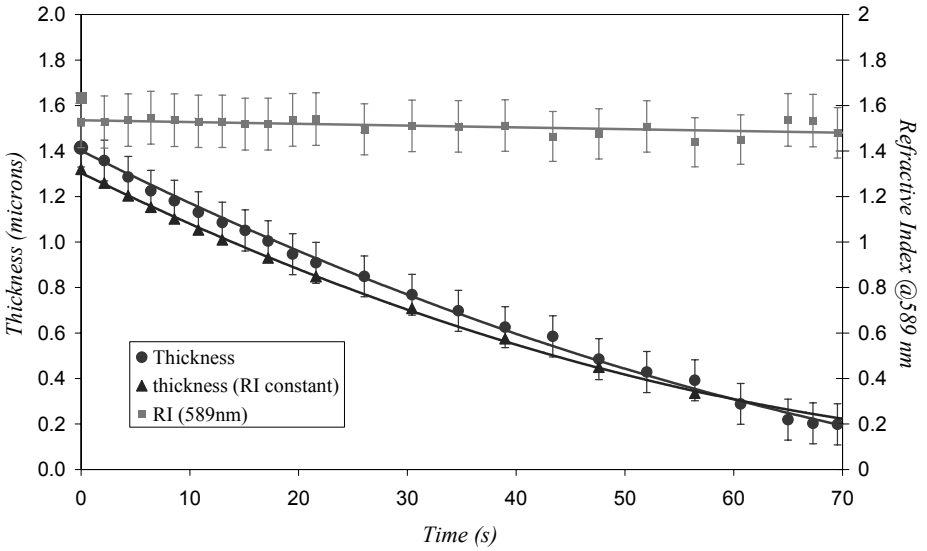

Figure 6.7. Refractive index and thickness change of a commercial JSR resist in a 0.13N TMAH aqueous solution.

Finally, the response of the JSR photoresist in CO_2 at pressures up to 5.0 MPa and at room temperature (22º C) was monitored; results are plotted in Figure 6.8. This measurement indicates the film is slightly compressed; the refractive index increases and the film thickness decreases.

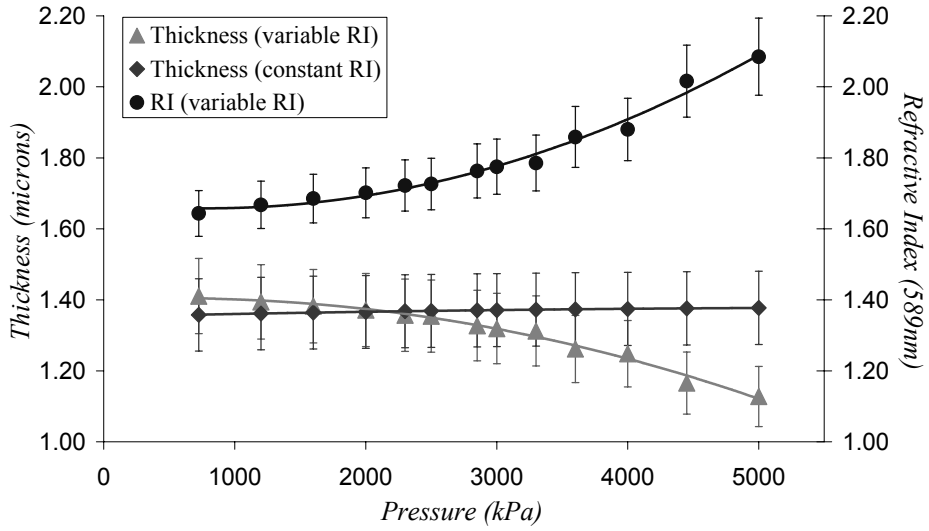

Figure 6.8. Compression of a commercial JSR photoresist in high pressure CO_2.

6.6 Discussion

MWI yields film thickness and refractive index results comparable to spectroscopic ellipsometry. Measurements of gas and liquid refractive indices are comparable to reported reference values. However, the confidence intervals of the values for thickness and refractive index reported are large relative to conventional optical techniques.

One source of error is the alignment of the interferometer probe. This measurement, as is usually the case in optical measurements, is sensitive to angular alignment. We have aligned the probe by maximizing the intensity of the reflectance. Even a small deviation from normal incidence results in almost entire loss of signal intensity. It is feasible that commercial development of this technique can allow more precise and accurate alignment and thus measurements.

Some fluctuation of the spectrometer signal with time has been observed; this is primarily attributed to the variation of the power output from the laboratory wall outlets. Using a multimeter to monitor changes in the voltage of both the AC wall outlet and the DC converter output, a variation of approximately 1% occurs in both cases, having a period of approximately 25 minutes. Since the intensity of the light source varies with the power supply, as does the sensitivity of the CCD within the spectrometer, this has been determined to be a primary factor in the observed variation. A regulated power supply has been added to this system to minimize this variability, and the software has been modified to correct for this variation be neglecting the signal from the first 23 elements of the detector. Prior to these modifications, the confidence intervals of film measurements were much greater.

Deviations from reported values of organic solvents may also correspond to moisture absorption, resulting in the observed lower refractive indices. Using Karl Fisher titration, the concentration of water in NMP, for example, was found to be 0.4%. However, using the mixing rule of Chapter 3 (Eq. 3.7), this would lead to a negligible refractive index change of only 0.001.

6.7 Conclusion

A real-time interferometric approach has been developed to monitor both film thickness and refractive index. Furthermore, these measurements can be performed using relatively inexpensive, commercially available system components. In addition, refractive indices of pure liquids and liquid mixtures can be measured, including elevated pressure fluids. Film thickness and refractive index measurements of polymer thin films are consistent with measurements obtained by spectroscopic ellipsometry. In addition, these film properties can be measured dynamically, particularly during dissolution and swelling.

CHAPTER 7

PHOTORESIST REMOVAL USING CO_2-EXPANDED LIQUIDS

7.1 Introduction

Photoresist removal is one of the most critical and most repeated cleaning processes in the fabrication of an integrated circuit (IC). A state-of-the-art IC consists of over 25 masking steps (ITRS, 2001), each utilizing a photoresist for pattern generation, and each requiring a subsequent photoresist removal process. Photoresist exposed to processes such as ion implantation and plasma reactive ion etching becomes a heavily carbonized, hardened polymeric residue that can be particularly difficult to remove.

Current commercial formulations have proven to be ineffective in fully removing these residues (Louis, 2001). These formulations primarily consist of conventional organic solvents, water, surfactants, and reactive components such as amines. Carbon dioxide has been suggested as an alternative to traditional liquids for surface cleaning and photoresist development (SIA, 2001). Carbon dioxide is relatively benign in terms of flammability, toxicity, and environmental impact. In addition, its physical properties include a significantly lower viscosity and surface tension, and a greater diffusivity than liquid counterparts, which suggest the possibility of improving mass transport and wettability. However, carbon dioxide is often a poor solvent in the liquid phase and is even less effective in the supercritical phase. Due to their unique range of properties, gas-expanded liquids (GXLs) may overcome the limitations of traditional solvents, pure CO_2, and supercritical mixtures of these components. The application of these GXLs has, therefore, been experimentally investigated.

7.2 Experimental Equipment Setup

Several systems have been assembled for use in evaluating the efficiency of GXLs for photoresist removal. The ability to process entire wafers is valuable in evaluating fluids such as GXLs under elevated temperatures and pressures. For these applications, a system has been designed and built for treatment of 8-inch diameter wafers. Diagrams of the complete system and the main pressure vessel are shown in Figures 7.1 and 7.2, respectively.

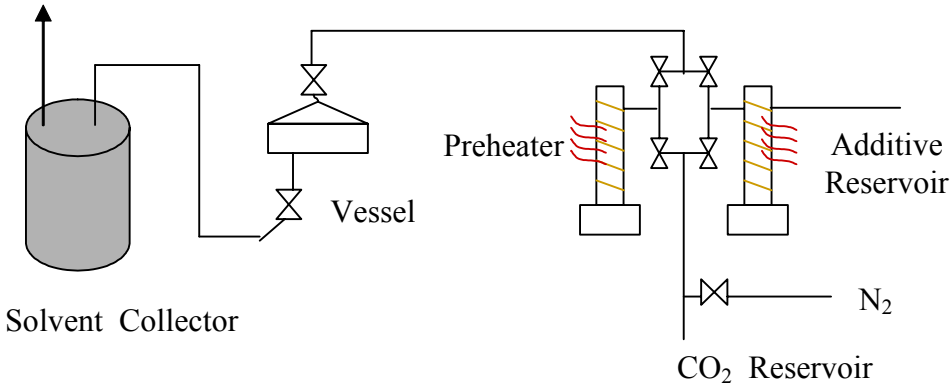

Figure 7.1. The high-pressure 8-inch wafer treatment system schematic.

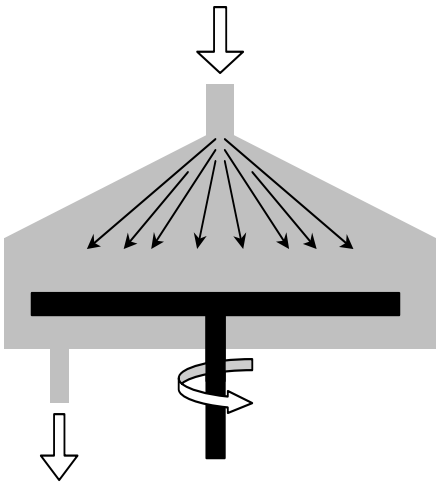

Figure 7.2. A schematic diagram of the center-fed flow reactor in which samples are rotated on an 8-inch platen.

The main vessel is capable of holding pressures up to 2000 psi and may be heated to 350 ºC. A rotating platen is machined to hold 8-inch wafers, while a modified platen has been machined to hold smaller samples. The seal is made with a PTFE gasket and 12 compression bolts in the vessel head.

The vessel is pressurized by means of multiple syringe pumps, specifically Isco model 1000D. These pumps are capable of delivering fluid at a rate of 408 mL/min, and at pressures up to 2000 psi. An air valve assembly is used to connect multiple pumps and is controlled through a single Isco controller. The vessel effluent is exhausted to a large expansion vessel where most liquid additives are separated from the CO_2 phase.

A similar system was also designed and assembled for treatment of 4-inch wafers. This system was modified from the 8-inch system by reducing the volume of the main pressure vessel. The 4-inch vessel head is nearly flat to reduce the total internal volume of the head. This allows a faster fluid charging rate and reduced consumption of chemicals. This system has also been equipped with a view cell connected in parallel to the high-pressure vessel for monitoring of the phase boundary location in relation to the sample wafer. This system is pictured in Figure 7.3. The ability to process full wafers permits relating bench top results to industrial-scale processes. Also, this system is well suited for 4-inch wafers that can be processed in the Microelectronics Research Center cleanroom facilities at Georgia Tech.

Figure 7.3. Picture of the complete high pressure system used to investigate GXL treatment of films.

A small steel cross capable of 3500 psi operation allows samples approximately 1 cm on a side to be studied. One arm of this cross is equipped with a sapphire window. This allows direct observation of the phase, phase boundary of fluids within the reactor and of dissolution of a film sample. In addition, the window is equipped with a spectrometer. A technique for measuring the refractive indices of GXLs has been developed with this spectrometer for measuring fluid composition. The thickness and refractive index of a dissolving film (Chapter 6) can also be monitored *in situ*. The high-pressure optical cell is illustrated in Figure 7.4.

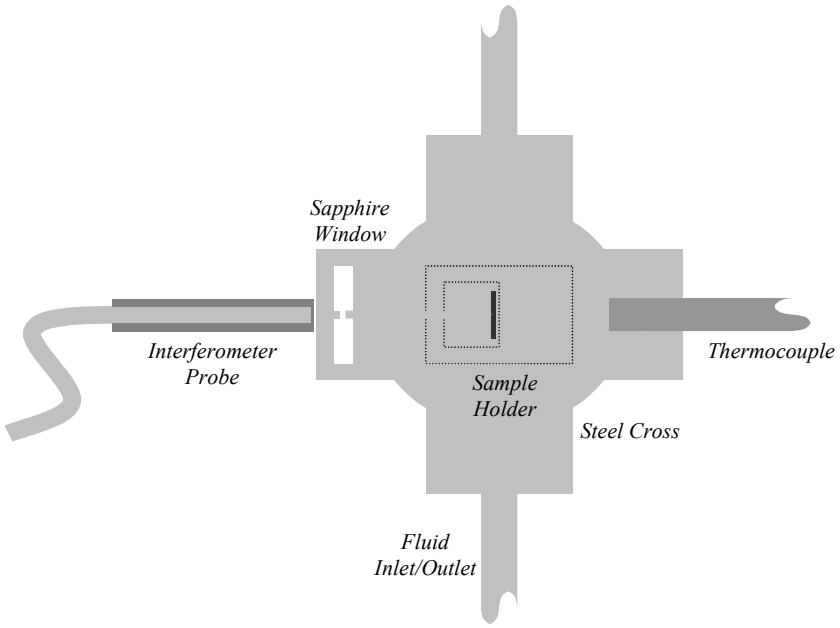

Figure 7.4. A schematic diagram of the dissolution rate monitor for dissolution under elevated pressures.

7.3 Experimental Procedure

One of the most common polymers used in state-of-the-art photoresist is poly-hydroxystyrene (PHOST), a replacement to novolak-based polymers due its reduced absorption of DUV radiation. Thin films were formed by casting a PHOST solution (15wt% by mass in PGMEA, MW=12000, PDI=6.4) at 800 RPM upon a silicon wafer, which previously had the native oxide layer removed by immersion in dilute HF. The film was subsequently baked on a hotplate at 120°C for 5 minutes. Optical constants and thickness of the film were determined using a variable angle spectroscopic ellipsometer (J.Woollam, Lincoln, NE). These quantities are: t=1818nm, A=1.5832, B=0.00812, C=2.885E-4, where the refractive index is given by $A+B/\lambda^2+C/\lambda^4$ and λ is the wavelength (μm). The wafer was then diced into pieces approximately 0.5 cm^2 such that they could be placed upon a sample holder and into a reaction chamber.

CO_2 was purchased from Air Products (Coleman grade, 99.5%). The vapor pressure of CO_2 is 6 MPa at room temperature (~22°C). All experiments were performed at room temperature, while the reaction chamber temperature was monitored with a thermocouple directly inserted into the reaction chamber. For operating pressures other than those of the CO_2 cylinder, an ISCO 1000 D syringe pump was used to both attain and maintain the pressure setpoint.

Films were subsequently treated in the high-pressure reactors with CO_2-expanded liquids. Samples were mounted on a customized sample holder and loaded into the chamber. The system was then pressurized with pure CO_2. In parallel, GXLs were formulated as described in Chapter 3.

The films were monitored both prior to and during liquid immersion by interferometry (Chapter 6). The samples were then removed from the chamber and analyzed by XPS and SEM.

7.4 Organic Residue Removal from Silicon

At the industrial level, cleaning processes are most accurately evaluated by treating a device wafer and comparing its yield to a wafer treated in other ways. The process with the best yield is then selected. However, to evaluate cleaning formulations without the fabrication of a complete functioning device, SEM is frequently used to observe residues before and after a cleaning process. Unfortunately, no chemical information about the residues is obtained.

In order to best develop processes for cleaning of post-etch structures, residues must be characterized. Only if the level of cleanliness resulting from a cleaning process can be quantified can an effective cleaning process be established.

XPS is a primary tool used to determine atomic composition and bonding structure of solid surfaces (Woodruff, 1999). In this technique, an x-ray source is used to irradiate a sample, causing the photoemission of core electrons. The binding energy of these emitted electrons is representative of the chemical species and bonds present in the sample, while the intensity relates to the atomic concentration. Although incident x-rays have a mean free path of about 10 microns, photoelectrons created only have a mean free path on the order of 1-10 nm, resulting in excellent depth resolution.

XPS has been primarily used to analyze organic residue on silicon substrates following treatment with GXLs. The ability of a process to remove photoresist can be evaluated by measuring the atomic composition of the surface. A clean silicon wafer is sufficiently conductive that no surface charging will occur. However, silicon exposed to ambient air will oxidize and will adsorb adventitious carbon.

Photoresist-coated silicon wafers will yield a significantly different XPS spectrum, in that the underlying silicon is not detectable if organic material of thickness greater than 10 nm is present. Furthermore, the nonconductive nature of the polymeric residue will cause surface charging, which is apparent in the form of a shift in the binding energy of observed peaks. Therefore, both the atomic concentration of silicon and the binding energy shift of the C1s peak serve as quantitative indicators of the amount of organic residue remaining on a surface.

7.5 Results and Discussion

PHOST samples were treated with CO_2-expanded ethanol. Ethanol is a commonly used solvent in the microelectronics industry and is an excellent solvent for

complete dissolution of these PHOST films. Liquid CO_2, however, does not dissolve these films.

Single wavelength interferometry (Figure 7.5) indicates that the film begins to swell significantly upon exposure to ethanol/CO_2 vapor. This is further quantified with multiwavelength interferometry, which indicates that the film swells in thickness by a factor of 4 (Figure 7.6) in ethanol vapor. After exposure to the liquid (at t = 24000 ms), no interference is detectable. This observation can be attributed either to complete removal of the films or to film cracking, which leads to significant scattering of the light. SEM and XPS were used to determine which of these possibilities is occurring in a particular sample. Even when GXLs incompletely remove PHOST films, partial dissolution yields an extremely rough, nonuniform residue (similar to Figure 7.11). Scattering from this surface prevents an interferogram from being acquired; thus, real time dissolution rate data in GXLs is not possible for this particular film.

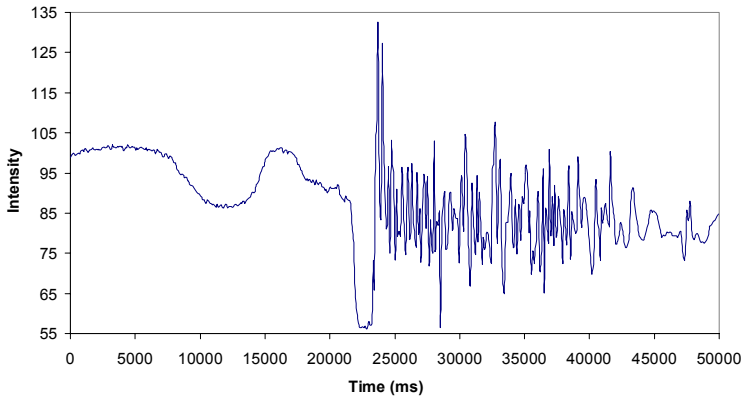

Figure 7.5. Single wavelength interference spectrum for PHOST exposed to CO_2-expanded ethanol at 5 MPa. The liquid contacts the sample at t = 22 sec, at which time the intensity drops significantly due to interference with the meniscus. Swelling occurs prior to liquid exposure, characterized by the oscillation of the intensity. No film is detectable after liquid submersion, likely due to rapid dissolution.

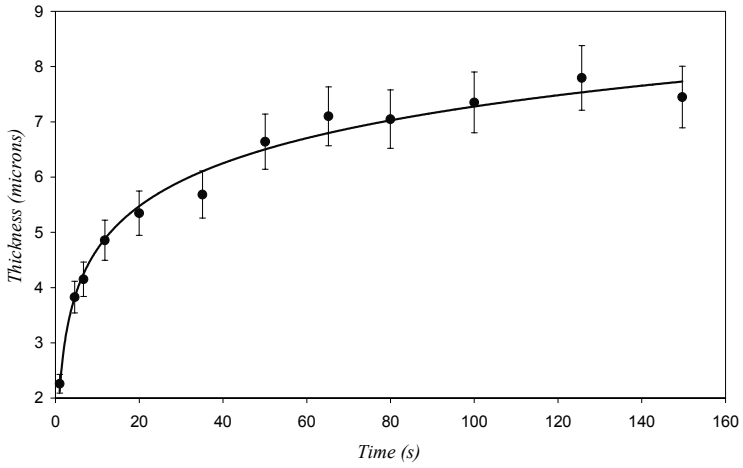

Figure 7.6. Swelling of PHOST upon exposure to ethanol vapor.

XPS results are shown in Figure 7.7 and 7.8. For films in which large amounts of residual polymer remain on the substrate, no silicon is detectable and significant charging of the surface occurs. Silicon is clearly detected on samples with little residue and no shift in the observed binding energy occurs due to charging.

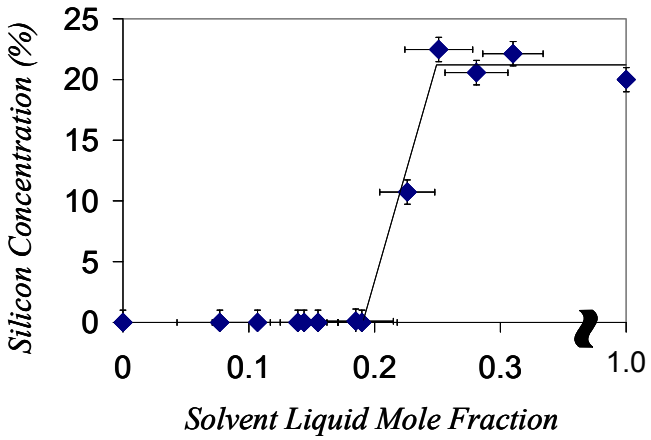

Figure 7.7. Surface concentration following treatment of PHOST films with GXLs of different composition. Ethanol yields a surface with 20% silicon. The same results are obtained with GXLs containing as little as 25% ethanol. GXLs with less ethanol do not remove the PHOST, and no silicon is detected.

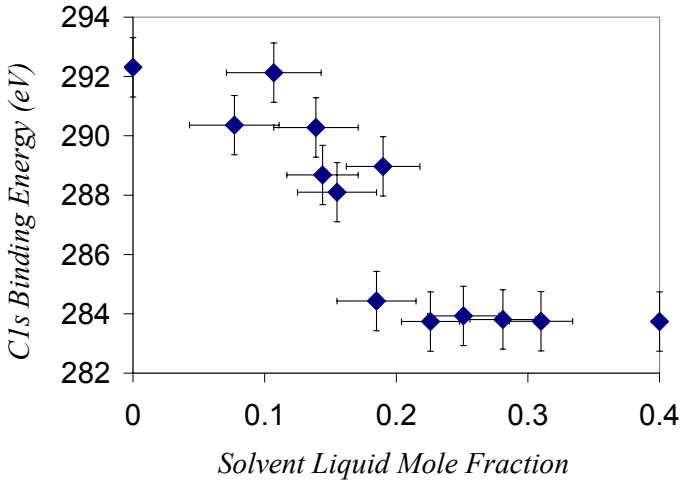

Figure 7.8. C1s binding energy following treatment with GXLs of PHOST films. Ethanol yields a surface with C1s of 284 eV. The same results are obtained with GXLs containing as little as 25% ethanol. GXLs with less ethanol do not completely remove organic material, resulting in a binding energy shift.

SEM was used to estimate qualitatively the amount of residue remaining on the substrate (Figure 7.9). These images correspond well to XPS results, in that no residue is visible on samples in which silicon is detected. However, these images also show the nonuniformities that can result from these processes. The observed cracking and peeling of the polymer likely results from stress developed in the film due to swelling, although the solubility is likely too poor for complete dissolution of the film. There may be local regions in which ethanol is concentrated and selectively removes the polymer, possibly leading to the void formations visible in the film.

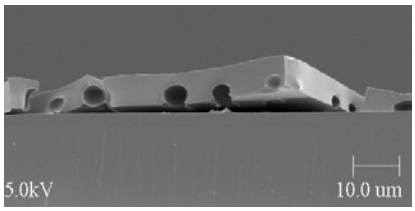

Figure 7.9. The SEM image of PHOST following treatment with CO_2-expanded ethanol at 5.5 MPa and 21ºC indicates large amounts of residual polymer on the silicon substrate.

These results indicate that the amount of residual polymer remaining corresponds well with the concentration of ethanol in the liquid, as expected. For low concentrations of ethanol, little of the polymer is removed, but with up to approximately 75% CO_2 in the GXL the solvent ability of the pure ethanol is maintained. This demonstrates that a solvent such as ethanol may be significantly modified (up to 75%) through expansion with CO_2 while maintaining the solvent ability of the pure liquid.

These PHOST films were also treated with CO_2-expanded NMP. Similar behavior to ethanol is observed, in which mixtures too rich in CO_2 do not remove PHOST. Mixtures up to 5 MPa, or correspondingly 70% CO_2 remove the film. This is quantified with XPS (Figure 7.10), but can be seen visually as well (Figure 7.11).

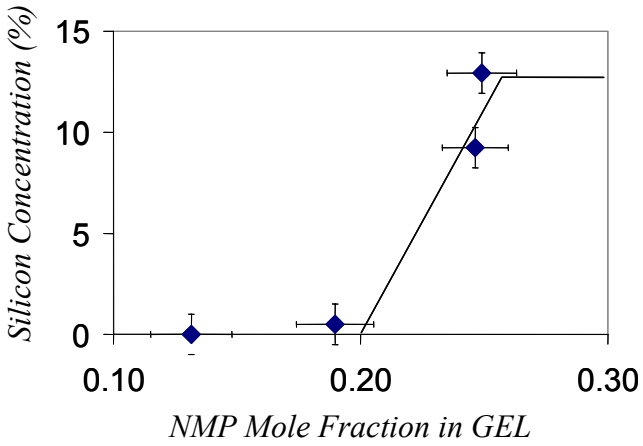

Figure 7.10. Surface concentration following treatment of PHOST films with CO_2-expanded NMP of different composition.

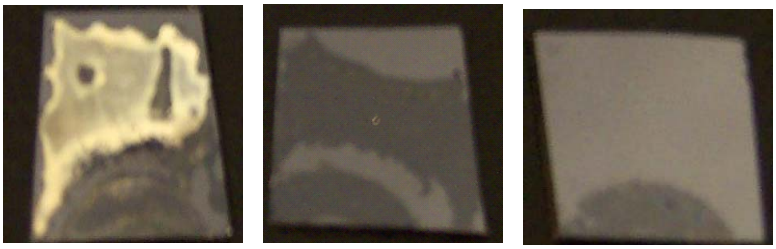

Figure 7.11. Visual inspection following treatment of PHOST films with CO_2-expanded NMP of different composition. From left to right, these samples were treated with GXLs of 15mol%, 20mol%, and 25mol% NMP.

Patterned samples prepared by SEMATECH were also treated with GXLs. These samples are dielectric stacks etched in a fluorocarbon plasma; thus photoresist and post-etch residues remain on the surface and within the patterned features. Additional details of these samples are described elsewhere (Levitin, 2003). XPS results are shown in Table 7.1, in which CO_2-expanded NMP is compared to pure NMP treatment. Although all of these treatments only partially remove residue, GXLs show equivalent results to the pure solvent.

Table 7.1. XPS results of treating patterned samples with CO_2-expanded NMP.

Treatment	Si%	C%	O%	N%	F%	S%
GXL 5.75 MPa	1.4	70.6	17.7	4.7	5.5	0.0
GXL 5.50 MPa	3.4	69.3	16.8	2.9	7.5	0.0
GXL 5.25 MPa	1.7	75.7	16.4	3.2	2.8	0.0
NMP	2.1	73.0	17.0	3.5	4.4	0.0
Untreated	0.0	65.2	24.2	6.1	3.6	0.8

Interferometry of PHOST films during exposure to ethanol and CO_2 suggest ethanol is the dominant specie responsible for dissolution. Although dissolution of PHOST films in aqueous base is reaction-limited and observed to occur through removal of surface layers, dissolution in ethanol proceeds by sorption into the film and swelling of the polymer. Dilute ethanol vapor swells the polymer, but not sufficiently to remove it. CO_2-expanded ethanol similarly swells the polymer, but for low concentrations of ethanol (<25mol%) polymer swelling is insufficient for complete removal. Partial, nonuniform removal may relate to the mobility and dissolution of small molecular weight chains, and rearrangement of chains in a nonplanar order.

Similar studies to these performed with PHOST films were analogously performed with commercially prepared resists from JSR Micro (IXR420H). These films were spin cast and baked at 120°C for 1 minute. Quite different results were obtained with these films than with the PHOST films. GXLs at pressures up to 5750 kPa fully removed the resist, even at exposure times as little as 1 min, suggesting the film lifts off. XPS results of these experiments are shown in Table 7.2.

Table 7.2 XPS results of treating JSR resist with CO_2-expanded NMP.

Treatment	Si%	C%	O%	C1s BE
NMP, 5 min	48.5	15.4	36.1	284.7
GXL 5.75 MPa, 4 min	50.9	15.5	33.6	284.8
GXL 5.75 MPa, 2 min	50.6	15.0	34.4	284.8
GXL 5.75 MPa, 1 min	49.2	12.6	38.2	284.8

Swelling experiments in ethanol vapor were also performed. The observed swelling in dilute ethanol is similar to that observed in PHOST films. The film responds to changes in ethanol concentration through an increase in thickness and a decrease in refractive index.

7.6 Scale-Up of GXL Processes

The theoretical investigation described in Chapters 3, 4, and 5 and the experimental results detailed in this chapter suggest significant opportunities for GXLs in photoresist and etch residue removal. Successful experimental and commercial solvent formulations must be investigated in a prototype production high pressure reactor to assess uniformity and time necessary for photoresist and residue removal. These results can be compared to preliminary, fundamental results to gain insight into scale-up issues in manufacturing; these issues will encompass both throughput considerations for cost-of-ownership evaluations and will indicate limitations in the current design of commercial reactors.

Although it may be possible to reduce the total amount of solvent consumed in a photoresist removal process by reducing the amount of solvent per volume of liquid, it may oppositely be possible that more solvent is consumed if more liquid of reduced

solvent strength must be used. For a mass transfer limited dissolution process, it has been predicted that less solvent need be consumed by using a GXL (Chapter 5). However, if alternative mechanisms to mass transfer dominate residue removal (as suggested by MWI results in Chapter 6), this model is invalid.

In the viewcell reactor, we can experimentally measure the time to remove the film using a traditional liquid and compare this time to that required when using a GXL containing an equivalent amount of solvent. If the removal time is less with a GXL, this suggests that indeed less solvent must be consumed. However, the volume of the reactor, and thus the height of liquid on the sample, may be an important factor. It was previously mentioned that the distance into which the dissolving species penetrates into the liquid is a function of liquid properties. As a result, the optimal liquid height and corresponding reactor volume may be different for different liquids. Therefore, comparing different liquids in the same reactor may not represent a completely valid comparison. The same issue applies to our 4-inch center-fed reactor, although rather than using in situ optical techniques to measure the removal time, ellipsometry and XPS can be used to evaluate the thickness of remaining film after treatment. This information can allow evaluation of possible cost savings due to a reduction in chemical usage, which will lower the operating cost of these GXL processes.

7.7 Conclusion

Conceptual demonstration of the use of CO_2-expanded solvents for photoresist and post-etch residue removal has been performed. Of specific interest are the effects of carbon dioxide, saturated vapor, and gas-expanded liquids upon films such as

polyhydroxystyrene (PHOST). These experiments illustrate the tunability of GXLs through the removal of PHOST-based films using CO_2-expanded solvents. CO_2-expanded ethanol and NMP containing up to approximately 75mol% of CO_2 maintains the removal ability/solvent strength of pure solvent. These fluids can therefore be modified to obtain optimal physical properties and optimal ES&H properties.

XPS and MWI results suggest removal of PHOST-based films occur by means of incorporation of ethanol into the polymer phase. If polymer chains are free to move, the film swells; if sufficient swelling occurs, polymer chains release from the surface. However, if polymer chain mobility is minimal, removal of the film may occur due to stress-induced lift off from the substrate.

CHAPTER 8

CONCLUSIONS

The extension of conventional liquid-phase cleaning processes used in the fabrication of state-of-the-art integrated circuits is questionable for geometries in the sub-100 nm range. Therefore, predictive physical models have been formulated to evaluate process merits such as wetting, dissolution rate, and solvent consumption. Gas-expanded liquids (GXLs) appear to be an especially useful class of fluids for photoresist and residue removal. The properties of these liquids can be varied significantly with pressure, allowing for enhancement of dissolution rates and wetting while reducing the amount of solvent consumed.

A model has been developed to investigate how processing variables directly correlate to the wetting time contribution of liquid-phase processes. The direct relationship between wetting time and surface tension, contact angle, fluid density, viscosity, temperature, pressure, flow rate, flow profile, diffusivity, and solubility allows optimal process design with respect to wetting. This numerical model is used to identify specific conditions under which wetting time may be significant, and therefore must be considered in the design of a cleaning or surface preparation process. In particular, wetting time may be important for features with a large height-width product, for processes in which the contact angle approaches 90°, and for processes in which total processing time must be small for adequate throughput.

An analytical model has also been derived for conditions in which wetting is diffusion controlled. From this model, a simple expression for wetting time is derived

and the effects of feature geometry and contact angle are investigated. This analysis predicts how wetting will scale in future device generations. Wetting times are reduced as the diameter and height of features is reduced, suggesting that it will not be increasingly difficult to wet nanoscale features found in integrated circuits with traditional liquids. However, when the gas-solid interfacial tension is greater than or on the order of the liquid-solid interfacial tension (i.e. the contact angle approaches 90°), the wetting time is significant. This may be particularly applicable when using aqueous liquids with hydrophobic films or polymer residues.

Although weakly wetting liquids can impact total process time and uniformity, strongly wetting liquids will also impact yield. More sensitive film patterns such as high aspect ratio photoresist lines can collapse due to capillary forces. Wetting liquids also may affect the physical properties of a material, particularly the geometry and dielectric constant of a patterned polymer film. Therefore, design equations such as those derived can provide useful insight for the design of improved, optimized chemical processes for future generations of integrated circuits and other state-of-the-art microdevices. The tunability of GXLs with respect to reduced surface tension and improved transport properties may prove useful for overcoming these issues.

Physical models have also been assembled to describe dissolution in terms of fluid properties. The effects of viscosity, density, surface tension, contact angle, diffusivity, and other properties can therefore be quantified. In this work, transport within nanoscale features and the dissolution rate from a rotating substrate are quantified as functions of physical properties of a liquid using transport theory. These transport models are used to evaluate the possible advantages of GXLs, which combine improved

physical properties over traditional liquids with the environmental advantages associated with CO_2-based fluids. This analysis suggests that transport within nanoscale features is aided due to the increased diffusivity in GXLs. Therefore, GXLs may be a useful alternative to traditional liquids in microelectronic processes that are limited by transport within nanoscale features.

The improved transport properties of GXLs relative to traditional liquids also lead to increased dissolution rates when compared on the basis of both rotation rate and solvent consumption. In addition, less solvent must be consumed when using a GXL relative to a traditional liquid for equivalent flow rates. Therefore, tremendous environmental improvements may be realized without sacrificing performance in photoresist and residue removal processes.

Interferometry has been developed as an analytical tool well suited for *in situ* analysis of film removal with GXLs. A real-time interferometric approach has been developed to monitor both film thickness and refractive index. Furthermore, these measurements can be performed using relatively inexpensive, commercially available system components. In addition, refractive indices of pure liquids and liquid mixtures can be measured, including elevated pressure fluids. Film thickness and refractive index measurements of polymer thin films are consistent with measurements obtained by spectroscopic ellipsometry. These film properties can also be measured dynamically, and thus can be applied to dissolution and swelling.

Experiments have been performed that illustrate the tunability of GXLs through the removal of PHOST films using CO_2-expanded ethanol and NMP. Conceptual demonstration of the use of CO_2-expanded solvents for photoresist and post-etch residue

removal has been performed. Of specific interest were the effects of carbon dioxide, saturated vapor, and gas-expanded liquids on the property changes of films such as polyhydroxystyrene (PHOST). CO_2-expanded ethanol and NMP containing up to 75mol% of CO_2 maintain the removal ability of the pure solvents. These fluids can therefore be modified to obtain optimal physical properties and improved ES&H properties. GXLs are able to remove PHOST-based films from silicon substrates through swelling, polymer chain disentanglement, and stress-induced liftoff.

CHAPTER 9

FUTURE WORK

9.1 Mechanistic Studies of Polymer Removal in CO_2

In addition to mass transport, other mechanistic steps that may be important to complete photoresist film removal include disentanglement of polymer chains, formation of a solvent rich gel phase at the interface of a dissolving film, and reaction of solvent with insoluble species to form soluble products (Hunek and Cussler, 2002). It is possible that the rate-limiting step in a GXL is different from that in a pure solvent due to the effects of pressure and CO_2 interactions. In fact, specific molecular interactions between CO_2 and polymers have been identified (Kazarian, 1996) that may affect polymer solubility. Also, CO_2 has been shown to accelerate the transport of species into a polymer (Berens, 1992), also likely affecting removal. Interactions between CO_2 and polymer chains suggest that solubility, and thus transport and dissolution, may be enhanced relative to that which would be expected if CO_2 did not interact with the polymer and simply served as a diluent. These effects may lead to greater removal rates than would otherwise occur simply due to improvements in the transport properties of the GXL.

Efforts should be made to account for these more complex effects. One approach to addressing such effects is to use ethane as an expansion gas. Ethane is soluble in many organic solvents and therefore can be used for GXLs; however, ethane lacks the quadrupolar molecular interactions common with CO_2. Specifically, interactions can exist with the carbonyl oxygen in PMMA or the hydroxyl group in PHOST. Indeed,

effects due to CO_2 addition to water under elevated pressure and temperature in the removal of photoresist films have been observed that cannot be accounted for by acidity of the water (Chavez, Bakker, Hess, 2001). Some properties of ethane and carbon dioxide are shown in Table 9.1.

Table 9.1. Comparisons of select properties of ethane and carbon dioxide.

	ethane	carbon dioxide
Molecular Weight	30	44
Critical Temperature (C)	32.17	31.06
Critical Pressure (MPa)	48.7	73.8
Liquid Molar Volume (mL/mol)	55.2	37.3
Solubility Parameter (J/cc)1/2	12.4	14.56
Dipole Moment	0	0
Liquid Density at 298K (g/cc)	0.316	0.716
Viscosity at 298K (Pa-s)	3.73E-05	6.43E-05
Surface Tension at 298K (N/m)	8.60E-04	5.85E-04

By comparing ethane- and CO_2-expanded solvents, the specific effects of CO_2 may be identified. That is, if ethane is used in a similar manner as CO_2 to modify the physical properties of the liquid, but different dissolution rates are observed, this may be attributed to the specific CO_2-polymer interactions. One particular experimental technique that may be useful for investigating these interactions are microbalance sorption studies in which the mass of a polymer film is measured as a function of CO_2 or ethane pressure. Large sorption of a particular gas by a polymer can indicate significant interactions between the two components. A quartz crystal microbalance (QCM) within a high pressure cell, a tool being assembled by equipping existing high pressure systems with feedthroughs for electrical contacts, can be especially useful for these measurements. Changes in the mass of thin polymer films deposited on these crystals

can readily be detected (Lu, Czanderna, 1984) on the order of ng/cm^2. An additional analytical technique useful for investigating molecular interactions is FTIR. An internal reflection FTIR cell in which films may be treated with elevated pressure fluids is depicted in Figure 9.1 (and detailed in Section 3.5). With this technique, polymer films may be exposed to ethane, carbon dioxide, solvents, and mixtures of these at pressures up to 1000 psi. Infrared absorption spectra can be acquired *in situ* so that chemical interactions between GXLs and polymer films can be investigated during removal.

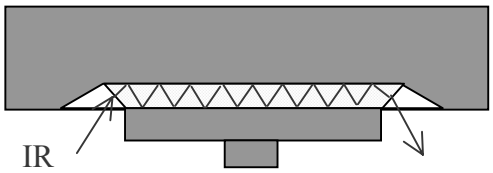

Figure 9.1. Schematic of the FTIR high pressure cell in which a film of interest is deposited on a silicon waveguide. The IR spectrum of the film can be obtained *in situ* as the film is exposed to a GXL.

An additional means to investigate the mechanisms of dissolution in GXLs is to study the effects of modifying the structure of the polymer films. The degree of crosslinking in a polymer film may be modified through baking and exposure to UV light. This degree of crosslinking can have significant effects on the dissolution rate – films of high crosslink density may be resistant to swelling and thus may exhibit a lower dissolution rate in a GXL. Therefore, if swelling significantly impacts the dissolution of a polymer film as expected, additional mechanistic insight may be possible. Microbalance sorption studies can be used to quantify the crosslink density of polymers, since films of greater crosslink density will absorb less gas. This effect can be evaluated from a sorption isotherm with the dual mode sorption model (Stannett, 1979),

$$C = kP + \frac{C'bP}{1+bP} \qquad [9.1]$$

in which the Langmuir capacity parameter, *C'*, is dependent on the crosslink density. In addition, the glass transition temperature (T_g) of a film will vary with crosslink density. T_g may be measured with techniques such as spectroscopic ellipsometry (Keddie, 1994) and Differential Scanning Calorimetry (DSC). Such studies can permit the dissolution rate of a film to be related to film morphology and structure.

9.2 Investigation of Wetting and Feature Collapse

The models of wetting described in Chapter 4 suggest limitations to conventional liquids. However, experimental evidence corresponding to these models is necessary to provide additional insight. There is interest in identifying the conditions under which patterns in photoresist and other materials will collapse and in identifying novel fluids that can be used to overcome this collapse. Some research has been performed to identify collapse caused by drying of water-rinsed features after development. For example, researchers have investigated the use of supercritical fluids for drying. However, there are other indications that collapse may also occur during subsequent wetting steps. Capillary pressures, the cause of pattern collapse, are much greater during wetting than drying and may result in even greater collapse problems. Efforts can be made to identify novel wetting fluids that may alternatively be used when wetting is a problem.

Experimental investigation of wetting could be simplified through scale up to capillaries of diameter on the order of millimeters. In fact, the wetting rate in a closed capillary could be compared to that described by the wetting model described in this thesis. However, for a closed capillary with a diameter of 25 microns, the wetting rate is

predicted to be on the order of microns per day. This rate would to small to detect within experimental error. Therefore submicron features must be used to further study wetting.

E-beam lithography can be used to fabricate high-aspect ratio structures in polymethylmethacrylate (PMMA). Previous research (Cao, Domke, 2000) has indicated that drying of these features will result in deformation for aspect ratios (*AR*) greater than a critical aspect ratio for collapse (*CARC*) given by

$$CARC = w/100 + 1.5 \qquad [9.2]$$

where w is the spacing in nm.

Initial samples can be fabricated in which only the spacing, w, is varied. The height (h), wall thickness (t), gap width (g), and line length (l) can be held constant. These dimensions are illustrated in Figure 9.2. The line length must be large such that line ends do not affect the mechanical strength of the lines. The gap width must be sufficiently large so that wetting is not hindered. The contact angle of water on PMMA has been reported to be 73.7° (Kwok, 1998). With this contact angle and a film thickness of 500 nm, pressure will be generated in a feature having a width less than 1700 nm.

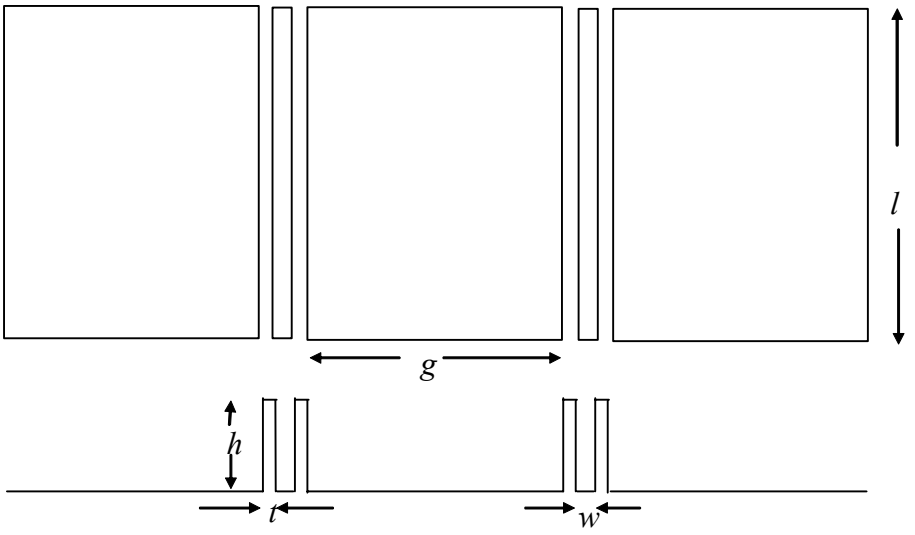

Figure 9.2. The feature geometrical parameters are defined by the height (h), wall thickness (t), line length (l), gap width (g), and line spacing (w).

Once the above pattern has been written with the electron beam, the PMMA can be developed in a standard TMAH solution, rinsed with DIW, and dried with a nitrogen gun. The sample can then be scanned for defects with atomic force microscopy (AFM) and the percentage of collapsed features can be recorded as a function of spacing. According to the previously reported data, the features should collapse during drying only at the lower value of 100 nm. The larger spaced lines should not collapse. If the contact angle and surface tension, γ, of the liquid are known, the pressure gradient, ΔP, generated in the features can be calculated as

$$\Delta P = \frac{2\gamma \cos\theta}{w} \qquad [9.3]$$

The collapse conditions can therefore be correlated to this pressure gradient.

APPENDIX

A. MATLAB Program for Estimating Wettability

```
%Define the input parameters
feature=2;        %feature type - 1 for trench, 2 for cylinder
trig=2*feature;
W=0.15e-6;        %width of feature, in m
H=2e-6;           %height of feature, in m
G=72/1000;        %surface tension of liquid, N/m
CA=25;            %contact angle, degrees
Mu=2/1000;        %liquid viscosity, Pa-s
d=0.03;           %height of fluid on wafer, m
rho=1000;         %liquid density(kg/m3)
henry=150000;     %Henry's constant(Pa-m3/mol)
P0=101325;        %initial pressure of gas in feature, Pa
PA=101325;        %applied pressure to liquid, Pa
D=2e-9;           %diffusivity, m2/s
R=8.314;          %gas constant, J/mol-K
T=300;            %temperature, K
v0=172;           %bulk velocity of liquid, m/s

%calculate pressure in via
Pvia=pvia(W,G,CA,PA,trig,rho,d); %see end of file
ci=Pvia/henry;  %concentration at interface, dimensional, mol/m3
cb=PA/henry;    %concentration in bulk, dimensional, mol/m3
M=H*P0/R/T; %moles in via to be transported - units of mol/m^2

%Define geometry, nodes and size of differences
xf=0.2;     %m
yf=(1+pi)*2*H*P0*henry*W/8/R/T/G/cos(CA*pi/180)*1.1;    %m
tf=pi/D*(H*P0*henry*W/8/R/T/G/cos(CA*pi/180))^2*1.1;;      %Specify the
maximum iteration time
m=50;       %number of steps in x
n=50;       %number of steps in y
dx=xf/m;    %m
dy=yf/n;    %m
dt=dy*dy/2/D;%s

%Initialize nodes and quantities
BC=ones(m,1);       %concentration at the via on surface is 1
Cp=zeros(m,n);      %concentration profile at present time step
Cf=zeros(m,n);      %concentration at future time step
Flux=0;             %flux at surface for a time step
Total=zeros(m,1);     %total moles transported
wettime=zeros(m,1);

%Estimate the velocity profile for flow past a flat plate
%calculate the momentum boundary layer thickness
BL=zeros(m,1);
for i=1:m
   BL(i)=(280/13)^(0.5)*i*dx*(Mu/i/dx/v0/rho)^(0.5);
end
v=zeros(m,n);
for j=(1:n)
```

```
    for i=1:m

        if j<(BL(i)/dy)
            v(i,j)=v0*(1.5*j*dy/BL(i)-0.5*(j*dy/BL(i)).^3);
        else
            v(i,j)=v0;
        end
    end
end
%Can alternately solve the velocity profile using finite difference

%Find the solution to the dimensionless mass balance:
% dC/dt=Dd2C/dy2-vdC/dx

%Solve this equation implicitly using ADI (Alternating Direction
Implicit) Method

%Define the ADI matices
A1=zeros(n,n);
b1=ones(n,1);
A2=zeros(m,m);
b2=ones(m,1);

%Define A1
j=1;
    A1(j,j)=2*D/dy/dy+1/dt;
    A1(j,j+1)=-D/dy/dy;
for j=2:(n-1)
    A1(j,j-1)=-D/dy/dy;
    A1(j,j)=(1/dt+2*D/dy/dy);
    A1(j,j+1)=-D/dy/dy;
end
j=n;
    A1(j,j-2)=-D/dy/dy;
    A1(j,j-1)=2*D/dy/dy;
    A1(j,j)=(1/dt-D/dy/dy);
A1=sparse(A1);

for k=1:2:(tf/dt)
    i=1;
        j=1;
            b1(j)=Cp(i,j)/dt-v(i,j)*Cp(i+1,j)/2/dx+D*BC(i)/dy/dy;
        for j=2:(n-1)
            b1(j)=Cp(i,j)/dt-v(i,j)*Cp(i+1,j)/2/dx;
        end
        j=n;
            b1(j)=Cp(i,j)/dt-v(i,j)*Cp(i+1,j)/2/dx;
        Cf(i,:)=(A1\b1)';

    for i=2:(m-1)
        j=1;
            b1(j)=Cp(i,j)/dt+D*BC(i)/dy/dy-v(i,j)*(Cp(i+1,j)-Cp(i-
1,j))/2/dx;
        for j=2:(n-1)
            b1(j)=Cp(i,j)/dt-v(i,j)*(Cp(i+1,j)-Cp(i-1,j))/2/dx;
        end
        j=n;
```

```
            b1(j)=Cp(i,j)/dt-v(i,j)*(Cp(i+1,j)-Cp(i-1,j))/2/dx;
        Cf(i,:)=(A1\b1)';
    end

    i=m;
        j=1;
            b1(j)=Cp(i,j)/dt+D/dy/dy*BC(i)-v(i,j)*(Cp(i,j)-Cp(i-
1,j))/dx;
        for j=2:(n-1)
            b1(j)=Cp(i,j)/dt-v(i,j)*(Cp(i,j)-Cp(i-1,j))/dx;
        end
        j=n;
            b1(j)=Cp(i,j)/dt-v(i,j)*(Cp(i,j)-Cp(i-1,j))/dx;
        Cf(i,:)=(A1\b1)';

%Calculate the flux at the interface for this time step = D*dC/dy(y=0)
    for i=1:m
        Flux=D*(Cf(i,2)-4*Cf(i,1)+3*BC(i))/2/dy*(ci-cb);
        Total(i)=Total(i)+Flux*dt;
        if Total(i)>M, BC(i)=0; Cf(i,:)=0;
            if wettime(i)==0, wettime(i)=k*dt;  end
        end
    end
    if Total(m)>M, break, end
    Total(m)
    Cp=Cf;

    k=k+1;  %2nd time step of ADI, implicit in x
    j=1;
        i=1;
            A2(i,i)=1/dt;
            A2(i,i+1)=v(i,j)/dx/2;
            b2(i)=Cp(i,j)/dt+D*(Cp(i,j+1)-2*Cp(i,j)+BC(i))/dy/dy;
        for i=2:(m-1)
            A2(i,i-1)=-v(i,j)/2/dx;
            A2(i,i)=1/dt;
            A2(i,i+1)=v(i,j)/2/dx;
            b2(i)=Cp(i,j)/dt+D*(Cp(i,j+1)-2*Cp(i,j)+BC(i))/dy/dy;
        end
        i=m;
            A2(i,i-1)=-v(i,j)/dx;
            A2(i,i)=1/dt+v(i,j)/dx;
            b2(i)=Cp(i,j)/dt+D*(Cp(i,j+1)-2*Cp(i,j)+BC(i))/dy/dy;
        A2=sparse(A2);
        Cf(:,j)=A2\b2;

    for j=2:(n-1)
        i=1;
            A2(i,i)=1/dt;
            A2(i,i+1)=v(i,j)/dx/2;
            b2(i)=Cp(i,j)/dt+D*(Cp(i,j+1)-2*Cp(i,j)+Cp(i,j-1))/dy/dy;
        for i=2:(m-1)
            A2(i,i-1)=-v(i,j)/dx/2;
            A2(i,i)=1/dt;
            A2(i,i+1)=v(i,j)/2/dx;
            b2(i)=Cp(i,j)/dt+D*(Cp(i,j+1)-2*Cp(i,j)+Cp(i,j-1))/dy/dy;
        end
```

```
        i=m;
            A2(i,i-1)=-v(i,j)/dx;
            A2(i,i)=1/dt+v(i,j)/dx;
            b2(i)=Cp(i,j)/dt+D*(Cp(i,j+1)-2*Cp(i,j)+Cp(i,j-1))/dy/dy;
        A2=sparse(A2);
        Cf(:,j)=A2\b2;
    end

    j=n;
        i=1;
            A2(i,i)=1/dt;
            A2(i,i+1)=v(i,j)/dx/2;
            b2(i)=Cp(i,j)/dt+D*(Cp(i,j)-2*Cp(i,j-1)+Cp(i,j-2))/dy/dy;
        for i=2:(m-1)
            A2(i,i-1)=-v(i,j)/2/dx;
            A2(i,i)=1/dt;
            A2(i,i+1)=v(i,j)/2/dx;
            b2(i)=Cp(i,j)/dt+D*(Cp(i,j)-2*Cp(i,j-1)+Cp(i,j-2))/dy/dy;
        end
        i=m;
            A2(i,i-1)=-v(i,j)/dx;
            A2(i,i)=1/dt+v(i,j)/dx;
            b2(i)=Cp(i,j)/dt+D*(Cp(i,j)-2*Cp(i,j-1)+Cp(i,j-2))/dy/dy;
        A2=sparse(A2);
        Cf(:,j)=A2\b2;

%Calculate the flux at the interface for this time step = D*dC/dy(y=0)
    for i=1:m
        Flux=D*(Cf(i,2)-4*Cf(i,1)+3*BC(i))/2/dy*(ci-cb);
        Total(i)=Total(i)+Flux*dt;
        if Total(i)>M, BC(i)=0; Cf(i,:)=0;
            if wettime(i)==0, wettime(i)=k*dt; end
        end
    end
    if Total(m)>M, break, end
    Total(m)
    Cp=Cf;
end
k*dt


function [Pvia]=pvia(W,G,theta,PA,trig,rho,d)
%A function to calculate the pressure in a via
Pint=trig*G*cos(theta*pi/180)/W;
FW=rho*9.79*d;
Pvia=FW+PA+Pint;
```

B. Removal of Native Copper Oxides Using Acetic Acid

Current IC manufacturing utilizes chemical mechanical polishing (CMP) for the planarization of copper films. CMP is often followed by a DI water rinse to remove any slurry residue. However, part of the mechanism of planarization is suggested to be oxidation of the copper. If oxidized copper species remain after CMP, the DI water rinse will not remove the oxidized copper species, and in fact under some conditions may even further oxidize the copper. Organic acids such as acetic acid have been investigated for use in alternate post-CMP copper cleaning process.

Previous investigations in other industries have indicated that acetic acid will effectively remove oxides, and equally important will not etch copper. In fact, vinegar is commonly used in households for cleaning of copper, and copper tanks are the generally recommended for large scale storage of acetic acid. XPS has been used to identify the character and kinetics of copper oxidation species before and after the treatment of copper thin films with acetic acid.

For the study of oxidation character and kinetics, a copper film was deposited onto a silicon wafer with a titanium adhesion layer. This copper film was immersed in glacial acetic acid at 35°C for 1 min, dried with nitrogen, and subsequently exposed to air. These are labeled Samples 1-5; 1 is immediate introduction into the vacuum system (approximately 30 seconds), 2 is 1 min, 3 is 8 min, 4 is 12 min, and 5 is 16 min in air. As the film was exposed to air, the film both oxidizes and adsorbs adventitious carbon. A film exposed to air for a relatively infinite time is Sample 6. XPS spectra of these films are shown in Figures B.1-4, and atomic concentrations are tabulated in Table B.1.

Normalized spectrum, in which the intensity of the peaks are equivalently scaled, are also provided to indicate the relationships of the peak shapes, and thus bonding structure.

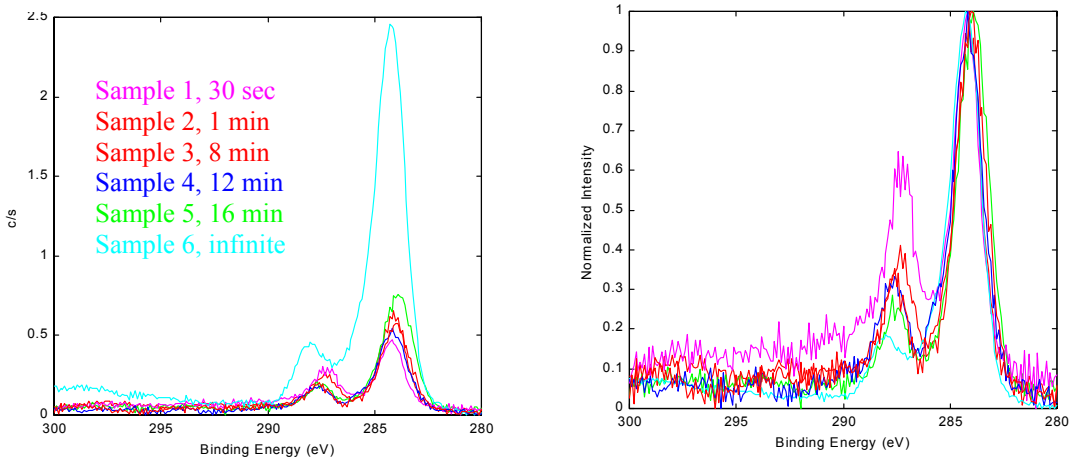

Figure B.1. Absolute (left) and normalized (right) C1s spectra of copper films treated with acetic acid and subsequently exposed to air.

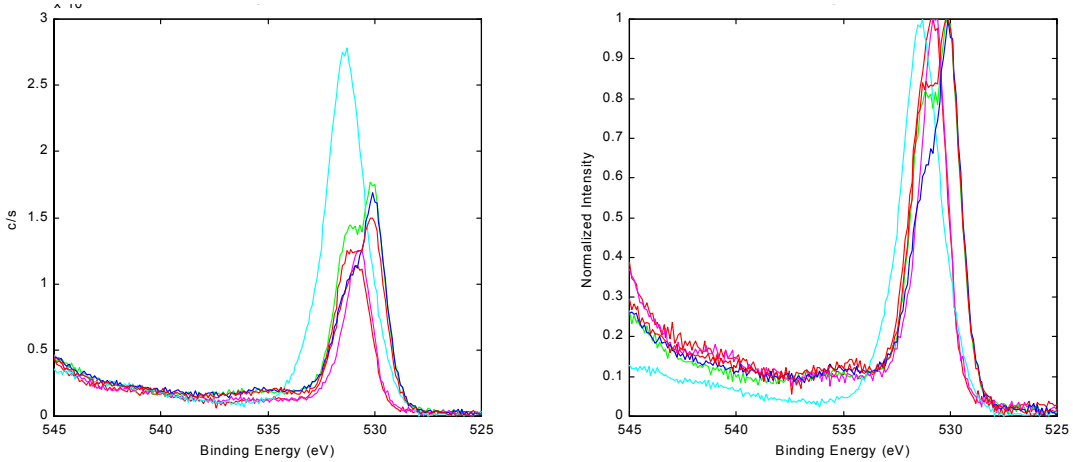

Figure B.2. Absolute (left) and normalized (right) O1s spectra of copper films treated with acetic acid and subsequently exposed to air.

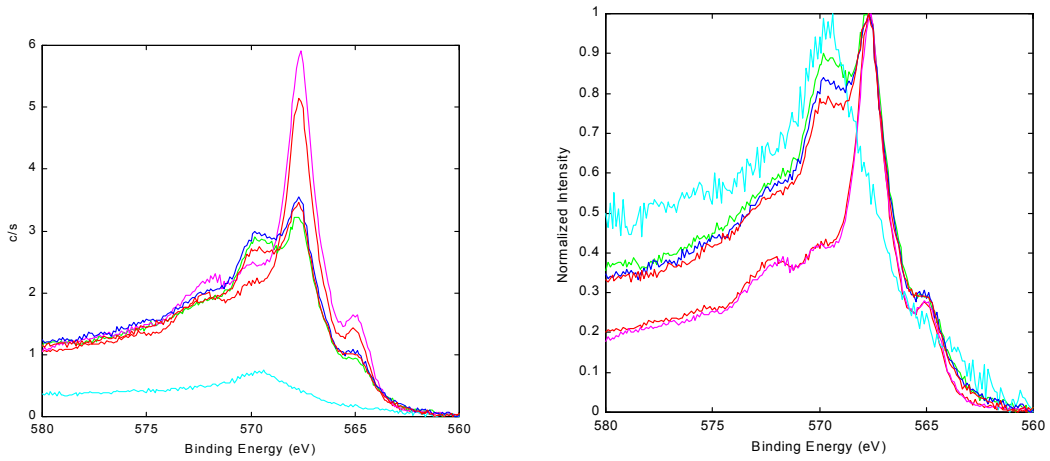

Figure B.3. Absolute (left) and normalized (right) Cu-Auger spectra of copper films treated with acetic acid and subsequently exposed to air.

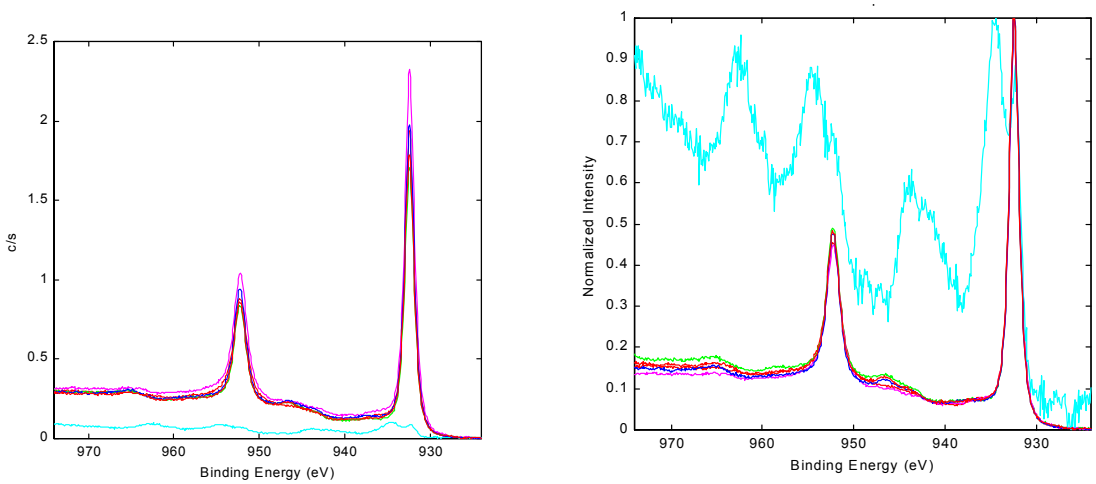

Figure B.4. Absolute (left) and normalized (right) Cu2p spectra of copper films treated with acetic acid and subsequently exposed to air.

Table B.1. The atomic composition of copper films treated with acetic acid and exposed to air. The fraction copper decreases with time as the amount of native oxide and adventitious carbon on the surface increases.

Sample	C%	O%	Cu%	Preparation
1	22.5	14.5	63.7	30 sec air exposure
2	24.4	17.5	58.1	1 min air exposure
3	22.9	26.3	50.8	8 min air exposure
4	22.4	25.6	52.0	12 min air exposure
5	29.1	27.1	43.8	16 min air exposure
6	62.8	30.6	6.5	infinite air exposure

Comparison of the Cu2p peak (Figure B.4) in all samples to the original sample (1) shows a tremendous increase in the proportion of copper in the analyzed region. These spectra are characteristic of a pure copper film, in that only the two peaks of Cu2p3/2 and Cu2p5/2 are present and the shake up peaks present in the original oxide are absent. These spectra indicate that the original thick native oxide is removed. However, a significant amount of oxygen is still present on the surface (Figure B.2).

It is of interest to know the chemical form of the oxygen remaining on the surface. The O1s peak grows with increased air exposure. Previous results (Chavez, 2001) indicate that this oxygen originates from a SiO_2 sublayer, yet this is not present in these samples. The copper Auger region indicates oxidation of copper does, in fact, take place with air exposure. The ratio of metallic copper to its oxides decreases as air exposure time increases. However, this Auger region for the sample with no air exposure is identical to that of a sputtered copper film. This indicates that the oxygen present on the surface is not in the form of a copper oxide.

Further agreement with this conclusion can be noted from the O1s peak. Metal oxides exhibit a lower binding energy than do carbonates. A shoulder is clearly seen in the spectrum. If the lower binding energy is attributed to the metal oxide, it is clear that this peak occurs upon prolonged air exposure.

Carbon is also significantly decreased after exposure to the acetic acid bath, but the concentration increases with increased air exposure. A shifted region of the C1s peak at 288 eV indicates a carbon-oxygen interaction. While previous experiments (Chavez, 2001) show this peak disappearing, it did not disappear here. The ratio of the carboxyl peak to the carbon peak actually was at a maximum at the minimum air exposure then decreased with air exposure.

A further test was completed to determine if dissolved oxygen in the acetic acid was responsible for residual oxygen on the copper surface. Acetic acid was purged with nitrogen for 1 hour to remove any dissolved oxygen. A sample was immersed in the purged acetic acid for 1 minute at 35C and exposed to air for 30 seconds, analogous to Sample 1 (Table B.1). The spectra were virtually identical to those observed previously, indicating dissolved oxygen has little if any effect on the concentration of oxygen on the copper surface.

Therefore, glacial acetic acid removes the native oxide from copper films. Residual carbonates remain on the copper surface, and upon exposure to air, oxidation and adventitious carbon deposition increases with time. This study indicates the scope and capabilities of XPS for metal and metal oxide analysis.

C. Spatial Resolution on Patterned Surfaces (SR-XPS)

For patterned, nonplanar films, XPS analysis becomes much more difficult. Unfortunately, XPS has poor lateral resolution since it is limited by its large analysis area (1-mm diameter spot). Because devices of interest are sub-micron, it is not possible to directly sample these regions. However, the surface sensitivity can be utilized in such a way that different geometrical regions may be analyzed. This spatial resolution (SR) demands careful manipulation of the orientation of not only the sample, but of the analyzer and x-ray source. By varying the angle of the sample relative to the detector, certain regions of the sample can be shadowed from either the x-ray source or the electron detector.

The appropriate angle is dependent upon the geometry of the sample. First, a sample having equispaced lines, vertical sidewalls, and square edges is considered. The aspect ratio, A, can be defined as the height of the trench, *h*, divided by the width of the trench, *w*. This basis is illustrated in Figure C.1.

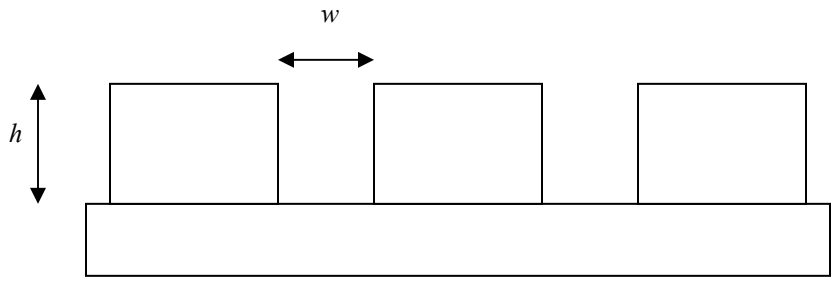

Figure C.1. Basic geometry of line/trench sample.

For these analyses, x-ray shading or electron shading is used. In x-ray shading, the sample is tilted relative to the x-ray source so that the mask layer and geometric features prevent the bottom of the trench from being directly exposed. Photoemission

from the bottom of the trench does not take place. When electron shading is used, the sample is angled so that the trench bottom is not in the line of sight of the electron energy analyzer. In this case the analyzer primarily collects photoelectrons from the sidewalls and top layer of the sample. A schematic of these techniques appears in Figure C.2. This method is a less destructive approach than alternates available and requires no special sample preparation, allowing *in situ* analyses (Oehrlein, 1998).

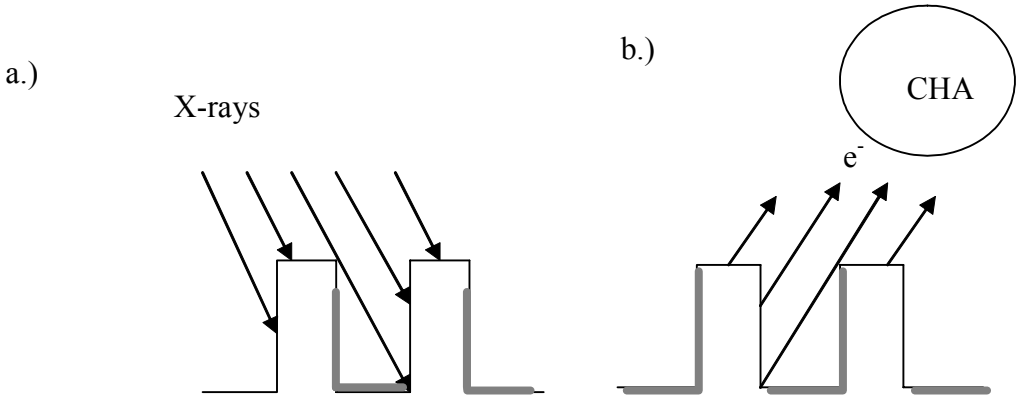

Figure C.2. Illustration of a.) x-ray shading, and b.) electron shading. Gray lines indicate shadowed regions.

The shading approaches have been used in several studies. For instance, one study used an oxide masked silicon wafer patterned with an $SF_6/50\%O_2$ reactive ion etch (Oehrlein, 1998). The XPS spectra contained Si 2p, O 1s, and F 1s peaks that were analyzed with the aforementioned method. The sidewall film was determined to be a SiF_xO_y material with oxygen/silicon and fluorine/silicon ratios of 1.7 and 1.0, respectively. XPS spectrum of the Si 2p peaks at different takeoff angles, for instance, yield distinct peaks for photoelectrons originating from the silicon in the substrate, trench, sidewall film, and oxide mask (Oehrlein, 1998).

This technique offers the ability to analyze sidewalls without cleavage of the sample. However, the geometry of the sample must be known and must be uniform over an area greater than the spot size of the x-ray beam. Unfortunately, samples of this basic geometry are difficult to fabricate. Commonly, sidewalls are sloped and corners are rounded. Furthermore, electrons and photons have a finite penetration depth (this is a function of the material, but is on the order of 1 nm for electrons and 1 micron for x-rays).

A pattern with sloped sidewalls is illustrated in Figure C.3. It is important to know how this profile would alter our ability to use SRXPS. Preliminary experiments have been performed to evaluate the feasibility of using this technique with the XPS available in our lab. It is proposed that an alternate method for determining the appropriate angles to resolve particular regions of a patterned film involves performing an analysis of the ratio of the main component of the trench bottoms to the main component of the line tops at varying angles with respect to the analyzer. Furthermore, the efficiency of x-ray and electron shading may be determined by this analysis.

Figure C.3. Nonideal pattern with sloped sidewalls.

Line-space patterns were fabricated by etching a 1-micron aluminum film (Figure C.4). This pattern was uniform over the entire region of the sample. Lines were approximately 10 microns wide: spaces were approximately 3 microns wide.

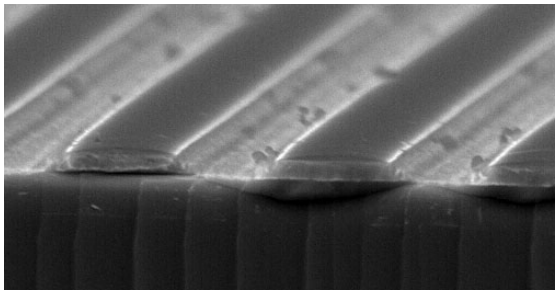

Figure C.4. Plasma etched aluminum lines, (nominally 3 micron lines, 10 micron spaces).

First, the sample was aligned in the XPS chamber such that the lines were perpendicular to the source-analyzer plane. The sample was then rotated to various angles in this axis. Angles are defined with respect to the analyzer. The angle was varied from 20 to 75 degrees at intervals of 2.5 degrees. The binding energy regions characteristic of silicon and aluminum were analyzed. It is assumed that the predominant specie in the trench is silicon while the material on the top of the line is aluminum. Although silicon may be sputtered from the bottom of the trench and redeposit on the top of the lines, and aluminum may be deposited in the trench, the ratio Al:Si should be a maximum when the trench bottom is shadowed and minimum when the trench is fully exposed to the detector. Data were recorded as Al% in the total concentration of Si and Al detected.

In Figure C.5, it can be readily seen that by changing the orientation of the sample, different regions of the pattern are exposed. It is interesting to note that the curve is not symmetric about 45 degrees. At angles less than 45 degrees, the basis of shadowing is electron shadowing, while at angles greater than 45 degrees, the x-rays are shadowed. If these two effects were equally efficient the minimum of the plot would occur at 45 degrees.

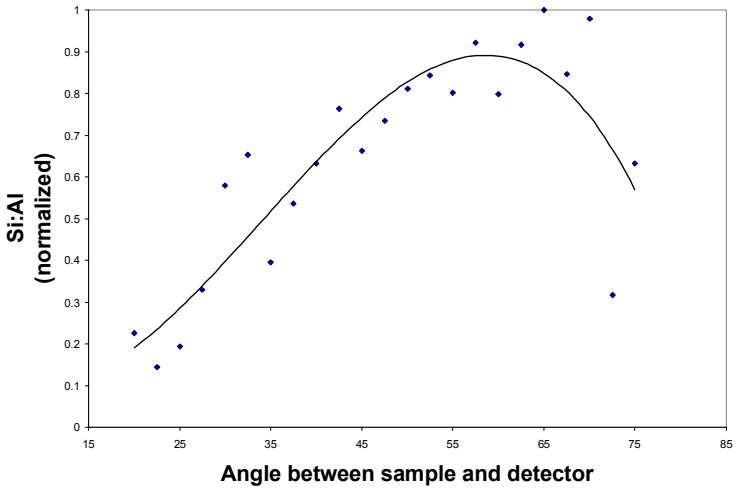

Figure C.5. Plot showing the effects of take off angle on trench area exposed. Aluminum lines are oriented perpendicular to analyzer.

At 45 degrees, a portion of the trench bottom is detected. As the angle is increased, the detector sees more of the bottom, and less of the bottom is directly exposed to the x-rays. But since the x-rays have a deeper penetration depth, fewer x-rays are blocked from the trench bottom than are exposed to the detector. Hence, more of the trench bottom is detected. As the angle is further increased the x-rays are completely blocked and a decrease in bottom signal is detected. Since the maximum is shifted to approximately 60 degrees, it is clear that x-ray shadowing is less effective than electron shadowing, which can be attributed to the difference in the mean free paths.

If the bottom of the trench were fully shadowed, a further change in the angle would not change the Al%, and the slope of the trendline would approach a value equivalent to the composition of the line tops. The data does not conclusively reach a minimum at 25 degrees; additional data at angles less than 20 and greater than 75 are

needed to draw further conclusions. Also, scans of higher resolution should reduce the scatter in the data.

For the sample analyzed, the critical angle for which the bottom of the trench is completely shadowed is 25 degrees. Electron shadowing gives better results in shadowing the bottom of the trench.

The results shown in Figure C.6 compare spectra obtained when lines are aligned parallel and perpendicular to the analyzer. It is apparent that some qualitative information relating to the spatial distribution in atomic concentrations can be obtained, although quantifying the data is difficult.

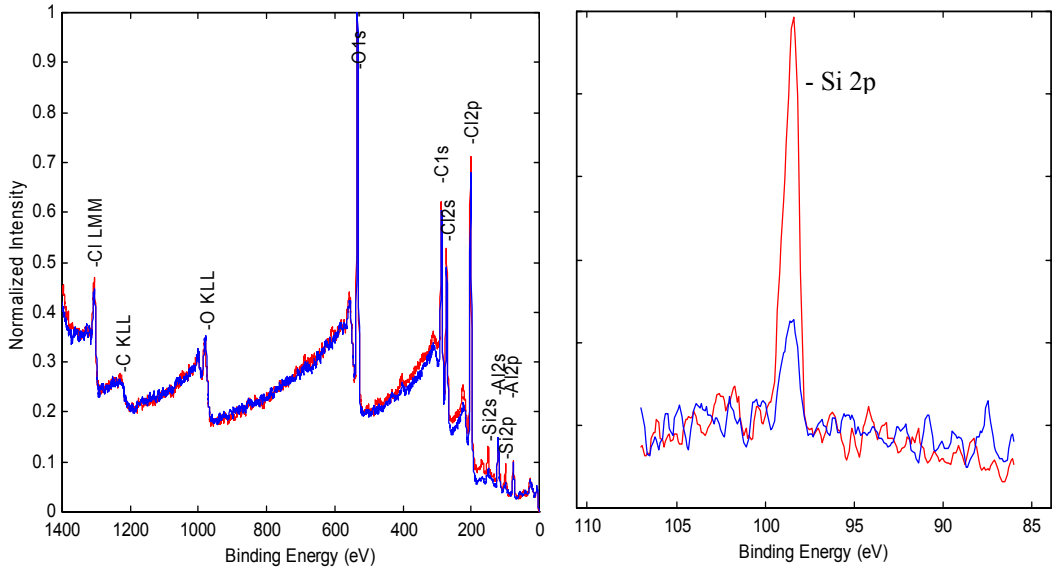

Figure C.6. Blue spectrum: aluminum lines are oriented perpendicular to analyzer. Red spectrum: aluminum lines are oriented parallel to analyzer. With trenches exposed (Red), the atomic concentration of Si is 3.6% while when unexposed it is 0.5%.

SR-XPS is capable of detecting elements at fractions of an atomic percent. Perhaps this approach can be used in parallel with electrical testing to evaluate effective cleaning or may be useful when electrical testing is unavailable. However, spatial resolution is limited if the geometry of the sample is poorly defined and dependent upon the ability to precisely adjust the relative position of the sample to the x-ray source and detector.

REFERENCES

Agrawal, A. and C.L. Henderson, *Proceedings of SPIE*, **5038**, p. 1026-1037 (2003).

Bakker, G.L. and D.W. Hess, *Rev. Sci. Instrum.*, **68** (1), p. 184-188 (1997).

Berens, A.R., G.S. Huvard, R.W. Korsmeyer, and F.W. Kunig, *Journal of Applied Polymer Science*, **46**, p. 231-242 (1992).

Bertucco, A. "Precipitation and Crystallization Techniques," in *Chemical Synthesis Using Supercritical Fluids*; P.G. Jessop, and W. Leitner, eds.; Weinheim: Wiley-VCH (1999).

Bird, R.B., W.E. Stewart, and E.N. Lightfoot. *Transport Phenomena*. New York: Wiley, p. 46 (1960).

Braun, A.E., *Semiconductor International*, p. 89, February (2001).

Braun, A.E*., Semiconductor International*, p. 76-90, September (2000).

Burns, S., G. Schmid, B. Trinque, J. Willson, J. Wunderlich, P. Tsiartas, J.C. Taylor, R. Burns, C.G. Willson, *Proceedings of SPIE*, **5039**, p. 1063-1075 (2003).

Campbell, S.A. *The Science and Engineering of Microelectronic Fabrication*. New York: Oxford University Press (1996).

Cao, H.B., P.F. Nealy, and W.D. Domke, *J. Vac. Sci. Technol. B*, **18** (6), p. 3303-3307 (2000).

Chang, C.J., and A.D. Randolph, *Biotechnology Progress*, **7**, p. 275-278 (1991).

Chang, C.J, K.L. Chiu, and C.Y. Day, *Journal of Supercritical Fluids*, **12**, p. 223-237 (1998).

Chavez, K.L., G.L. Bakker, and D.W. Hess, *J. Vacuum Science and Technology B,* **19**, p. 2144-2148 (2001).

Chavez, K.L. and D.W. Hess, *Journal of the Electrochemical Society*, **148** (11), p. G640-G643 (2001).

Churaev, N.V. *Liquid and Vapor Flows in Porous Bodies, (Topics in chemical engineering, V. 13)*. Amsterdam: Overseas Publishers Association, p. 274-275 (2000).

Crowl, D.A. and J.F. Louvar. *Chemical Process Safety: Fundamentals with Applications*. Englewood Cliffs, New Jersey: Prentice Hall, p. 160-166 (1999).

Cussler, E.L. *Diffusion Mass Transfer in Fluid Systems, 2nd Ed*. New York: Cambridge University Press, (1997).

de Gennes, P.G. *Reviews of Modern Physics*, **57 (**3), Part 1, p. 827-863 (1985).

DeJule, R., *Semiconductor International*, June (2000).

Dettre, R. and R. Johnson, " Contact Angle Hysteresis II: Contact Angle Measurements on Rough Surfaces," in *Contact Angle, Wettablility and Adhesion* (F.M. Fowkes, Ed.), Advances in Chemistry Series, No. 43 (American Chemical Society, Washington, D.C.), p. 136-144 (1964).

DIPPR, Thermophysical property database at *http://www.che.gatech.edu/dippr,* Public Release (2002).

Dornisch, D., G. Li, and M. Brongo**,** *Solid State Technology*, **43** (5) (2000).

Eckert, C.A., D. Bush, J.S. Brown, C.L. Liotta, *Ind. Eng. Chem. Res.*, **39**, p. 4615-4621 (2000).

Goldfarb, D.L., J.J. de Pablo, P.F. Nealey, J.P. Simons, W.M. Moreau and M. Angelopoulos, *J. Vac. Sci. Technol. B,* **18** (6), p. 3313-3317 (2000).

Heavens, O.S. *Optical Properties of Thin Solid Films*. New York: Dover Publications (1991).

Hebda, A.D., K.A. Romero, D.M. Seif, and T.W. Peterson in *Cleaning Technology in Semiconductor Device Manufacturing IV,* T. Hattori, R. E. Novak, and J. Ruzyllo, Editors, PV 99-36, p. 569-576, The Electrochemical Society Proceedings Series, Pennington, NJ (1999).

Henderson, C.L, *PhD Dissertation*, University of Texas-Austin (1998).

Hunek, B., and E.L. Cussler, *AIChE Journal*, **48** (4), p. 661-672 (2002).

Johnson, E.A. and T.F. Morse, U.S. Patent 6,278,809 (2001).

Kamal, T. *PhD Dissertation*, School of Chemical Engineering, Georgia Institute of Technology (2000).

Kanegsberg, B., ed. *Handbook for Critical Cleaning*. CRC Press: New York (2001).

Kazarian, S.G., M.F. Vincent, F.V. Bright, C.L. Liotta, and C.A. Eckert, *J. Am. Chem. Soc.*, **118**, p. 1729-1736 (1996).

Keddie, J.L., R.A.L. Jones, and R.A. Cory, *Europhys. Lett.,* **27**, p. 59 (1994).

Kern, W. and D.A. Puotinen, *RCA review*, **187**, June (1970).

Kern, W., ed. *Handbook of Semiconductor Cleaning Technology*. Park Ridge, NJ: Noyes Publications (1993).

Kwok, D.Y., A. Leung, C.N.C. Lam, A. Li, R. Wu, and A.W. Neumann, *J. Colloid Interface Sci.* **206,** 44 (1998).

Lee, S.T., S.V. Olesik, and S.M. Fields, *Journal of Microcolumn Separations*, **7**, p. 477-483 (1995).

Lee, W.M., U.S. patent 4,824,763 (1989).

Levich, V.G. *Physicochemical Hydrodynamics*. Englewood Cliffs, New Jersey: Prentice Hall, p. 64 (1962).

Levitin, G., S. Myneni, and D.W. Hess, *Electrochemical and Solid-State Letters*, **6** (8), G101 (2003).

Lin, H., A.A. Busnaina, and I.I. Suni, *Interconnect Technology Conference Proceedings, IEEE*, p. 49-51 (2000).

Louis, D., presented at *Semicon Europa*, Munich, Germany, April (2001).

Lu, C. and A.W. Czanderna, *Applications of Piezoelectric Quartz Crystal Microbalances*. New York: Elsevier, p. 31 (1984).

Mazouchi, A. and G.M. Homsy, *Physics of Fluids*, **13** (10), p. 2751 (2001).

McCaffery, F.G., *Journal of Canadian Petroleum Technology*, **11** (3), p. 26 (1972).

Middleman, S. *An Introduction to Fluid Dynamics*. New York: Wiley (1998).

Middleman, S. *An Introduction to Mass and Heat Transfer*. New York: Wiley (1998).

Mogilnikov, K.P. and M. R. Baklanov, *Electrochemical and Solid-State Letter*s, **5** (12), p. F29-F31 (2002).

Moharam, MG., E.B.Grann, D.A. Pommet, and T.K. Gaylord, *J. Opt. Soc. Am A,* **12**(5) (1995).

Nakao, H. Umimoto, S. Odanaka, T. Ohzone, and H. Esaki, *J. Electochem. Soc.,* **137** (7), p. 2303-2305 (1990).

Namatsu, H., *J. Vac. Sci. Technol. B,* **18** (6), p. 3308-3312 (2000).

Namatsu, H., *J. Vac. Sci. Technol. B*, **19** (6), p.2709-2712 (2001).

Namatsu, H., K. Kurihara, M. Nagase, K. Iwadate, and K. Murase, *Appl. Phys. Lett.*, **66** (20), p. 2655-2657 (1995).

Namatsu, H., K. Yamazaki, and K. Kurihara, *Microelectronic Engineering*, **46**, p. 129-132 (1999).

Oehrlein, G.S. and Y. Kurogi, *Materials Science and Engineering*, **24**, p. 172-180 (1998).

Olim, M., *J. Electrochem. Soc.*, **144** (12), pg. 4331-4335 (1997).

Parker, R., R. Chiarello, and D. Gomez, *Semiconductor Pure Water and Chemicals Conference Proceedings*, Santa Clara, p. 323, March (1998).

Peters, M.S. and K.D. Timmerhaus, *Plant Design and Economics for Chemical Engineers.* New York: McGraw-Hill, Inc., (1991).

Pham, V.Q., G.L. Weible, N. Rao, and C.K. Ober, *Proceedings of SPIE*, **4690**, p. 425-431 (2002).

Poling, B.E., J.M. Prausnitz, and J.P. O'Connell. *The Properties of Gases and Liquids, 5th Ed*. New York: McGraw-Hill, p. 9.78 (2001).

Prausnitz, J.M., R.N. Lichtenthaler, and E.G. de Azevedo. *Molecular Thermodynamics of Fluid-Phase Equilibria, 3rd Ed.* Upper Saddle River, New Jersey: Prentice Hall PTR, p. 653-658 (1999).

Qin, X. and W.V. Chang, *J. Adhesion Sci. Technol*., **10**(10), p. 963-987 (1996).

Rancourt, J.D. *Optical Thin Films – User Handbook*. Bellingham, WA: SPIE Optical Engineering Press, p. 10 (1996).

Semiconductor Industry Association (SIA), *The International Technology Roadmap for Semiconductors*, Interconnect (2001).

Sirard, S.M., P.F. Green, and K.P. Johnston, *J. Phys. Chem. B*, **105**, p. 766-772 (2001).

Stannett, V.T., W.J. Koros, D.R. Paul, H.K. Lonsdale, and R.W. Baker, *Adv. Polym. Sci.,* **32**, p. 71 (1979).

Takahashi, K.M., and M.E. Gross, *J. Electrochem. Soc.,* **146** (12), p. 4499-4503 (1999).

Tompkins, H.G. and W.A. McGahan. Spectroscopic Ellipsometry and Reflectometry. New York: John Wiley & Sons, Inc., p. 59 (1999).

Tracy, D. *SEMI Industry Research and Statistics*, October (2001).

Versteeg, G.F. and W.P.M. Van Swaaij, *Chemical Engineering Science*, **43** (3), p. 573-585 (1998).

West, K.N., *PhD Dissertation*, School of Chemical Engineering, Georgia Institute of Technology (2001).

Woodruff, D.P. and T.A Delchar, *Modern Techniques of Surface Science – Second Edition*. Cambridge: Cambridge University Press, p. 193-198 (1999).

Zubchenko, Y.P., S.F. Shskova, and O.P. Ladygina, *Khimicheskaya Promyshlennost*, **9**, (1985).

VITA

Matthew T. Spuller was born on December 11, 1976, in Southfield, MI to Thomas and Linda Spuller. He attended Manatee High School in Bradenton, FL, graduating in 1995. His interest in chemistry and math motivated his pursuit of a chemical engineering career. He attended the University of Florida, from which he was awarded a Bachelor of Science in Chemical Engineering, with honors, in 1999. Matthew wed Laura Elizabeth LeBlanc on August 14, 1999, and soon after began graduate study at the Georgia Institute of Technology. In the fall of 2003, he was awarded a Doctorate of Philosophy in Chemical Engineering.